

**Study of Dynamic Processes
at the Electrochemical Interface
by *in situ* High Speed STM:**

Surface Diffusion and Adsorbate Interactions

Dissertation

zur Erlangung des Doktorgrades

Doctor Rerum Naturalium

der Mathematisch-Naturwissenschaftlichen Fakultät

der Christian-Albrechts-Universität zu Kiel

vorgelegt von

Andriy Taranovskyy

Kiel, Mai 2012

**Study of Dynamic Processes
at the Electrochemical Interface
by *in situ* High Speed STM:**

Surface Diffusion and Adsorbate Interactions

Dissertation

zur Erlangung des Doktorgrades

Doctor Rerum Naturalium

der Mathematisch-Naturwissenschaftlichen Fakultät

der Christian-Albrechts-Universität zu Kiel

vorgelegt von

Andriy Taranovskyy

Kiel, Mai 2012

Referent: Prof. Dr. Olaf M. Magnussen
Korreferent: Prof. Dr. Eckhard Pehlke
Ort und Tag der Disputation: Kiel, 11. Juli 2012
Zum Druck genehmigt: Kiel, 11. Juli 2012

gez. Prof. Dr. Wolfgang J. Duschl, Dekan

Abstract

The knowledge about surface diffusion and adsorbate-adsorbate interactions is important for deep understanding of various processes on surfaces and interfaces, such as crystal growth, phase transitions, self-assembly or catalysis. Up to now, the direct microscopic measurements of adsorbate-adsorbate interactions were done in a number of selected systems under ultra-high vacuum condition, but no such studies were performed at solid-liquid interfaces. This work is a continuation of the recent *in situ* high-speed STM (scanning tunneling microscopy) study of tracer diffusion of sulphur adsorbates on Cu(100) in aqueous solution of 0.01 M HCl performed by T. Tansel [1]. It revealed a linear dependence of diffusion barriers on the electrode potential, which originates from electrostatic interaction of the adsorbate dipole moment with the electric field in the double layer.

In the present work, development of software for image recognition and further quantitative analysis allowed the extraction of adsorbate-adsorbate interactions and diffusion barriers of adsorbates in the vicinity of neighboring adsorbates from experimental video sequences. For measurements of interactions between adsorbates, two different methods—dynamic and equilibrium analysis—were applied, providing consistent results, obtained for the first time at an electrochemical interface. The measured pairwise interatomic potential for S_{ad} showed anisotropic behavior, with pronounced repulsion at nearest neighbor sites and attraction at next-nearest neighbor sites of the $c(2 \times 2)$ adlattice. The S_{ad} diffusion barriers were considerably decreased in the vicinity of neighboring S_{ad} , as compared to the tracer diffusion barrier of isolated S_{ad} .

In further STM measurements, the model system was modified by introducing species possessing a different (cationic) nature, such as Pb adsorbates. The results of tracer diffusion for Pb_{ad} revealed a similar potential dependence, as in the case of S_{ad} . This behaviour was not expected because of different adsorbate dipole moments of these species, which are opposite in direction. The observed trend was rationalized by the dominant contribution of neighboring Cl_{ad} forming the $c(2 \times 2)$ lattice to the total surface dipole moment during a single jump event. In addition, attractive pair interactions on the order of 20 meV were found between Pb_{ad} at nearest and next-nearest neighbor sites of the $c(2 \times 2)$ lattice.

In the potential regime corresponding to Pb underpotential deposition on Cu(100), a Pb surface alloy phase nucleated at steps and continued by growing along the upper terraces. With our high temporal and spatial resolution STM we could study the fast dynamic processes associated with surface phase transitions during Pb alloying/dealloying. The for-

mation of a novel transient (4×3) alloy phase with 0.25 ML Pb coverage and its continuous transformation into a $c(4 \times 4)$ Pb alloy phase with a coverage of 0.375 ML was observed. By changing the potential sweep in positive direction, Pb dissolution started, resulting in formation of a novel transient $c(4 \times 4)$ Pb alloy phase with lower coverage. Further Pb dissolution lead to the re-adsorption of Cl_{ad} forming $c(2 \times 2)$ domains and development of closed-loop Pb ribbon structures. Based on analysis of high resolution STM images we have suggested a new model for this structure.

Zusammenfassung

Die Kenntniss von Oberflächendiffusion und Adsorbat-Adsorbat-Wechselwirkungen ist wichtig für das tiefe Verständnis der verschiedenen Prozesse an Oberflächen und Grenzflächen, wie z. B. Kristallwachstum, Phasenübergängen, Selbstorganisation oder Katalyse. Bis jetzt wurden direkte mikroskopische Messungen der Adsorbat-Adsorbat-Wechselwirkungen in einer Reihe ausgewählter Systeme unter Ultrahochvakuum-Bedingungen gemacht, aber keine solchen Studien an der Fest-flüssig-Grenzflächen durchgeführt. Diese Arbeit ist eine Fortsetzung des *in situ* Hochgeschwindigkeits-RTM (Rastertunnelmikroskopie) Untersuchung der Tracerdiffusion von Schwefel Adsorbaten auf Cu(100) in wässriger Lösung von 0.01 M HCl, durchgeführt von T. Tansel [1]. Diese deckte die lineare Abhängigkeit der Diffusionsbarrieren vom Elektrodenpotential auf, die durch elektrostatische Wechselwirkung des Adsorbat Dipolmoment mit dem elektrischen Feld in der Doppelschicht entsteht.

In der vorliegenden Arbeit erlaubte die Entwicklung der Software für die Bilderken- nung und die weitere quantitative Analyse die Extraktion der Adsorbat-Adsorbat-Wech- selwirkungen und der Diffusionsbarrieren von Adsorbaten in der Nähe der benachbarten Adsorbaten aus den experimentellen Video-Sequenzen. Für die Messungen der Wechsel- wirkungen zwischen den Adsorbaten wurden zwei verschiedene Methoden—dynamische und Gleichgewichtsuntersuchungen—angewandt, die konsistente Ergebnisse lieferten. Zum er- sten Mal wurden solche Daten an elektrochemischen Grenzflächen erhalten. Das gemessene paarweise interatomare Potenzial für S_{ad} zeigte anisotropes Verhalten, mit ausgeprägter Re- pulsion bei nächsten Nachbarn Plätzen und Attraktion bei übernächsten Nachbarn Plätzen des $c(2 \times 2)$ Adsorbatgitter. Die S_{ad} Diffusionsbarrieren waren, im Vergleich zu der Diffu- sionsbarriere von isoliertem S_{ad} , in der Nähe von benachbarten S_{ad} deutlich kleiner.

Das Modellsystem wurde in weiteren RTM-Messungen durch hinzufügen von Ionen (Ka- tionen) mit unterschiedlichen Eigenschaften, z.B. Pb Adsorbate, modifiziert. Die Ergeb- nisse der Tracerdiffusion für Pb_{ad} offenbart eine ähnliche Potentialabhängigkeit, wie im Fall von S_{ad} . Dieses Verhalten wurde nicht erwartet, aufgrund der unterschiedlichen Adsorbat Dipolmomente dieser Spezies, die in entgegengesetzter Richtung sind. Der beobachtete Trend konnte durch den dominanten Beitrag des benachbarten Cl_{ad} in der $c(2 \times 2)$ Über- struktur zu dem Gesamtbeitrag des Dipolmoments während eines einzelnen Sprungs erklärt werden. Darüber hinaus wurden attraktive Paar-Wechselwirkungen in der Größenordnung von 20 meV zwischen Pb_{ad} an nächsten und übernächsten Nachbarnplätzen des $c(2 \times 2)$ Gitters gefunden.

Im Potentialregime der Pb Unterpotentialabscheidung auf Cu (100) nukleiert eine Pb-Oberflächenlegierung an den Stufen und breitet sich aus durch Wachstum entlang der oberen Terrassen. Mit der hohen zeitlichen und räumlichen Auflösung unseres RTM konnten wir schnelle dynamische Prozesse studieren, die mit dem Oberflächen-Phasenübergänge während Pb Legierung/Legierungsauflösung verbunden sind. Die Bildung einer neuen transienten (4×3) Legierungsphase mit 0.25 ML Pb Bedeckung und ihre kontinuierliche Transformation in eine $c(4 \times 4)$ Legierungsphase mit Bedeckung von 0.375 ML wurde beobachtet. Durch Ändern des Potentials in positiver Richtung wurde die Pb Auflösung initiiert, was die Bildung eines neuen transienten $c(4 \times 4)$ Legierungsphase mit niedrigerer Bedeckung zur Folge hat. Die weitere Pb Auflösung führt zu der Re-Adsorption von Cl_{ad} , das $c(2 \times 2)$ Domänen bildet, und der Entwicklung von geschlossenen Pb Bandstrukturen. Basierend auf der Analyse der hochauflösenden RTM-Bilder haben wir ein neues Modell für diese Strukturen vorgeschlagen.

Contents

1. Adsorbates at electrochemical interfaces	1
1.1. Metal-solution interface	1
1.2. Adsorbate-adsorbate interactions	5
1.3. Measurements of adsorbate-adsorbate interactions in UHV	8
1.4. Electrochemical Video STM	13
2. Image Recognition Software	17
2.1. Adsorbate detection	19
2.2. Surface lattice recognition	21
2.3. Lateral drift correction	25
2.4. Adsorbate assignment	26
3. Quantitative measurements of adsorbate-adsorbate interactions	29
3.1. Dynamic analysis	29
3.2. Equilibrium analysis	38
4. Results of the quantitative study of the S_{ad}-S_{ad} interactions	47
4.1. Synopsis	47
4.2. Publication Physical Review Letters 104 , 106101(2010)	49
4.3. Publication ChemPhysChem 11 , 1438(2010)	54
4.4. MC simulation of high coverage structures	63
4.5. Adsorbate mobility and residence times	65
5. <i>In situ</i> STM study of Pb on Cu(100) in Cl containing solution	69
5.1. Pb surface diffusion and interactions	69
5.2. Publication The Journal of Physical Chemistry C 115 , 19336(2011).	72
5.3. Underpotential deposition of metals	80
5.4. Pb surface alloying and dealloying	81
5.5. Publication submitted to Physical Chemistry Chemical Physics	82

6. Summary	117
A. List of the developed software	119
B. List of original data used in the quantitative analysis	121
C. Bibliography	123

1. Adsorbates at electrochemical interfaces

1.1. Metal-solution interface

The major part of electrochemical science is related to the study of interfaces between an electronic conductor (metal or semiconductor) and an ionic conductor (electrolyte) [2]. In order to have a look on the processes at such interfaces, let's briefly consider a metal electrode immersed in an electrolyte solution (Fig. 1.1). For specific studies, a monocrystal metal electrode is usually used, so that the complete surface, which is in a contact to the electrolyte, corresponds to a single crystal plane. The electrolyte typically consists of an aqueous solution of negatively and positively charged ions. The water molecules carry a dipole moment, that is why in Fig. 1.1 they are represented with arrows. As a result of the solvation process, the anions and cations are surrounded by the solvent molecules which form solvation shells by rearrangement of their dipoles due to the interactions with ions.

In the general case, the electrochemical interface is charged. Once the metal electrode gets into contact with the electrolyte, redistribution of charges occurs in the interface region. Two types of electrochemical reactions can take place: ion transfer reactions and electron-transfer reactions. In the first case an ion migrates to the interface and afterwards discharges. For the second kind of reactions, the ions or uncharged species can be reduced by electrons which can tunnel from the metal surface through the electrolyte over a distance up to 10 Å. These reactions lead to an inhomogeneous charge redistribution under equilibrium condition, thus, the metal surface carries an excess charge which is balanced by a charge of equal magnitude and opposite sign located in the adjacent layer of electrolyte. Due to both higher concentrations and mobilities of charge carriers in metals than in electrolytes, their conductivities are several orders of magnitude higher than for electrolytes. Therefore, an excess charge on the metal surface is located in a narrow surface region with a thickness of about 1 Å. Since concentrations of ions in the solution are smaller than for free electrons in the metal, the balanced charge is distributed in the solution in a wider region of 5–20 Å thick [3]. These two narrow regions at the interface are forming the electric double layer. Its structure is similar to a plane capacitor, with the difference that its part in the electrolyte has a diffuse shape. Since usually the separation between the effective

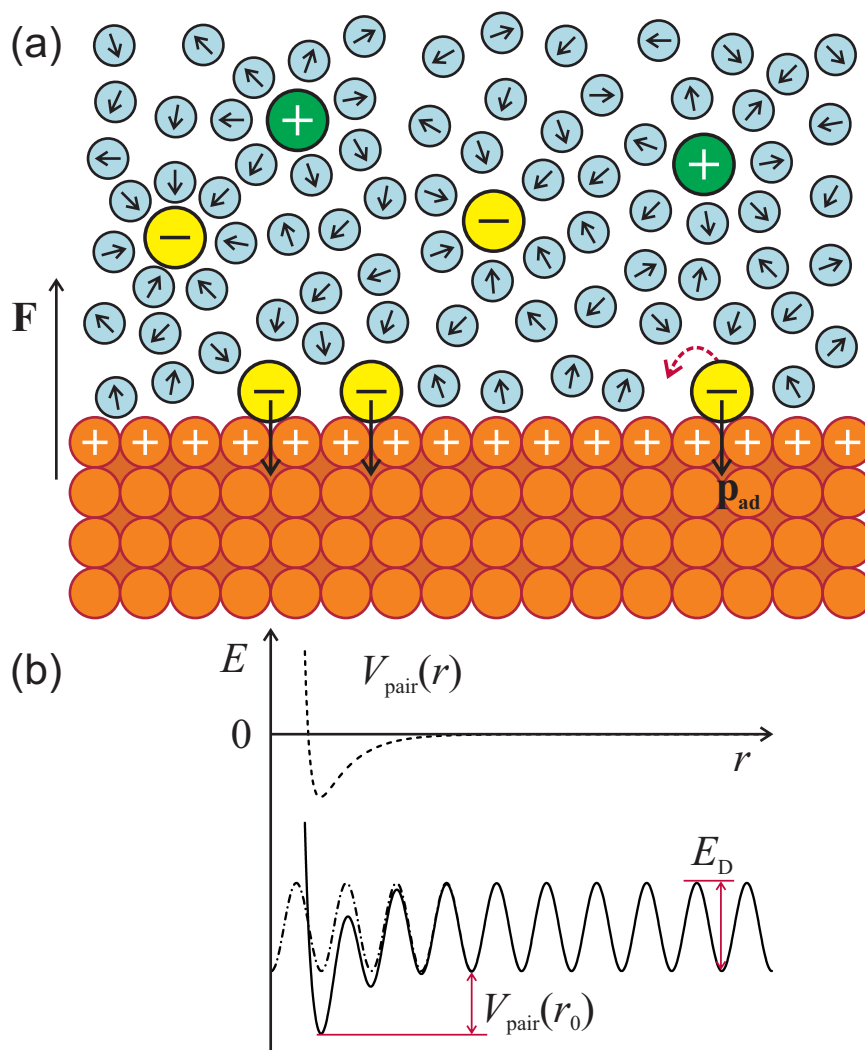


Figure 1.1.: a) Schematic representation of metal-electrolyte interface. b) Modification of the surface energy landscape by mutual interactions between adsorbates.

plates d is in the order of 10 \AA , the capacity of the double layer per unit area $C = \epsilon\epsilon_0/d$ can be extremely high. Consequently, for typical electrode potentials in the order of 1 V , the electric field \mathbf{F} in the double layer region can reach very high values up to 10^9 V/m . Such a high field will have a considerable influence on the charged species at interface. Thus, in comparison to vacuum conditions, the electrode potential ϕ become a second (in addition to the temperature T) parameter, which determines dynamics of processes at electrochemical interfaces [4,5]. In the specific case, when the interface carries no charge, the corresponding electrode potential is the potential of zero charge ϕ_{pzc} . Such condition is the most relevant for comparison of the surface energetics with those in the vacuum.

For solvated ions in the vicinity of the metal surface there is a chance that their solvation shells will be broken and they come in direct contact with the metal. In such case, if the interactions between an ion and metal atoms is stronger than with solvent molecules it will specifically adsorb on the metal surface. If adsorption takes a place due to the physical interactions (such as van der Waals forces [6]) it is called physisorption. If adsorption is complicated in addition by chemical interaction between adsorbates and electrode, one speaks about chemisorption. Chemical interactions are considerably greater than physical ones, and in contrast to physisorption, usually chemisorption is irreversible under vacuum conditions. In electrochemical environment the desorption of chemisorbed species can be achieved by applying a proper electrode potential.

Upon adsorption of an ion with charge $z_{ion}e_0$ on the metal surface, redistribution of electronic density between an adsorbate and the metal surface happens, which depends on the relative position of the metal Fermi level and the adsorbate density of states. Due to the unequal charge distribution between the adsorbate and the metal, a surface dipole moment of the adsorbate \mathbf{p}_{ad} is formed [7]. If the adsorbate dipole moment has a direction inwards to the metal it is denoted as negative (typical for halide ions); if the direction is outwards, then it is positive (metal adsorbates).

The presence of adsorbates at the metal with a surface density n_{ad} will change the total potential drop across the interface by an amount

$$\Delta\phi = n_{ad} \frac{p_{ad}}{\epsilon_0} \quad (1.1)$$

In addition, one has to keep in mind, that in electrochemical environment as compared to the vacuum condition, the effective surface dipole moment includes also contributions of neighbouring solvent molecules. Because of interaction with adsorbates, solvent molecules

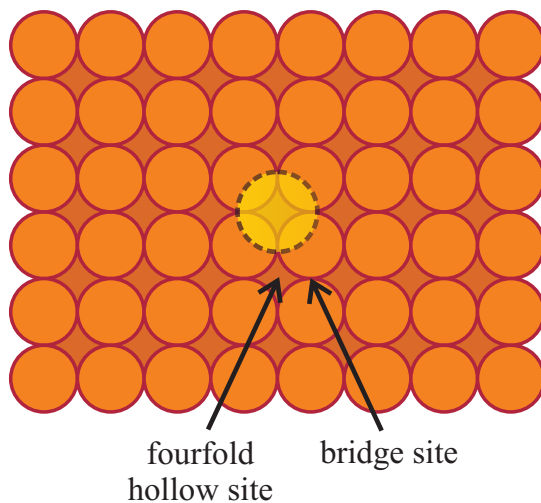


Figure 1.2.: Fourfold hollow site and twofold bridge site on a single fcc(100) crystal surface

will orient their dipoles in the opposite direction, thus, reducing the total potential drop across the interface. In practice, it is not possible to differentiate contributions from adsorbates and surrounding solvent molecules.

The adsorption takes place on specific sites, which correspond to the energetically favorable positions, i.e. local minima of the total energy of the system which includes the adsorbates and the metal surface. For ex., during the halide ion adsorption on fcc(100) crystal surface such locations are usually situated in the fourfold hollow sites (Fig. 1.2). In the case of surface diffusion, when an adsorbate located at one fourfold site moves to the closest fourfold site it passes across a bridge site or twofold hollow site, characterized by higher energy.

The schematic representation of the the periodic energy landscape of the surface shown in Fig. 1.1a is given in Fig. 1.1b. To perform a jump between neighbouring adsorption sites, the isolated adsorbates need to overcome an energy barrier E_D , which is the difference of adsorption energies in activated state and adsorption site. If the adsorbate have another coadsorbate in the close neighbourhood, the energy landscape can be influenced by mutual interactions between them (left part of Fig. 1.1a). This modification is denoted as the adsorbate-adsorbate pairwise potential V_{pair} . Both activation energy barrier E_D and pairwise potential V_{pair} determine the dynamic processes on the interface such as surface diffusion and phase formations.

As was mentioned before, the important difference between electrochemical interface and vacuum condition is the presence of the strong electric field in the double layer. Thus the

Gibbs free energy of adsorption includes additional term corresponding to the interactions of adsorbate dipole moments with this field [1, 4, 5]:

$$G_{ad} = G_{ad}^0 - \mathbf{p}_{ad}\mathbf{F} = G_{ad}^0 + p_{ad}F. \quad (1.2)$$

Here G_{ad}^0 is the free adsorption energy at the uncharged interface, i.e. at the potential of zero charge. For a homogeneous distribution of adsorbates on the surface and low defect densities, such as terrace steps, the electric field is uniform and equals $F = \sigma(\phi)/\epsilon_0$, where $\sigma(\phi)$ is the potential dependent surface charge density. Substituting this in eq.(1.2) gives

$$G_{ad} = G_{ad}^0 + p_{ad}\sigma(\phi)/\epsilon_0. \quad (1.3)$$

Therefore, the activation diffusion barrier for the adsorbate is

$$E_D = E_D^0 + \Delta p_{ad}\sigma(\phi)/\epsilon_0, \quad (1.4)$$

where E_D^0 is a diffusion barrier at the potential of zero charge, Δp_{ad} is the difference of adsorbate dipole moments in activated state and adsorption site. For the potential range, in which the interface capacitance C can be considered as a constant quantity, the surface charge is

$$\sigma(\phi) = C_{pzc}(\phi - \phi_{pzc}), \quad (1.5)$$

where C_{pzc} is the interface capacitance at the potential of zero charge. Substituting this into eq.(1.4) gives linear dependence of diffusion barrier on electrode potential, which was already found in the direct STM studies of S_{ad} tracer diffusion on Cu(100) surface [1] and Ostwald ripening of islands on Au(100) electrodes [4].

1.2. Adsorbate-adsorbate interactions

The adsorbate-adsorbate interactions in general, combine contributions from variety of interactions of different nature. The interactions between adsorbates on the metal surface can be attributed to two kinds—direct, when the adsorbates interact directly through the

medium between them and indirect, which are caused by a mutual perturbation of the substrate surface [8].

The following interactions are referred as direct:

Pauli repulsion or 'exclusion principle' repulsion. It results from increase of the interaction energy by the overlap of antisymmetric wavefunctions of electrons. According to the exclusion principle, the electrons with parallel spins has to be in different space states, thus it keeps them separated away from each other [9]. This interaction energy reaches high values at short distances between adsorbates and therefore is responsible for the site blocking effect, i.e. limits the minimal distance at which adsorbates can approach each other. It decreases fast with the interatomic distance, typically it is approximated by $\propto 1/r^{12}$ distance dependence [10].

Van der Waals forces. Usually they are less strong in comparison to other kind of interactions and play a dominant role only in physisorption, typically for adsorption of rare gases. For such adsorbates the dipole moment is mainly induced by deformation of electronic charge distribution, as compared to higher dipole moment of chemisorped adsorbates where the charge transfer from the adsorbate to the substrate takes place. The van der Waals forces are attractive, the dispersive contribution to the adsorbate interactions is evaluated as $\propto -C/r^6$, where C is a constant proportional to the square of the polarisability [11].

Electrostatic dipole-dipole interactions. For two adsorbates on the metal surface which have dipole moments p_A and p_B the interaction energy is given by [12]

$$E(r) = \frac{1}{4\pi\epsilon_0} \cdot \frac{2p_A p_B}{r^3}. \quad (1.6)$$

This is two times higher than the interaction of the equivalent dipole moments in the same configuration in the vacuum. The reason for such difference is the ideal metal screening: the real charge is distributed over the surface nevertheless it acts as located at the image point. For adsorbates of the same species electrostatic configurations are always repulsive.

For adsorbates on metal surfaces, the indirect interactions play a significant role. One distinguishes the following interactions which belong to this type:

Substrate-mediated electronic interactions. Upon chemisorption, a discrete adsorbate electron level broadens into a band which can be described by a density of states function filled up to the Fermi level. Adsorbate wave functions combine with metal substrate wave functions and may overlap, or in other words adsorbates share the same electrons via the

metal substrate, thus interact each other. If the overlap of wave functions happens in phase, then the interaction is attractive, if it is out of phase then it is repulsive. Since the wave functions are oscillatory itself, the interactions should have also an oscillatory dependence on the distance between adsorbates. The theoretical groundwork based on the tight binding model [13–15] concludes that the asymptotic part of interactions has a long range shape with the amplitude decreasing as inverse square root of distance (in contrast to the bulk where it decreases as inverse fifth power of interatomic distance [15]) and a period equal to the half of Fermi length.

Electrons filling the surface band on close-packed surfaces of noble metals form a 2D nearly free electron gas. Scattered off point defects and step edges due to the quantum interference it produces the standing wave spatial oscillating patterns in the local density of states, which can be imaged by STM by applying a low bias at low temperatures. A good illustration of the electronic substrate mediated interactions is given in the study of surface mediated interactions of Cu adatoms on Cu(111) surface at low temperature regime ($T = 9 - 21$ K) by Repp [16]. The obtained STM images represented the electronic standing wave pattern perpendicular to the surface caused by scattering of electrons off two Cu adatoms located at different separations. The interactions between adatoms were directly related to the changes in local density of states (LDOS) at Fermi level around the pair of adatoms. The case when the LDOS is decreased was corresponding to the minimum of potential energy between the two adatoms, and if it is was increased—to the maximum of the potential energy. The theoretical description made by Hyldgaard and Persson [17] based on double scattering of the two-dimensional electron gas from adatoms at Fermi level reveals the energy of adsorbate interactions in the asymptotic approach for large distances r

$$E(r) = -\varepsilon_F \left(\frac{2 \sin(\delta_F)}{\pi} \right)^2 \frac{\sin(2q_F r + 2\delta_F)}{(q_F r)^2}, \quad (1.7)$$

where ε_F is the Fermi energy measured from the bottom of the surface band, δ_F is the Fermi-level phase shift of adsorbate induced standing wave pattern ($\delta_F = -\pi/2$), and q_F is the in-surface Fermi wave vector. At short interadsorbate distances discrepancies between measured adsorbate interaction energies [16, 18] and the values obtained by formula(1.7) were found. These differences could be rationalized by the influence of the bulk electronic states on the scattering of the surface electrons.

Interactions mediated by the elastic distortion of the lattice. The classical interpretation of the adsorbate pair interactions on the elastically isotropic surface by Lau and Kohn [19]

in the approximation of large separations gives $\propto 1/r^3$ interadsorbate distance dependence and is inversely proportional to the shear modulus of the substrate. The interaction is repulsive for identical atoms and also for physisorbed atoms, for arbitrary atoms it can be repulsive or attractive. Qualitatively, the adsorbates will have attractive interaction, if the lattice distortion caused by adsorbate A on the substrate atoms in the vicinity of adsorbate B will coincide with lattice distortion caused on these substrate atoms by adsorbate B, and vice versa. The distance dependence is the same as for dipole-dipole interactions, however, estimations give a somewhat smaller strength of interactions.

In 2000 Pedersen [20] et al. in an STM study of the diffusion of N atoms adsorbed on Fe(100) surface found that the diffusion of N atoms in the close vicinity of another N adsorbate is anisotropic, i.e. the diffusion barrier depends on the direction of the jump as well as the initial relative configuration of the adsorbates. Ab initio DFT calculations reveal the strong coupling of N atoms to the Fe substrate, causing strong local lattice strain. When the lattice distortions caused by two adsorbates have the same direction, the interaction is attractive, if they counteract—it is repulsive.

For any pair of adsorbates, the total interaction energy which includes contributions from the described above kind of interactions can be measured experimentally. From certain characteristics such as magnitude and distance dependence of the interatomic potential, anisotropy of interactions, nature of species or local intermediate environment, one may estimate, which interactions made major contributions to adsorbate-adsorbate interactions under given conditions. However, it is not possible to determine the contributions of each kind of interactions separately.

1.3. Measurements of adsorbate-adsorbate interactions in UHV

Indirect measurements of adsorbate-adsorbate interactions have been done in studies of adsorbate surface phase transitions by macroscopic techniques such as low-energy electron diffraction (LEED). The interaction energies were derived by fitting of the lattice gas model to the experimentally obtained decay of the superlattice beam intensity as a function of temperature during phase transitions at low and saturation coverages of O on W(110), related to the island dissolution and order-disorder transformations respectively [21–23].

In similar studies the adsorbate interactions in the lattice gas model were adjusted to reproduce the phase diagram of chemisorbed layers of O/W(110) [24], H/W(100) [25], O/Ni(111) [26,27]. The effect of lateral interactions on the heat of adsorption as a function of coverage and its influence on desorption and migration kinetics was investigated by King

et al. [28]. By the simplistic view, the repulsive interactions between nearest-neighbors decrease the diffusion barrier height and attractive interactions increase it. In turn, the formation of ordered surface structures causes a coverage dependence of available empty adsorption sites and thus affect the adsorption kinetics [29, 30].

The development of modern high resolution microscopic techniques (FIM, STM), which allows the imaging and detection of individual adsorbates located on particular adsorption sites of crystal surfaces, has opened new possibilities to perform direct quantitative measurements of adsorbate surface diffusion and adsorbate-adsorbate interactions.

In the majority of works, it was accomplished by measuring the equilibrium adsorbate spatial distributions and following extraction of interaction energies between the adsorbates on the metal surfaces under UHV condition. The existing data of measured values of interactions between adsorbates on single metal surfaces in UHV obtained in various scientific groups are cited in Table 1.1¹. The first analysis was done in 1973 by Tsong for 5 rhenium atoms on the tungsten (110) plane [31]. Between the imaging, heating periods at 320 K with a duration of 3 min were applied so that adsorbates reach the new equilibrium location and for each image the pair correlation were obtained. It was found that the interaction potential exhibits an oscillatory behavior with at least two relative minima at 2.74 Å and 6.8 Å. However, the direct determination of adsorption sites was not performed and the atomic distributions were build in relation to the distances between adsorbates, which were not completely correct measured, since a strong nonlinear distortion is typical for the FIM images.

One year later, Graham studied tungsten self-adsorbed atoms diffusing on the (211) and (321) planes and separated from each other by an empty channel [33]. The analysis revealed that, for this separations ($r > 7$ Å) no interaction between adsorbates was found and their behavior doesn't differ from independently diffusing particles. At the same time, tungsten adatoms located in adjacent rows at $r = 4.48$ Å showed a strong interaction which was evident from the highly correlated motion of adatoms. Such interaction had a profound effect on adsorbate arrangements so that the determination of the pair distribution function was not possible. In 1980, Fink et al. observed long range anisotropic interactions between palladium and wolfram (or rhenium in an alternative experiment) on the W(110) surface [34]. At a temperature of 240 K, W remains immobile and can serve as reference point on the surface, while Pd or Re still diffuse along the surface. For W–Pd pair distributions, two

¹Here we present only the selected values of interatomic potential at given separations which correspond to the most pronounced attraction minima or repulsion maxima.

Table 1.1.: Measured values of adsorbate-adsorbate interactions in UHV

Author, year	Adsorbate pair	Substrate	r , Å	$V_{pair}(r)$, meV ¹
Tsong, 1973 [31]	Re–Re	W(110)	2.7	≈-160
			6.8	≈-40
Tsong, 1981 [32]	W–Re	W(110)	2.7	-99.0
	W–Ir		2.7	-53.2
	Ir–Ir		5.5	-82.0
Graham, 1974 [33]	W–W	W(211)	>7	≈0
		W(321)	>7	≈0
Fink, 1984 [35]	Re–Re	W(110)	<10	≈-50
Watanabe, 1989 [36]	Re–Pd	W(110)	2.7	-36.8
			3.2	≥45
			4.5	≥45
			6.9	≥45
Watanabe, 1991 [37]	W–Pd	W(110)	2.7	-50.4
			3.2	≥40
			4.5	≥40
			5.3	41.1
Watanabe, 1992 [39]	Ir–Ir	W(110)	2.7	-86.0
			3.2	70.0
			4.5	70.0
	Re–Re	W(110)	2.7	21.5
			5.3	64.4
11.0	-31.5			
Koh, 1999 [40]	Pd–Pd	W(110)	2.7	-88.6
			3.2	14.0
			4.5	28.5
			5.3	42.0
Trost, 1996 [41]	N–N	Ru(0001)	2.7	>200
			4.7	13
			5.4	-18
Renish, 1999 [42]	O–O	Ru(0001)	4.7	33
			5.4	-43

Table 1.1.: Measured values of adsorbate-adsorbate interactions in UHV

Author, year	Adsorbate pair	Substrate	r , Å	$V_{pair}(r)$, meV ¹
Repp, 2000 [16]	Cu–Cu	Cu(111)	7.0	5.3
			12.5	-0.4
			27	-0.4
Ebert, 1996 [44]	Vac–Vac	InP(110)	9.0	65
Österlund, 1999 [45]	N–N	Fe(100)	2.9	140
			4.1	23
Knorr, 2002 [18]	Cu–Cu	Cu(111)	12.5	-2.0
			27	-0.5
	Co–Co	Cu(111)	12.5	-1.5
			27	-0.5
	Co–Co	Ag(111)	17	2
			28	-0.5

preferred adsorption locations at 3.2 Å and 11.0 Å were observed, for W–Re, the pronounced attraction was found at 5 Å distance and to a less extent at 8 Å.

An important step in adsorbate interaction studies was made by Fink in 1984 by the first direct mapping of the Re adsorbates to the adsorption sites on the W (110) plane [35]. The lattice was reconstructed from the 345 recorded positions of single Re diffusing along the surface at 380 K. Once the lattice grid was established it provided a convenient tool for the distance measurement between the adsorbates. The analysis of pair correlations for two Re adatoms showed repulsive interactions for distances less than 10 Å. Despite this fact, the formation of stable Re trimers (linear as well as triangular) was observed, indicating that many-body effects for metal adatoms can play an important role.

The developed method of direct adatom mapping was improved by Watanabe in 1989 [36–38]. The significantly increased number of statistical observations (more than 1500) allowed the presentation of obtained pair correlations in a new quality—in the form of a two-dimensional distribution function, thus the dependence of interaction energies on interatomic distance as well as orientation could be extracted. The study of Re–Pd, W–Pd, and Ir–Ir adatom pairs distribution on W(110) revealed that, for all three cases, the interactions are highly anisotropic, as could be expected for the indirect elastic interactions, with repulsion along $[1\bar{1}0]$ and $[001]$ and long range attraction along $[1\bar{1}1]$ directions. The absolute interaction energy values were on the order of a few 10 meV.

Recently, with the application of STM, the measurements of pair interaction energies were performed in a variety of systems. Atomic nitrogen chemisorbed on Ru(0001) was investigated by Trost with STM at 300 K [41]. From the statistical analysis of a N distribution with a surface coverage on the order of 0.1 ML the effective pair interaction potential was extracted. This potential consist of the real pairwise potential and the entropic forces which become significant with an increasing coverage. It was shown that the observed oscillating shape of N distribution function can be rationalized by a pair interaction potential characterized by a strong repulsion on the nearest, and to a much lower extent, at the next-nearest hcp threefold sites, and weak attraction at the third-neighbor sites.

An STM study was done also for interactions between vacancies on InP(110) surface, which show a screened Coulomb potential form with a vacancy charge of $+1e$, except at short distances [44].

Repp et al. performed a study of the interactions between the two copper adatoms on Cu(111) mediated by the two-dimensional electron gas in the low temperature regime of 9–21 K [16]. The obtained potential exhibits long range oscillating behavior with a period of half the Fermi wavelength. Up to distances of 70 Å, 5 potential minima were determined. On the recorded STM images of adatoms with different separations it was clearly seen that the local density of states decreases if there is a potential energy minimum between the adatoms.

In the work of Osterlund, the configurational analysis was performed for N adsorbate distributions with a surface coverage of 0.1 ML on Fe(100) [45]. In addition to pair interactions, three-body interaction energies were taken into account, providing the best fit of the corresponding MC simulations to the experimental data.

A new concept of quantitative measurements of pair interactions was introduced by Renish after development of an STM with high temporal resolution [42, 43]. The image acquisition rate of 8 to 20 frames per second allows to trace directly the individual pairs of adsorbates and to extract the interaction energies from their relative motion via a master equation model. The study of O adsorbates on Ru(0001) showed that hopping rates of O adsorbate can be modified up to one order of magnitude in the presence of another O adsorbate. As expected for chemisorbed nonmetallic adsorbates, the shape of the obtained O interatomic potential had repulsive and attractive branches.

At the end of this short overview it is worth to mention, that similar methods were applied as well by Hoster and Bergbeiter in their STM studies of metal surface alloys [46, 47]. The effective pair interaction parameters in the two-dimentional $\text{Cu}_x\text{Pd}_{1-x}$ monolayer surface

alloys on Ru(0001) were determined from a statistical analysis of atomic distributions for different alloy compositions.

1.4. Electrochemical Video STM

After invention of STM in 1981 by G. Binnig and H. Rohrer [48,49] it became a widely used experimental tool for studying various structures and processes at surfaces and interfaces at scale in the range from few micrometers down to the subnanometer regime [50,51]. In addition to the imaging, it allows precise manipulation of the atoms and molecules on the surfaces [52]. The advantage of STM as compared to other surface imaging technique such as field ion microscopy (FIM) is that the sample is represented by a flat single-crystal surface instead of a sharp single-crystal tip. Thus larger areas can be imaged with very high resolution. Also using a plane substrate helps to avoid high stress fields which emerge during preparation of high curvature tips. In addition, in contrast to FIM, it allows surface imaging at solid-liquid interfaces as well.

The measuring principle of STM is based on quantum mechanical effect which can be observed when two conducting materials are separated by a very thin insulator (in order of few angstroms). Despite the existence of a potential barrier for electrons whose energy is lower than the height of this barrier, there is a finite probability for them to penetrate ('tunnel') through it similar as a wave and the tunneling current can be detected [53,54]. Let's consider two similar metals (sample and tip) in the vacuum separated only by empty narrow space with a thickness d when the bias voltage U is applied. In both metals the energy levels of electrons are filled up to Fermi levels ε_F which are shifted from one another by the amount eU (Fig. 1.3). To bring an electron to the vacuum level E_{vac} one needs an extra energy Φ , the so-called work function of the metal. In general, the one-dimensional energy barrier between metals is represented by an arbitrary shape function $\Phi(z)$ of coordinate z in the direction normal to the metal surfaces. It can be characterized by the mean potential barrier height $\bar{\Phi}$ above the Fermi level of the negatively biased sample electrode. A tunneling of electrons through the barrier passes from the sample to the tip and in opposite direction from tip to sample resulting in the net tunneling current I .

If a low bias voltage is applied, i.e. $eU \ll \bar{\Phi}$, the tunneling current can be expressed by [55]:

$$I = const \cdot eU \cdot e^{-2\frac{\sqrt{2m\bar{\Phi}}}{h}d}, \quad (1.8)$$

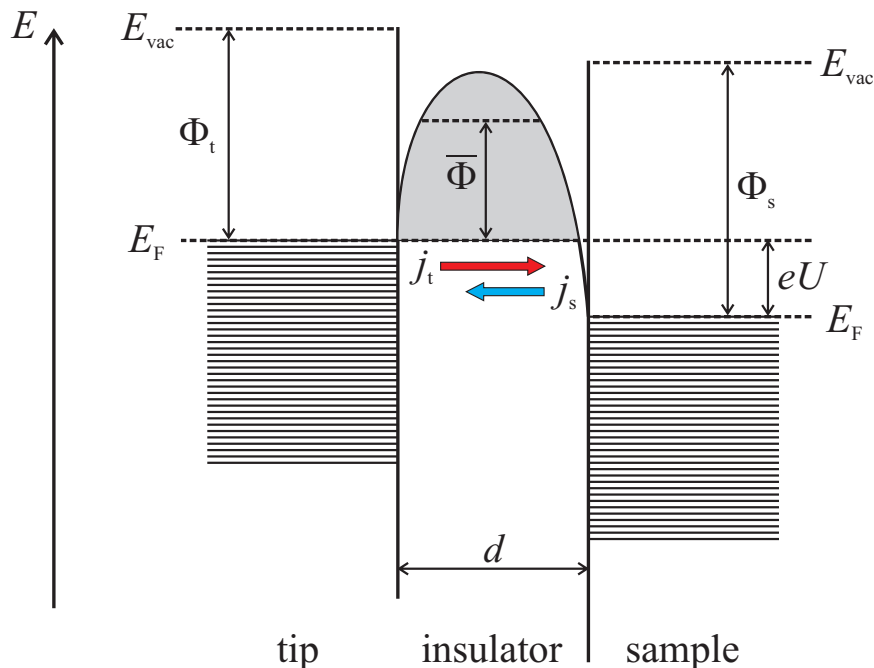


Figure 1.3.: Potential barrier in a thin insulating film between two metal electrodes.

where e and m are charge and mass of the electron and h is the Plank constant. The tunneling current I is proportional to the voltage U so it obeys Ohm's law at low bias. It depends exponentially on the square root of the mean potential barrier height and the distance between tip and electrode. The last property means high sensitivity of current I to the changes in this separation and can be used for topographic imaging of the surface. With this aim the tip is connected to a piezo element which can change its dimensions by applied voltage and allows moving of the tip in the orthogonal directions x and y parallel to the surface as well as in direction z perpendicular to the surface.

The experimental part of this study was performed by measurements in electrochemical environment with *in situ* high speed scanning Scanning Tunneling Microscope (STM). The detailed description of the STM developed in the group of Behm, and operating PC software for video data processing have been given already [56–59].

This STM allows operation in two regimes: constant current imaging (CCI) and constant height imaging (CHI) as schematically shown in Fig. 1.4. In the first mode, while scanning over the surface, the tunnel current between tip and surface is kept at the constant determined value. This is provided by the feedback loop, which compares the measured tunneling current with the reference current and generates the voltage U_z which is applied

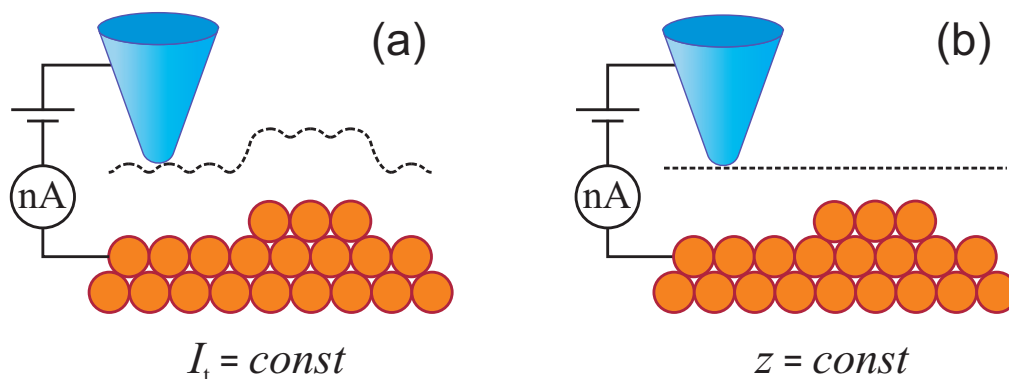


Figure 1.4.: STM topographical imaging in a) constant current mode, b) constant height mode

to the z -piezoelectric drive and adjusts the position of the tip over the surface to make both currents equal. This voltage U_z is plotted then as a function of lateral coordinates x and y and reflects the topographic features of the surface structure. The scan speed in this mode is crucially determined by the response time of the feedback loop.

The scanning speed can be increased considerably if the response frequency of the feedback loop is greatly reduced. In this case, the tip is held at constant height while scanning over the surface (CHI). The measured tunnel current as a function of x and y coordinates of the tip includes the topographic information via eq.(1.8). This mode allows real-time recording with image acquisition rates up to 30 Hz, allowing study of dynamic processes such as the movements of adsorbates on the surface. For this purpose, scanning speed should be faster than the adsorbate hopping rates. At the same time, the scanning frequency is limited by the lowest mechanical resonance frequency of the tip. For successful scanning in this mode, it is important to avoid the collision of the end of tip with the rough areas on the surface ('tip crash'), since the feedback loop is not controlling tip-surface separation in this case. That is why the measurement in CHI mode is applicable only to very flat surfaces.

In our experiments CCI mode was used prior to the main measurements in CHI mode. Due to the slow scanning speed it allows to imagine relatively big areas (up to $4000 \times 4000 \text{ \AA}^2$), also with a rough surface topology, and helps to allocate flat terraces. Those were scanned afterwards in the fast mode by reducing the size of scanning area to less than $400 \times 400 \text{ \AA}^2$.

The STM measurements were performed at room temperature in an electrochemical (EC) cell designed as a cylindrical shape Kel-F reservoir filled by aqueous electrolyte of about 1 mL volume. A three-electrode configuration consisting of the working electrode

(studied Cu(100) monocrystal surface), a reference electrode and a counter electrode was implemented in the EC cell. The potential of the sample was measured versus the reference electrode. To ensure the reliability of these measurements, the ohmic drop between the working and the reference electrodes should be minimized. This can be achieved by the counter electrode which provides the electric current to the sample so that only a negligibly small current flows through the reference electrode. With this aim, the counter electrode was designed as a circular shape platinum wire mounted around the inner walls of the EC cell. In turn, the reference electrode was adjusted at a possible minimal distance to the working electrode, in order to reduce the thickness of the electrolyte layer between both electrodes and, consequently, its ohmic resistance. In various experiments, either copper or platinum wire have been used as a so-called pseudo reference electrode, calibrated vs. a saturated calomel reference electrode (SCE).

Prior to each measurements the Cu(100) crystal was electropolished in 70% solution of orthophosphoric acid and afterwards immersed into studied electrolyte solution, avoiding contact of the crystal surface with an air [60].

STM tips were prepared from 0.3 mm thick tungsten wire by electrochemical etching in 2 mM KOH electrolyte [61]. For stable measurements in electrochemical environment, the potential between tip and sample U has to be set up in the double layer regime, otherwise, charge transfer reactions will occur, causing morphological changes of the tip. Here two main problems arise. First, faradaic currents in electrolyte will superimpose on the measured tunnel current causing its offset. Second, the double layer capacity of the tip will produce additional noise in the current signal. In order to reduce these effects, one needs to limit the area of the tip exposed to the electrolyte. This can be achieved by polymer coating of the major part of the tip surface, leaving only the end of the tip exposed to the electrolyte [62–64].

In any measurement, it is important to minimize the influence of the experimental tool on the studied object. For high quality surface imaging with STM, one needs to keep the tip at close distance to the surface, however, then the interaction between tip and adsorbates on the surface has to be taken into account. Depending on the strength of this interaction, it may influence the hopping rates of adsorbates or even 'push away' adsorbates from the scanning area. That is why, in study of surface diffusion, it is necessary to check carefully the tip effect at different tip-surface separations, i.e. tunnel currents, and to find the optimal condition range, under which the tip influence on adsorbate dynamics is rather small [61].

2. Image Recognition Software

The STM video sequences, recorded with image acquisition rate of 10–20 fps, typically contain from a few hundreds up to two thousands frames. Prior to the application of quantitative methods for adsorbate tracer diffusion and adsorbate-adsorbate interactions studies, one needs to transform these sequences of images into sequences of corresponding digital occupation maps for the following analysis. This output should contain information about the occupation of surface lattice sites by the studied adsorbates for every individual image. This part of the thesis describes how in the present work an automatic procedure was developed for the process of image recognition.

The generalized scheme of the image recognition algorithm is presented in Fig. 2.1. Before the frame by frame processing starts, recognition of the surface lattice has to be performed initially (the left branch of the flowchart). It includes determination of the lattice vectors and (if it is possible) correction of the nonlinear distortion of STM image. In the case when the chloride adlattice is hardly visible, it can be reconstructed from the positions of sulphur adsorbates, which occupy the same lattice sites as the chloride adsorbates (this can be checked as shown later). If during the separate STM measurement the size of the scanning area and the scanning direction along the surface were not changed, the lattice recognition routine needs to be executed only one time. Then the recognition of the every individual frame in the video sequence starts (the right branch of the flowchart). Every frame recognition cycle consists of the adsorbate detection, the lateral drift correction and the assignment of adsorbates to their actual positions on the surface lattice. After the whole video sequence is processed, the output data consisting of the information about the occupation of the surface lattice sites by adsorbates at regular time intervals can be recorded into an ASCII file.

The described image recognition software was developed within this work and implemented on CodeGearTM Delphi ® 2007 environment. The application of the software was tested in about 50 STM video data with different adsorbate species (sulphur, lead, methylthiolate etc.) and showed its good efficiency for high contrast data.

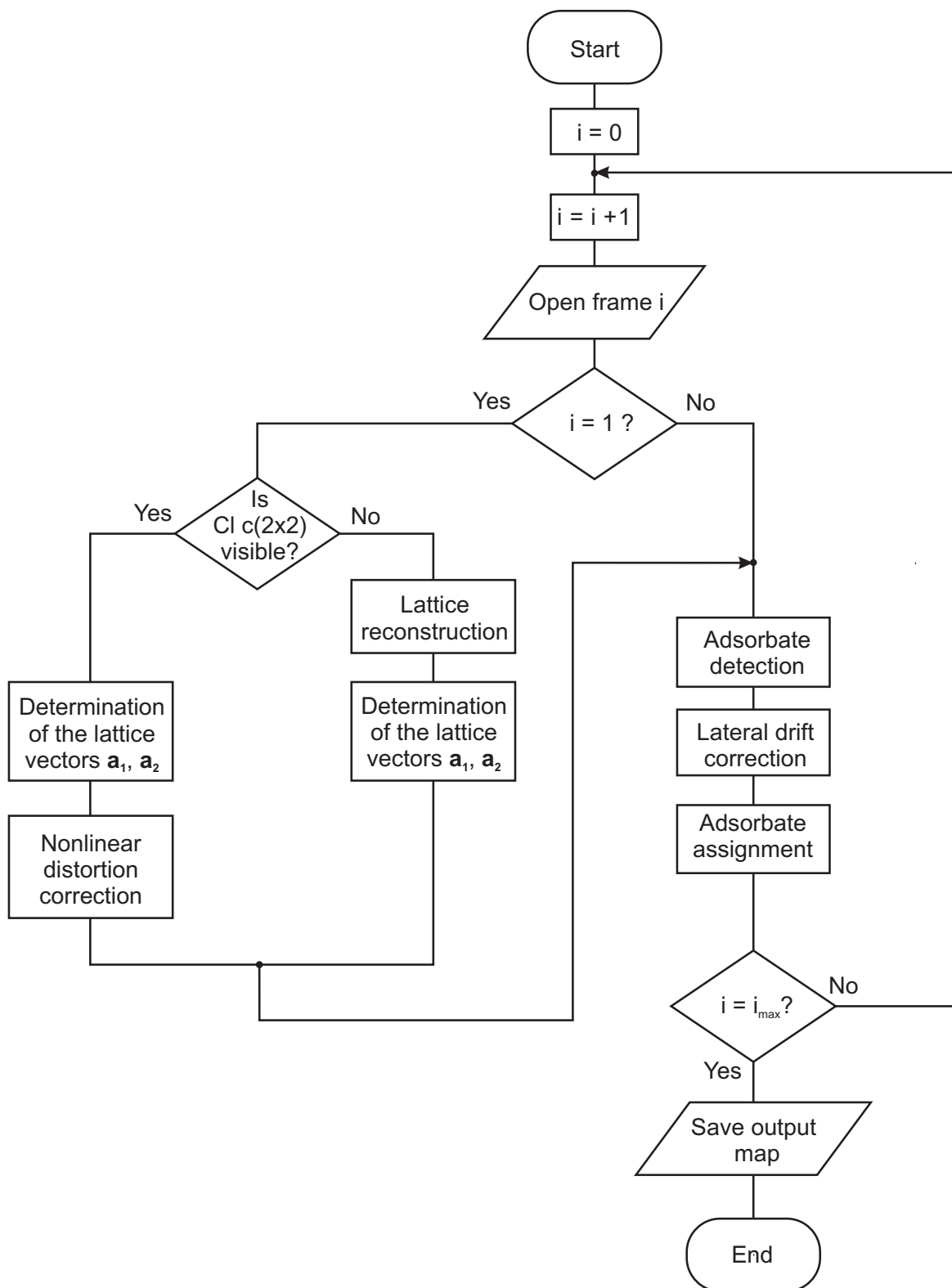


Figure 2.1.: The generalized flowchart of the image recognition processing.

2.1. Adsorbate detection

One of the STM images from a recorded video sequence, which is used as the input data for our computer program, is shown in Fig. 2.2a. The image represents the two-dimensional matrix of pixel height values, obtained by preceding digital processing of raw tunnel current data. We have introduced the coordinate system linked to the STM image with the horizontal axis X and the vertical axis Y, where the axis X is associated with the fast scanning STM tip direction. The size of the images was formatted to be typically 500 pixels \times 500 pixels.

On the image, the S_{ad} appear as white protrusions on the clearly visible Cl $c(2 \times 2)$ structure. This characteristic appearance of S_{ad} was observed in all the video data, while the visibility of the Cl lattice depends on the quality of the data and in some cases may interfere with the proper recognition. Under this condition, a simple and effective method for adsorbate detection consists in the setting of a threshold level for the pixel height (i.e. color brightness). The pixel height profile shown in Fig. 2.2b is obtained along the line segment (marked as dashed in Fig. 2.2a) oriented in [010] direction. Here the pixel height is rescaled between 0 (black color) and 1 (white color).

To choose the proper value of the threshold height one needs to conform to the following rules: i) it should be high enough to make possible the separation of S_{ad} and Cl_{ad} images as well between S_{ad} located at the nearest neighbor sites, ii) on the other hand, with the lowering of this level, the size of recognized S_{ad} in pixels will increase, allowing the determination of their location with better precision and also helping to distinguish them from other arbitrary occurrences on the images such as noise. In general, the threshold level was calculated via the simple relation $h^{tr} = h^{max} - k \cdot (h^{max} - h^{av})$, where h^{max} and h^{av} are respectively the maximum and average values of pixel height in STM image and k is an adjustable parameter which was manually optimized for every video individually, typically in the range 0.2–0.4.

This consideration is valid for the images with homogeneous brightness. In practice, due to the characteristic scanning tip motion (in the center it is closer to the surface than at sides), the brightness could be lower at left and right side of the image than in the middle. To compensate this effect, the threshold level $h^{tr}(x)$ was calculated taking into account the coordinate dependence. First, the image was divided in $N = 5$ to 10 sections along the horizontal axis and the values of h_i^{max} , h_i^{av} , and consequently h_i^{tr} were determined separately for each of these sections. Then the obtained values of h_i^{tr} were approximated by a polynomial function of 3rd order $h^{tr}(x)$, which gives the threshold level depending on

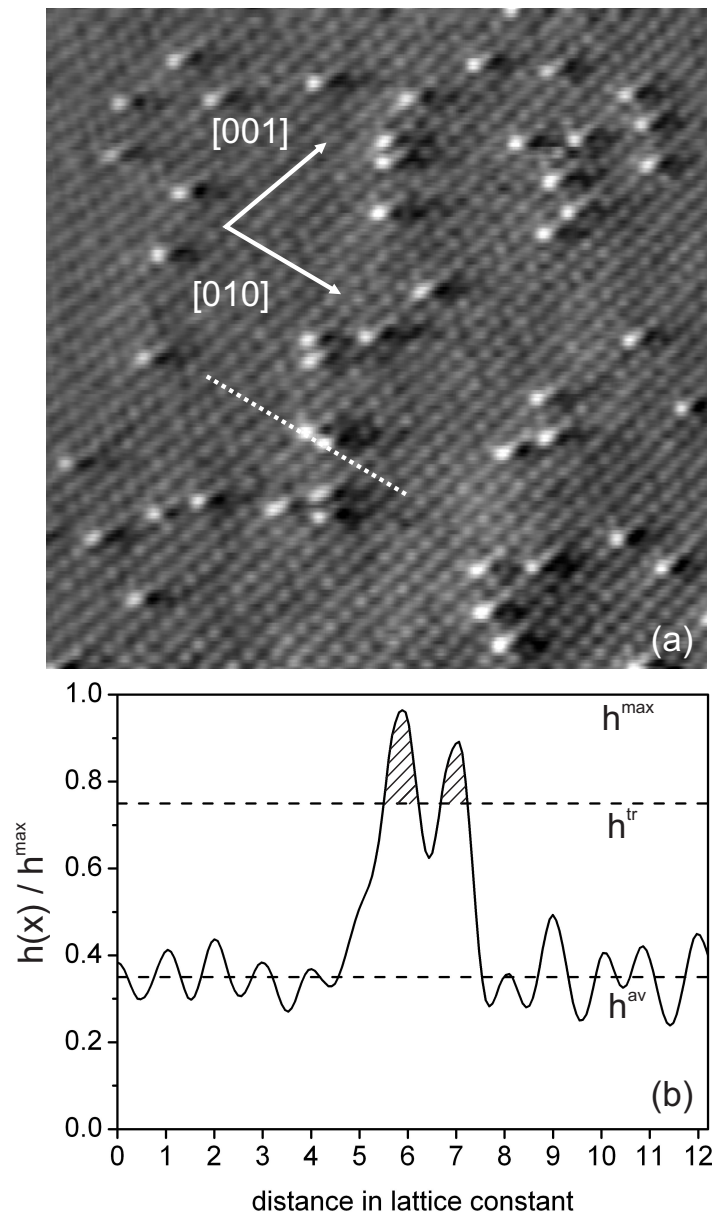


Figure 2.2.: a) Typical STM image representing the S_{ad} distribution on Cu(100) in 0.1 M HCl ($12 \times 15 \text{ nm}^2$, -0.38 V); b) pixel height profile taken in [010] direction. The S_{ad} are identified by the setting of the height threshold level.

the x coordinate.

After that, all the pixels with a height above the threshold level were marked and adjacent ones were joint into groups. In the ideal case, each group of pixels would belong to one individual S_{ad} , but because of such occurrences as noise, high brightness of some Cl_{ad} or groups of S_{ad} located in the vicinity of each other in such a way that their images overlap and can not be distinguished separately, one need to examine groups of pixels additionally. This was implemented by the distribution of the pixel groups into three classes I, II and III according to their area size A_n (measured in pixels) [65]. Two adjustable parameters A_{min} and A_{max} were introduced. Thus, groups of pixels with small area $A_n < A_{min}$ (small size class I) were ignored, groups of pixels with medium area $A_{min} < A_n < A_{max}$ (medium size class II) were selected as corresponding to individual S_{ad} and those with bigger size $A_n > A_{max}$ (big size class III) were redirected to the posterior treatment, which we will consider again after description of the surface lattice recognition. In order to help the user with optimization of the threshold level parameter k and area sizes A_{min} and A_{max} used for the above mentioned selection, the recognized groups of pixels can be shown in separate colors according to their size classes and overlaid on the original image, see Fig. 2.3. On the image, the majority of pixel groups is related to single S_{ad} adsorbates and filled with blue color (medium size), the green pixel group corresponds to a pair of S_{ad} sitting at nearest neighboring lattice sites (big size) and red ones (small size) are related either to some of the Cl_{ad} with high brightness or to S_{ad} partially imaged (at the right and bottom edges of the image).

Besides of area sizes of pixel groups, for further analysis it is necessary to determine their positions on the image. The coordinates x_n and y_n of the center of pixel groups (those which were selected as medium size pixel groups) were calculated as a weighted average, with the weight of each pixel given by its height. This data will play a significant role in the lattice reconstruction and the final assignment of S_{ad} to their lattice sites.

2.2. Surface lattice recognition

The lattice recognition process involves the calculation of lattice vectors, compensation of nonlinear image distortions and lateral drift determination.

For the initial analysis we choose an STM image with clearly visible Cl adlattice (Fig. 2.4a). At low coverages, each sulphur adsorbate substitutes one of the more weakly bound chloride adsorbates from its adsorption site, thus, S_{ad} is still located in $c(2 \times 2)$ superstructure. This statement will be justified below by comparative analysis of both structures – the chloride

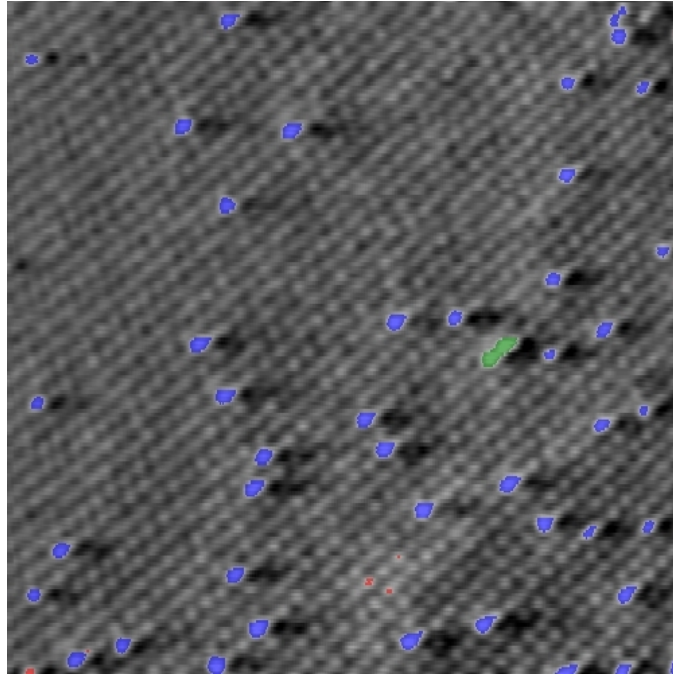


Figure 2.3.: STM image with marked out threshold layer. The recognized pixel groups are painted with the different color according to their size class: red color—small size, blue color—medium size, green color—big size.

adlattice and the structure reconstructed from the positions of the sulphur adsorbates.

The quantitative measurement of lattice vectors, namely \mathbf{a}_1 and \mathbf{a}_2 , was accomplished in the following steps. First, the Fourier transform image (Fig. 2.4b) was obtained from the original STM image by calculation of the Fourier transform function in the two dimensional space [66]:

$$\hat{f}(\xi_x, \xi_y) = \iint f(x, y) e^{-2\pi i(\xi_x x + \xi_y y)} dx dy, \quad (2.1)$$

where $f(x, y)$ is two-dimensional function representing the pixel height in the STM image.

This allows to find the positions of maxima in reciprocal space which correspond to the unit vectors \mathbf{b}_1 and \mathbf{b}_2 of the reciprocal lattice. By inverting those, one can calculate the primitive vectors \mathbf{a}_1 and \mathbf{a}_2 of the adsorbate lattice in the coordinate system connected with the STM image:

$$\mathbf{a}_1 = 2\pi \frac{\mathbf{b}_2 \times \mathbf{b}_3}{\mathbf{b}_1 \cdot (\mathbf{b}_2 \times \mathbf{b}_3)}, \quad \mathbf{a}_2 = 2\pi \frac{\mathbf{b}_3 \times \mathbf{b}_1}{\mathbf{b}_1 \cdot (\mathbf{b}_2 \times \mathbf{b}_3)}. \quad (2.2)$$

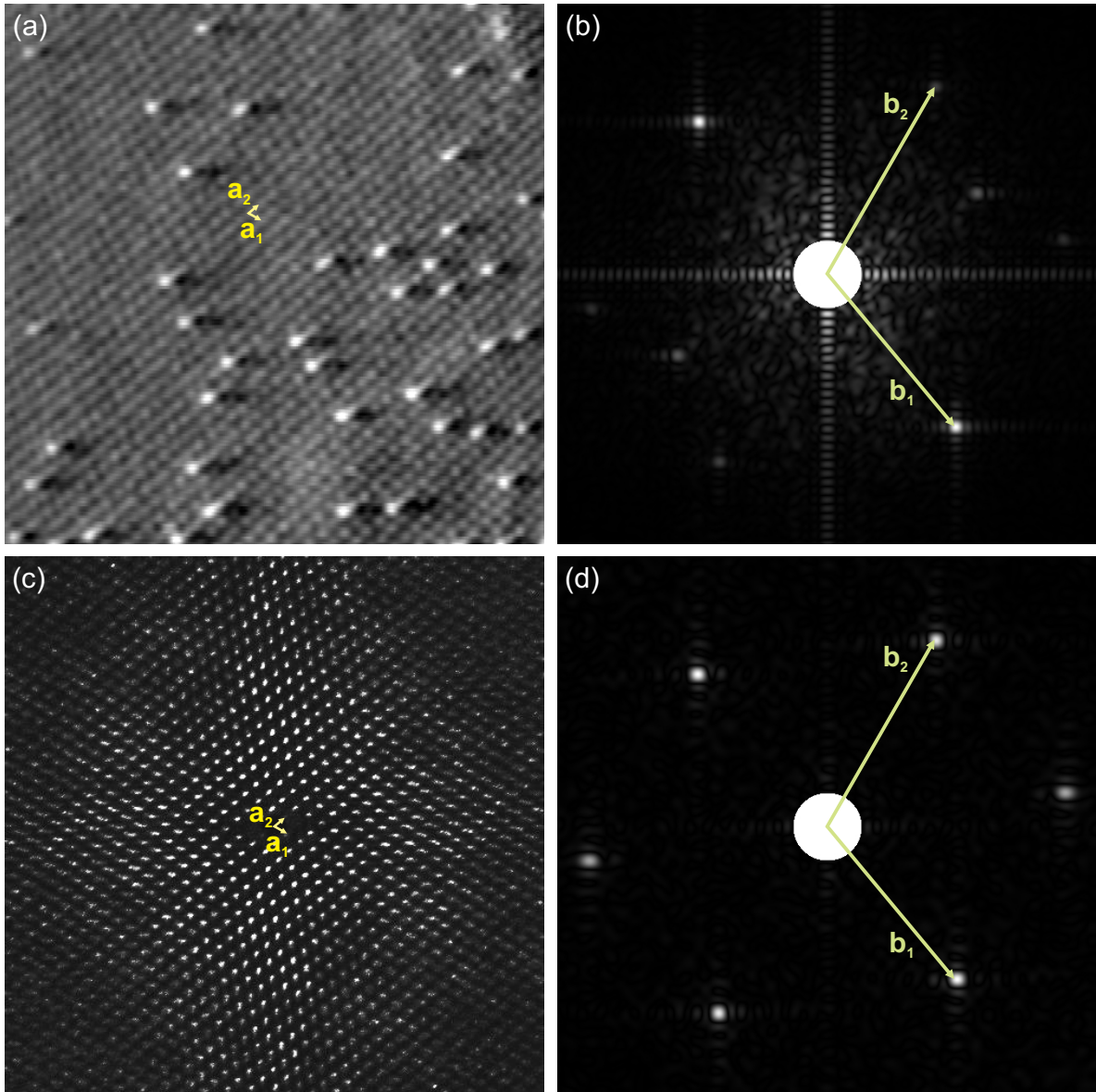


Figure 2.4.: a) STM image showing the well recognized Cl $c(2 \times 2)$ lattice with the primitive vectors \mathbf{a}_1 and \mathbf{a}_2 ; b) the Fourier transformation of the given image. The peaks are related to the unit vectors \mathbf{b}_1 and \mathbf{b}_2 of reciprocal lattice; c) the surface lattice reconstructed from the positions of S_{ad} and d) its Fourier transformation. The comparison proves the identity of both lattices.

Here \mathbf{b}_3 is a unit length vector normal to the image plane and directed to the viewer.

To verify that sulphur adsorbates move within the same $c(2 \times 2)$ lattice, it was reconstructed from the positions of S_{ad} [35, 42, 43]. The relative distances between all the adsorbates were determined for every frame in the video STM sequence and superimposed. The obtained structure together with its Fourier transformation are shown in Fig. 2.4c and Fig. 2.4d, respectively. It is evident, that the positions of maxima in Fig. 2.4b and Fig. 2.4d coincide, thus, the reciprocal unit vectors \mathbf{b}_1 and \mathbf{b}_2 and consequently the real space primitive vectors \mathbf{a}_1 and \mathbf{a}_2 are equivalent for both cases. This procedure provides an alternative way of lattice recognition, which can be the only one applicable in the case of data of lower quality with hardly visible chloride adlattice.

Once unit vectors are known, the positions of all adsorbate lattice sites can be calculated from a periodic structure build by these vectors

$$X(i, j) = X_0 + a_{1x}i + a_{2x}j \quad (2.3)$$

$$Y(i, j) = Y_0 + a_{1y}i + a_{2y}j \quad (2.4)$$

where X_0 and Y_0 are coordinates of the origin of the discrete coordinate system related to the square lattice net (although it looks oblique due to a tilt and a compression of the image), i and j are discrete coordinates in this coordinate system. The coordinates X_0 and Y_0 of the origin were determined for every frame in the sequence taking into account the lateral drift of the scanning area as discussed below. To improve the determination of lattice site positions, the non-linear distortion of the STM images in the fast scanning direction was considered. While in the central part of the image it doesn't result in significant discrepancies between calculated coordinates of lattice sites and their positions in the STM image, at the left and right edges of the image it may increase the risk of S_{ad} assignment to wrong lattice sites. As a solution, equation 2.3 was modified by adding the correction function $O(x)$:

$$X(i, j) = X_0 + a_{1x}i + a_{2x}j + O(x). \quad (2.5)$$

To evaluate the correction function $O(x)$, the automated algorithm reproduces the curve shape of the atomic rows either in $[010]$ or $[001]$ directions by stepwise scanning in the chosen direction and the determination of the coordinates of the adsorbates, Cl as well as

S, in the given row. These coordinates were obtained by search of local maxima heights, i.e. the centers of adsorbates. Y coordinates were represented as a function of X coordinates which was approximated by polynomial functions of the 3rd order. For the reliable work of this procedure, it is important to ensure the following conditions: i) one needs to chose the atomic row in the STM image with the largest amount of adsorbates, and correspondingly data points; ii) the values of X and Y coordinates of the adsorbates in the chosen row has to be in a range which is as wide as possible, to provide a better quality of the fit. The atomic rows located in the diagonal of STM image, or close to it, would satisfy these conditions. Then, the correction function $O(x)$ was obtained by subtracting the non-distorted line, directed parallel to the corresponding unit vector and coinciding with atomic the row in the center of the image, from the polynomial fit function. Obviously, this option can be applied only if the chloride pattern is clearly visible. Nevertheless, the absence of the nonlinear correction may cause errors in the determination of the adsorbate positions usually only close to the borders of the image. The exact location of those adsorbates is not that important, however. Since the local distribution of other adsorbates around them is partially out of our view, they can not be taken into account in the quantitative analysis.

2.3. Lateral drift correction

In addition to the scanning motion, the STM tip performs slight lateral drift, so that the scanning area is shifting with time in arbitrary directions during the experiment. This drift is much slower than the complete scanning of one frame, but has to be taken into account for the sequence of frames in one video. It means, that the locations of lattice net positions (obtained via eqs.2.4-2.5 from coordinates of X_0 and Y_0 of the lattice origin) have to be recalculated for each frame in the video sequence providing the best fit to the centers of S_{ad} pixel groups (x_n, y_n) . In other words, one needs to minimize the squared sum of the distances between the centers of S_{ad} pixel groups (x_n, y_n) and the lattice net sites $(X(i_n, j_n), Y(i_n, j_n))$, located at the closest distance to them :

$$\sum_{n=1}^{N_{ad}} R_n^2 = \sum_{n=1}^{N_{ad}} [(X(i_n, j_n) - x_n)^2 + (Y(i_n, j_n) - y_n)^2]. \quad (2.6)$$

The given optimization is performed by varying the coordinates X_0 and Y_0 of the lattice origin, the coordinates $(X(i_n, j_n), Y(i_n, j_n))$ were calculated via the equations 2.4 and 2.5. For the first frame in the video sequence, the starting values of X_0 and Y_0 for the fitting

routine were determined as the coordinates of the center of the image. Therefore, after initial run of the fitting procedure, one of the lattice sites in the center will be set as origin. For each next frame, the starting values for X_0 and Y_0 are taken from the old coordinates of the origin in the previous frame, thus, the routine will trace the shift of the initially chosen origin.

During the fitting there is a certain chance, that the origin of the lattice net may move away from its initial position by one lattice distance or even more. This would cause the assignment of S_{ad} to wrong lattice positions and consequently detection of large amounts of false jumps. To exclude this artefact, the coordinates of the lattice site which are the most close to the coordinates of origin in the previous frame were chosen as the position of the origin in the new frame.

The successful application of this method has well-defined limits: for two successive frames the components of the lateral drift in the directions of unit vectors should be less than half of the corresponding lattice distances. Nevertheless, for all the videos processed, the given condition was wholly satisfied.

The result of the adjustment by means of a grid search algorithm is shown on the Fig. 2.5a. The overlaid dotted pattern represents the lattice positions, the atomic rows with $i = 0$ and $j = 0$ plotted in blue color. As could be seen, for the most of S_{ad} the lattice points lie very close to the centers of the S_{ad} shapes, which is a good sign for the correct recognition. Certainly, one can notice that at the edges and especially in the bottom part of the given image the lattice points mismatch with the chloride lattice, but, what is more important, they are located in the vicinity to the S_{ad} centers. Thus, for most of the cases, the error in the calculation of the lattice sites positions is still less than critical for the correct adsorbate registration.

2.4. Adsorbate assignment

When the coordinates of the centers of S_{ad} are determined and the lattice net is adjusted well, the final step in the recognition process is to register each of the S_{ad} to the closest lattice site. In such a way, we create a binary lattice map, containing the information about the arrangement of the adsorbates on the surface (Fig. 2.5b). The recognition process, repeated for each frame in the video, gives as output the sequence of binary maps at regular time intervals. These data will be used in the following quantitative studies of adsorbate tracer diffusion and adsorbate-adsorbate interactions described in the next sections.

Up to now the treatment was applied only to those S_{ad} which have passed through the

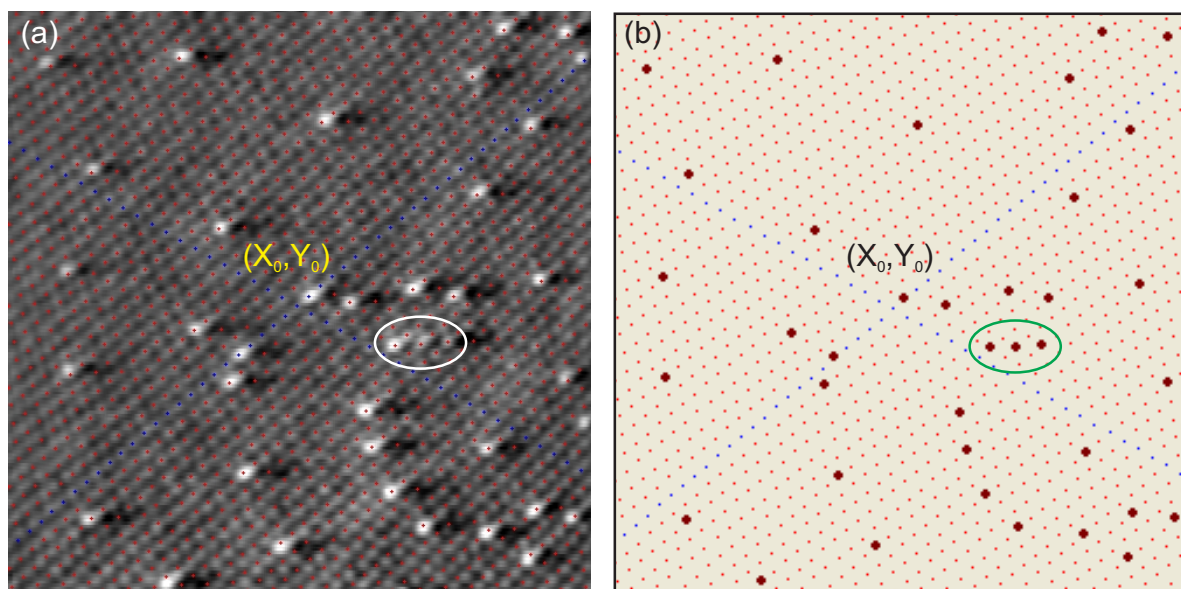


Figure 2.5.: a) STM image with the lattice net adjusted to the positions of sulphur adsorbates; b) the binary output map reflecting the distribution of S_{ad} (red dots) on the given image. The origin of the discrete coordinate system is located on the intersection of the lattice sites rows painted in blue color.

sifting with a clearly visible appearance of single adsorbates. The cases, when two or more adsorbates sit at close positions and their images overlap so that they can not be recognized separately, were excluded in the lattice recognition. Particularly, the center of two 'merged' shapes of adsorbates will lie between them and its coordinates would cause undesirable errors in the lattice adjustment. Nevertheless, the determination of the locations of atoms in such groups is still of interest, especially for the case of two adsorbates, since this information is important for the measurements of the pairwise interactions. As a simple automatic solution for this problem, the local area of such spots was divided by Wigner-Seitz cells, i.e., the locus of points on the image that are closer to a certain lattice point than to any other lattice points (see the schematic drawing on Fig. 2.6). Then if a considerable part (more than 70%) of the individual cell is covered by the recognized pixel group, the program will register the adsorbate to this lattice position. The accuracy of this method is moderate, but it is still significantly helping the user to conduct the recognition process.

Depending on the quality of the video data, the automated procedure allow the recognition of 95-98% of the adsorbates presented on the image. In addition, the computer program gives the opportunity of manual corrections inasmuch as according to our belief

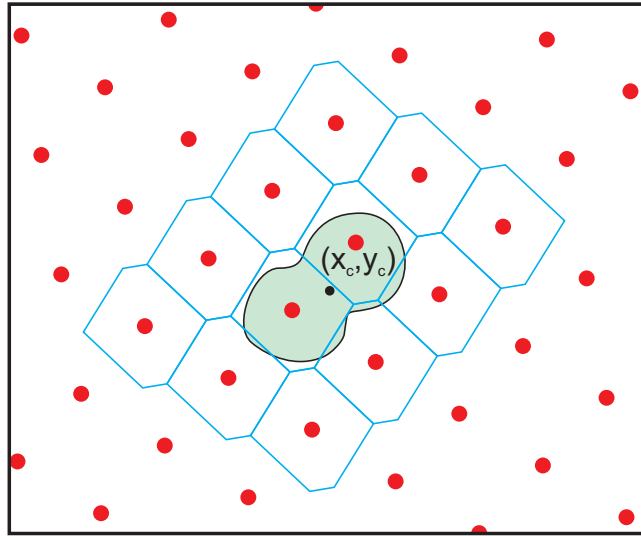


Figure 2.6.: Schematic representation of the recognition of the big size pixel group formed by the merging of the images of the two adsorbates sitting at nearest neighbor sites. The local area is divided into Wigner-Seitz cells, those cells which are considerably covered by pixel group will be registered as occupied by adsorbates.

no computer algorithm can work better than a human eye. The user can scroll STM images simultaneously with the corresponding binary maps and make the final decision to add or delete adsorbates on them. For example, the ellipse on the Fig. 2.5 indicates a row of the three S_{ad} oriented in $[011]$ direction, but only the one of them which is at the left side was detected automatically. Two other S_{ad} with reduced color height influenced by the typical 'shadow' from the first S_{ad} were skipped. Careful checking of the previous and next STM images confirmed that the central and left positions are also occupied with S_{ad} and the necessary correction was done manually.

Events which present severe difficulties even for the recognition by the user could happen with a certain frequency as well. One example is when a group of 5 and more adsorbates, located in the vicinity of each other and correspondingly moving with increased mobility, merges in STM images in one big white group of pixels. Such occurrences, which can not be treated unambiguously, were completely excluded in the following quantitative analysis.

3. Quantitative measurements of adsorbate-adsorbate interactions

It is worth to remember, that all the measurements of adsorbate-adsorbate interactions mentioned above were performed under UHV conditions. In our group, similar methods were adopted for comparable studies in the electrochemical environment for the first time. In the last years, pair interactions were obtained from series of experiments by high speed STM respectively for sulphur, lead and methylthiolate adsorbates on Cu(100) surface in aqueous solution of 0.01 M HCl.

The first two sections of this chapter will give a description of both quantitative methods for the calculation of the interatomic potentials illustrated by their application to one of the experimental data. In the next chapters we will present the results of interatomic energies and mobility for sulphur and lead adsorbates, respectively, obtained by analysis of the experimental data recorded at various electrode potentials.

3.1. Dynamic analysis

In the most simple case an isolated adsorbate within the square lattice performs random walk motion. The activation barriers and consequently the jump rates are equivalent in all four directions to the neighbor sites. As an isolated sulphur adsorbate we consider one which is separated from all other sulphur adsorbates by a sufficient distance when the interactions between them can be neglected. The previous study of S_{ad} tracer diffusion by Tansel [1] showed that the hopping rates of S_{ad} were significantly influenced when the distance to a neighbouring S_{ad} becomes less than $4a_0$ [1, 61, 70].

At close distances between adsorbates, the local energy landscape—the adsorption sites energies and the saddle point energies—is modified by the interactions between the adsorbates, affecting their motion. In such case, the motion of adsorbates is not isotropic anymore, since the probability of the jumps in certain directions depends now on the initial and final positions of particles. Studying the mutual motion of the adsorbates one can extract the modifications to the diffusion barriers caused by the interactions.

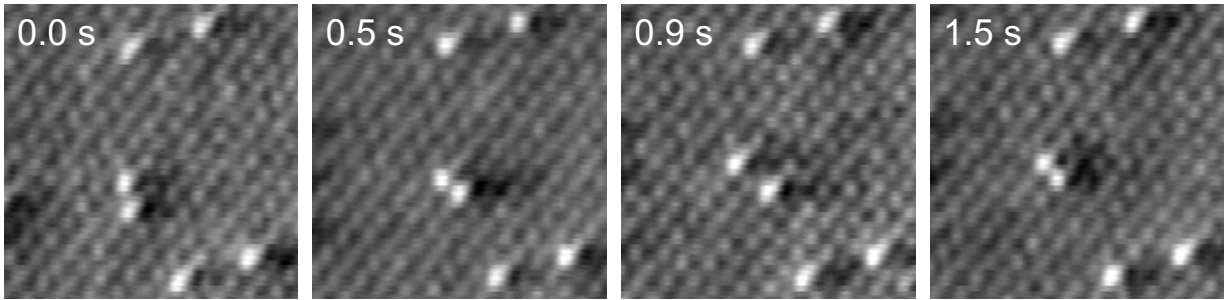


Figure 3.1.: Selected STM images ($50 \times 50 \text{ \AA}^2$) illustrating the enhanced dynamics of S_{ad} dimer (shown in the center of images). During the recording of the image the adsorbates forming the dimer performed jumps few times while the other S_{ad} remain at their initial positions.

To determine a pairwise interaction potential we have studied the motion of isolated dimers—pairs of the S_{ad} located close to each other and isolated from all other S_{ad} , so that they interact only between each other. They should be separated from other sulphur adsorbates by distance not less than $4a_0$, at the same time, their own separation should not exceed this value. It is clear that dimers located at a distance closer than $4a_0$ from the borders of the STM image, are not suitable for consideration. In addition, dimers should be separated at least by the given distance from steps, domain boundaries or other imperfections on the surface lattice such as impurities. A pair of S_{ad} which satisfies all conditions while changing its relative configuration is shown on the Fig. 3.1 in the center of each image in the sequence. One can notice the influence of the adsorbate interactions on their mobility: during the time of observation equal to 1.5 s the pair of S_{ad} performed a few jumps, while the other adsorbates remained at their positions.

For the statistical analysis, the changes in the relative configurations of the isolated dimers in the adjacent frames were assembled for the whole video sequence and grouped together according to the fourfold symmetry [42]. This results in the determination of a set of two-dimensional particle jump distribution functions, one per every configuration with initial separation r_k between adsorbates ($r_k = 1a_0, \sqrt{2}a_0, 2a_0, \sqrt{5}a_0, 2\sqrt{2}a_0$; here index k is numbered according to the distance between the sulphur adsorbates). Each jump distribution function gives the probability to find the new configuration in the next frame, i.e. after a time interval Δt . All five histograms are shown on the Fig. 3.2 as dark blue columns. The red circles indicate the initial configuration of the dimer for which the histogram was plotted. Each histogram with the total statistic counting usually in the order of few hundreds up to thousand of observations contains about 9-20 data points. The

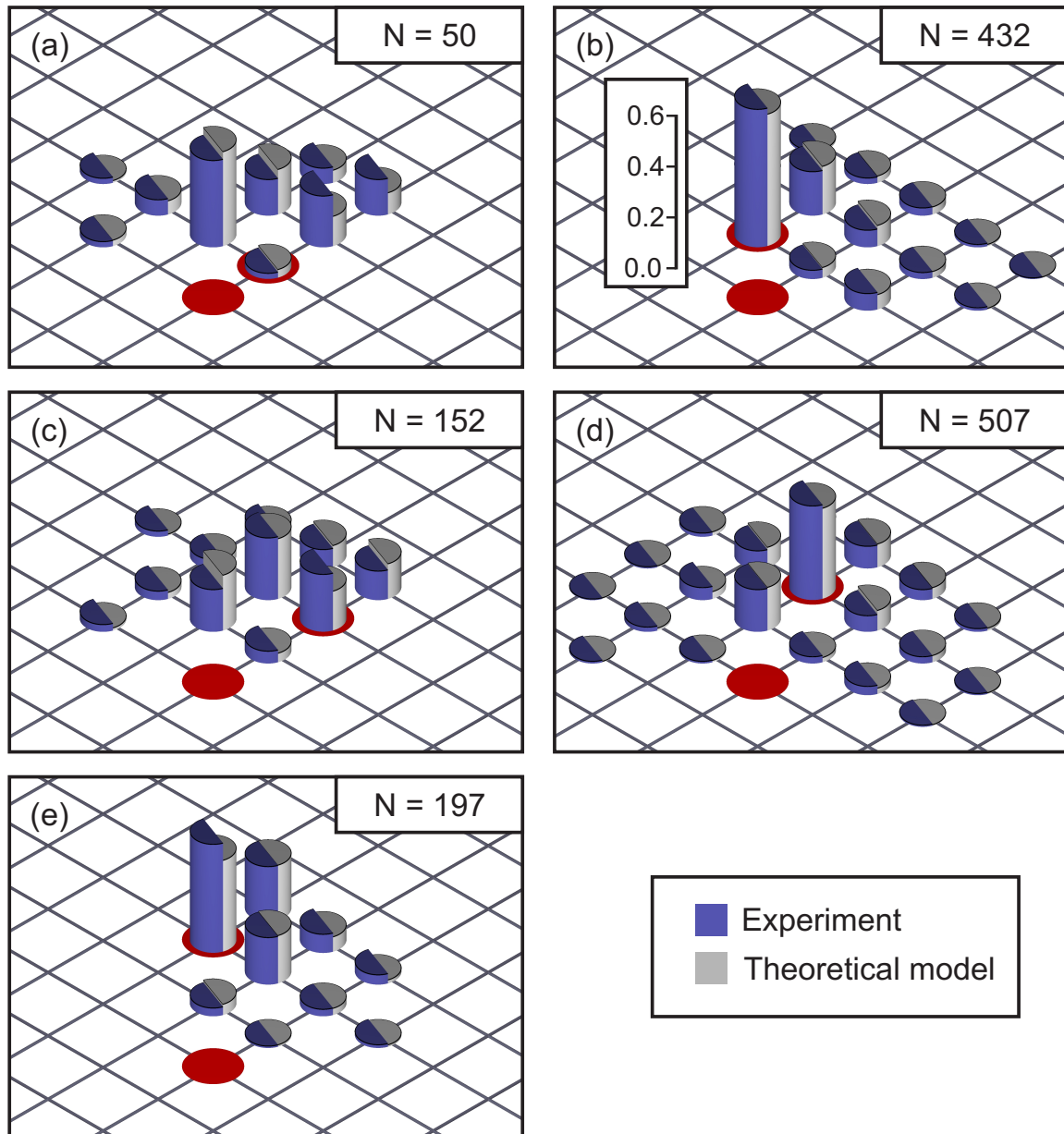


Figure 3.2.: Two-particle jump distribution functions for a) $1a_0$, b) $\sqrt{2}a_0$, c) $2a_0$, d) $\sqrt{5}a_0$, e) $2\sqrt{2}a_0$ initial configurations (dark blue bars—experimental values with the N total number of observations, light grey bars—fit model). The corresponding scale for the probability values is shown on b). The experimental data were recorded at $-0.47 V_{SCE}$.

given experimental distributions were normalized by the total number of observations for the respective configuration N_k^{exp} . The absolute values of obtained distribution histograms may be estimated by comparison of corresponding column heights with the scale presented in Fig. 3.2b. Here it is also worth to mention, that the given histograms for the initial configurations $r_k = 1a_0, \sqrt{2}a_0, 2a_0$ and $2\sqrt{2}a_0$ were assembled from 4 symmetrically identical configurations, whereas for the case $r_k = \sqrt{5}a_0$, 8 identical configurations exists. Therefore, for the direct comparison of statistic counting N_k^{exp} for this histogram with the others its value has to be divided by factor of 2.

Preliminary comparison of the given histograms, suggests that the adsorbate sites are not equivalent. The different values of the total number of observations when adsorbates are located at the nearest sites (50) and the next-nearest sites (432) indicates that the next-nearest configuration occurs more frequently so it is more favorable. This is additionally confirmed by the shape of the histograms. In the case of the next-nearest neighbor configuration, it has the highest probability to remain in the same initial dimer configuration in the following frame, while for the nearest neighbor configuration, such probability is very low, moreover, the the highest probability in this case still corresponds to the next-nearest position. Consequently, the next-nearest neighbor configuration is more stable than the nearest one.

To describe theoretically the motion of one adsorbate in the close neighborhood of another one, we have introduced the following model scheme (see Fig. 3.3). Due to the influence by the interaction with another coadsorbate, at each atomic separation, S_{ad} has a certain modified value of the adsorption energy E_i . For values $i \geq 5$, the values E_i were chosen to be identical to the adsorption energy of the isolated S_{ad} .

In the analysis of adsorbate motion, we consider only the atomic jumps between the nearest sites. In order to accomplish the jump from the site i to one of the neighboring site j , the adsorbate must move across a higher energetic state which is characterized by some value of the saddle point energy E_{ij}^S . Thus, the activation energy or the 'diffusion barrier' of this jump is given by

$$E_{ij}^D = E_{ij}^S - E_i. \quad (3.1)$$

All saddle points are presented schematically as crosses in Fig. 3.3. Similarly to the case of the adsorption sites energies, starting from the value E_{47}^S and for all the saddle points for which the condition $(i + j)/2 > 5$ met, the values of the saddle point energies E_{ij}^S

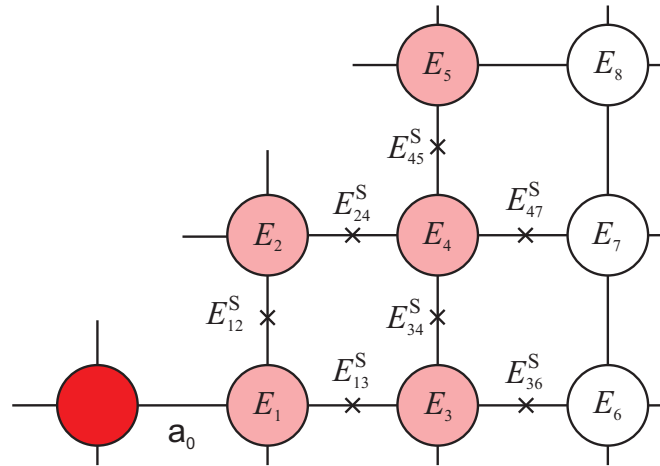


Figure 3.3.: Schematic model of the modified energy landscape in the square lattice, consisting of the adsorption sites and saddle point energy values

are assumed to be not modified by the interactions and set to be 0 for convenience. As follows from this definition, the diffusion barrier for an isolated particle is given then by $E_{\infty}^D = -E_5$.

According to transition state theory [67, 68], the hopping rates in the direction of the jump are given by

$$\gamma = \gamma_0 \cdot e^{-E^D/k_B T}, \quad (3.2)$$

where γ_0 is an attempt frequency, $k_B = 8.617385 \times 10^{-5}$ J/K is the Boltzman constant and $T = 291$ K is the temperature. The absolute value of attempt frequency $\gamma_0 = 2.35 \times 10^{12} \text{s}^{-1}$ was obtained from the Arrhenius fit of the data in the study of the tracer diffusion of isolated S_{ad} in the experiments at 277-296 K temperature regime [1]. All together we have a set of the 11 independent parameters (5 adsorption sites energies E_1, E_2, E_3, E_4, E_5 and 6 saddle point energies $E_{12}^S, E_{13}^S, E_{24}^S, E_{34}^S, E_{36}^S, E_{45}^S$) which describe the spatial modulation of the energy landscape on the surface by the coadsorbate. In such a way, the values of 14 jump rates between the neighboring sites calculated from the given energies will be used to describe the dynamic behavior of the pair of S_{ad} .

A master equation derived for the case of the relative motion of two particles [42, 43] can be used to calculate the probability $p(\mathbf{r}_i)$ to find a dimer with a relative distance vector \mathbf{r}_i :

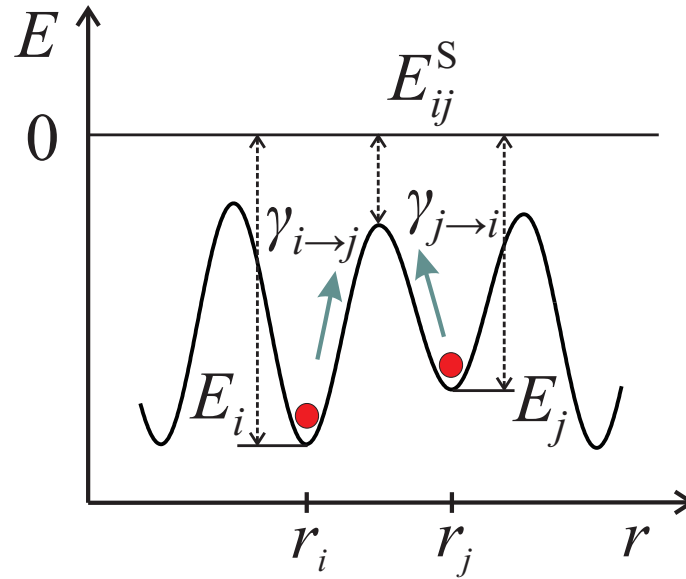


Figure 3.4.: Schematic illustration of the activation diffusion barriers between the neighbouring sites

$$\begin{aligned} \frac{\partial}{\partial t} p(\mathbf{r}_i) = & \sum_{\mathbf{r}_j=NN(\mathbf{r}_i)} [\gamma(\mathbf{r}_j, \mathbf{r}_i) + \gamma(-\mathbf{r}_j, -\mathbf{r}_i)] p(\mathbf{r}_j) \\ & - p(\mathbf{r}_i) \sum_{\mathbf{r}_j=NN(\mathbf{r}_i)} [\gamma(\mathbf{r}_i, \mathbf{r}_j) + \gamma(-\mathbf{r}_i, -\mathbf{r}_j)], \end{aligned} \quad (3.3)$$

where $NN(\mathbf{r}_i)$ denotes the displacement to the nearest neighbor sites of \mathbf{r}_i ; $\gamma(\mathbf{r}_j, \mathbf{r}_i)$ is the rate at which an adsorbate located at a distance \mathbf{r}_j from the other adsorbate jumps to a distance \mathbf{r}_i and can be calculated from the set of the introduced energy parameters (see Fig. 3.4):

$$\gamma(\mathbf{r}_i, \mathbf{r}_j) = \gamma_0 e^{-\frac{E_{ij}^s - E_i}{kT}} \quad (3.4)$$

The total jump rate out of the site, or the inverse residence time at this site, is the sum of the jump rates to all neighboring sites:

$$\Gamma(\mathbf{r}_i) = \sum_{\mathbf{r}_j=NN(\mathbf{r}_i)} \gamma(\mathbf{r}_i, \mathbf{r}_j) \quad (3.5)$$

Taking into account the symmetry, eq.(3.3) can be rewritten as

$$\frac{\partial}{\partial t} p(\mathbf{r}_i) = \sum_{\mathbf{r}_j=NN(\mathbf{r}_i)} 2\gamma(\mathbf{r}_j, \mathbf{r}_i)p(\mathbf{r}_j) - p(\mathbf{r}_i) \sum_{\mathbf{r}_j=NN(\mathbf{r}_i)} 2\gamma(\mathbf{r}_i, \mathbf{r}_j). \quad (3.6)$$

Eq.(3.6) was solved numerically separately for every initial dimer configuration \mathbf{r}_k resulting in 5 theoretical jump distribution functions for the respective configurations. The solution was obtained by applying the Euler scheme [69] on a discrete square slab with a size of 100×100 sites. The total simulation time was equal to the time interval between the adjacent STM frames Δt .

The initial distribution for each separate configuration was set by

$$p_k(\mathbf{r}_i) = \begin{cases} 1 & \text{if } \mathbf{r}_i = \mathbf{r}_k \\ 0 & \text{if } \mathbf{r}_i \neq \mathbf{r}_k \end{cases} \quad (3.7)$$

The dimensions of the slab are much bigger than the characteristic length for the isolated adsorbate diffusion $\sqrt{D\Delta t}$, where

$$D = \frac{1}{4}\Gamma a_0^2 \quad (3.8)$$

is a tracer surface diffusion coefficient, Δt is the time interval between the following frames (typically 0.1 s). Taking into account that the hopping rates for isolated adsorbates Γ in our experiments are in the range of 0.1–10 s⁻¹, one can estimate the characteristic length to be about 0.05–0.5 a_0 . This allows us to consider the computation cell as 'infinite'. In such a way, as the boundary conditions for simulation slab, we can set up the values of the probability function outside of the slab to be equal to zero. The tracking of the values of the total probability flux through the computation cell borders during the simulation process showed that its value remains negligibly small for the given simulation time and hopping rates, what confirms our assumption.

Then the theoretical histograms calculated for the five different initial configurations of dimer ($1a_0$, $\sqrt{2}a_0$, $2a_0$, $2\sqrt{2}a_0$, $\sqrt{5}a_0$) were fitted simultaneously to the respective experimental histograms by the variation of the values of the free energy parameters—adsorption sites energies and the saddle point energies. To provide the best adjustment of the theoretical distributions to the experimental ones, the so called weighted Least Square Method was applied. For each separate initial dimer configuration \mathbf{r}_k , the sum of the squared differences between the experimental and the theoretical jump probability distribution functions was

obtained:

$$f_k = \sum_{\mathbf{r}_i} \frac{1}{\sigma_i^2} (p_k^{teor}(\mathbf{r}_i) - p_k^{exp}(\mathbf{r}_i))^2, \quad (3.9)$$

with a weighted factor $1/\sigma_i^2$, where the experimental error σ_i of the measurement is considered to be a statistical error:

$$\sigma_i = \frac{\sqrt{n_i^{exp}}}{N_k^{exp}}. \quad (3.10)$$

Here $n_i^{exp} = p_k^{exp}(\mathbf{r}_i) \cdot N_k^{exp}$ is the experimental number of observations of a dimer configuration \mathbf{r}_i in the separate experimental histogram obtained for the initial dimer configuration \mathbf{r}_k , and N_k^{exp} is the total number of observations for a given experimental histogram.

Now the overall parameter which has to be optimized was calculated as the sum of the contributions from the separate histograms:

$$F = \sum_k f_k. \quad (3.11)$$

For the sake of convenience, let us consider the total set of 11 energy parameters which includes the set of 5 adsorption sites energies E_i and the set of 6 saddle point energies E_{ij}^S and denote its components by E_x , where $x = 1 \dots 11$. Then, the position of the minimum in such a free parameter space correspond to the condition

$$\frac{\partial F}{\partial E_x} = 0, \text{ for each } x. \quad (3.12)$$

Its location was determined by using the grid search algorithm [71], with the consecutive minimization of F in every iteration of the method by independent variation of each energy parameter. The obtained values of energy parameters in this minimum correspond to the measured values of these parameters. The confidence limits for these parameters were calculated from the local curvature of F at the minimum point [71]:

$$\sigma_{E_x}^2 = \frac{2}{\frac{\partial^2 F}{\partial E_x^2}}. \quad (3.13)$$

The theoretical jump probability distributions fitted to the corresponding experimental data are shown in Fig. 3.3 as the light blue columns. For the given data set, the reduced chi-square, i.e. the parameter F divided by the number of degrees of freedom (the difference between the total number of the data points and the number of free variables plus one constant term) was equal to 1.04, indicating the goodness of the fit.

The extracted values of adsorption sites energies E_i merge various potentials—the binding energy of an adatom on the crystal plane and the interatomic potential energy between two adatoms $V_{pair}(r_i)$ [31, 72]. According to the assumption that $V_{pair}(r_5) = 0$, the value of the potential of pairwise interactions $V_{pair}(r_i)$ for each distance r_i can be calculated as a difference of the adsorption energy E_i for a given site and the value for the adsorption energy of the isolated particle which is equal to E_5 :

$$V_{pair}(r_i) = E_i - E_5. \quad (3.14)$$

The calculated values of the pairwise interaction potential $V_{pair}(r_i)$ obtained by the fitting of the described theoretical model to the experimental histogram data, presented in Fig. 3.2, are plotted in Fig. 3.5 as a function of the distance between the S_{ad} . The potential has an oscillating behavior due to its dependence on the lattice direction. The most distinctive is the repulsion on nearest neighbor sites and attraction at the next nearest neighbor sites with values on the order of a few 10 meV. These interactions are small but important since they are on the order of $1/2k_B T$.

Finally, it is worth to mention that our choice of energy parameters as fitting variables is slightly different from the original idea proposed by Renish et al. [42, 43]. In their case, during the fitting the jump frequencies were varied independently, while the additional constraints need to be applied to fulfill the detailed balance condition. As the result, multiple values of the interatomic potentials at certain positions, depending on the paths these positions can be reached, were obtained [3]. Our method is devoid of this disadvantage, although the determination of the minimum has to be very accurate. The jump rates which are included in master equations depend exponentially on changes in the energy parameters. Therefore, the least square parameter in eq.(3.9) is very sensitive to the variations in the energy values.

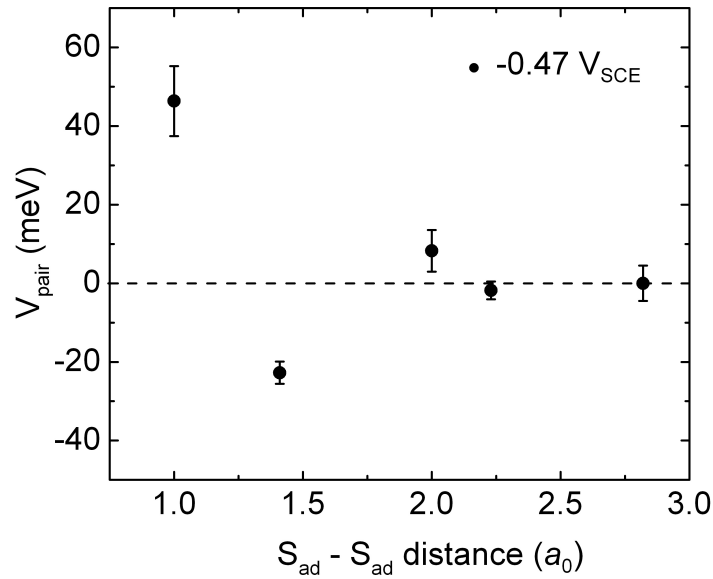


Figure 3.5.: Pairwise $S_{ad} - S_{ad}$ potential $V_{pair}(r_i)$, obtained from the analysis of S_{ad} dimer motion at $-0.47 V_{SCE}$.

3.2. Equilibrium analysis

As was already observed in the previous section, the occupation of the lattice sites by adsorbates in the presence of interactions between them is different from a stochastic distribution. For large separations between the adsorbates, i.e., out of range of the interactions between them, the probability to find an adsorbate at the certain distance r_i of another adsorbate is uniform value and equal to the surface coverage of the adsorbates. At shorter distances, when the interactions start to play a significant role, this probability will be higher than the average value for sites corresponding to attractive interactions and lower for repulsive interactions, respectively.

The equilibrium method of the determination of adsorbate-adsorbate interactions is based on the calculation of the adsorbates pair correlations. The radial pair correlation function is defined as the probability to find an adsorbate at a certain distance r_i from the other adsorbate at the same time moment, normalized by the surface coverage of the adsorbates $\theta_{c(2 \times 2)}$ determined relative to the lattice sites of the Cl $c(2 \times 2)$ adlayer:

$$g(r_i) = \frac{p(r_i)}{\theta_{c(2 \times 2)}}. \quad (3.15)$$

The commonly used adsorbate coverage θ with respect to the Cu atoms in the (100)

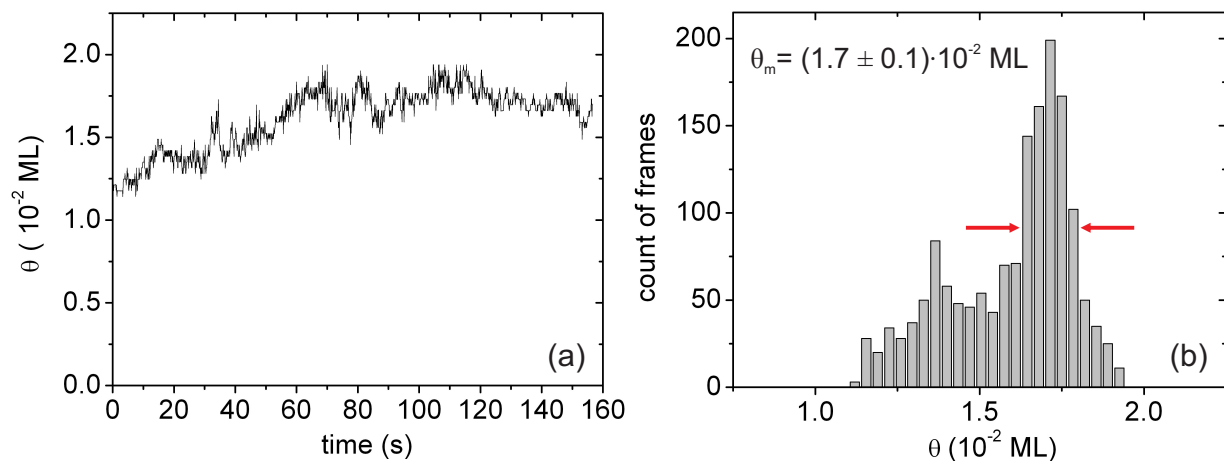


Figure 3.6.: a) Surface coverage fluctuations during the experiment time and b) corresponding distribution of STM frames by surface coverage. Red arrows on b) indicate the selected coverage interval of STM images used in the further analysis.

plane is given then by $\theta = \theta_{c(2 \times 2)}/2$. The probability function $p(r_i)$ can be determined from the available experimental data by the statistical evaluation of the spatial adsorbate distributions:

$$p(r_i) = \frac{N(r_i)}{wN_0}, \quad (3.16)$$

here $N(r_i)$ is the number of S_{ad} observed at distance r_i from another S_{ad} , N_0 is the total number of observations, w is the geometrical factor equal to the number of symmetrically equivalent configurations for the corresponding separation of r_i between the adsorbates (on the square lattice, $w = 4$ for the [001] and [011] directions and $w = 8$ for all other directions). Analysis showed that the numbers of adsorbate observations separated by a certain distance r_i have comparable values within the statistical errors, independent of the relative adsorbate orientations. Thus, a possible influence on adsorbates by the scanning tip, which would result in their anisotropic distributions, was not observed.

According to eq.(3.15), the distribution of non-interacting particles is characterized by a value of $g(r_i) = 1$. The deviations from unity to higher or lower values show the existence of attractive or repulsive interactions respectively.

For interacting species, $g(r_i)$ depends on the surface coverage, that is why to perform a quantitative analysis it is necessary to select experimental data with a similar surface coverage. Since the size of the scanning area is rather small, typically on the order of $100 \times 100 \text{ \AA}^2$, the surface coverage of adsorbates can fluctuate significantly during the time

of the experiment, as shown in the example in Fig. 3.6a. These fluctuations are caused by the diffusion of the adsorbates through the borders of the scanning area as well as the lateral drift of the STM tip. Events related to the adsorption or desorption of atoms, which would manifest in a sudden appearance or disappearance of adsorbates on the surface, respectively, while their mobility is sufficiently low to trace the motion of each adsorbate, were never observed in our experiments. The coverage histogram, which corresponds to Fig. 3.6a, is plotted in Fig. 3.6b. For the given data set, a narrow interval of surface coverages around the average value $\theta_m = (1.7 \pm 0.1) \times 10^2$ ML, which is related to the higher peak (marked on the plot by arrows), was selected for the determination of the pair correlation function. Consequently, the adsorbate distribution were assembled only from the images with the adsorbate coverage lying within the selected range.

The adsorbate distributions on the lattice sites were calculated in the local area around each adsorbate, limited by the range of adsorbate interactions, i.e, $4a_0$, which is the same as in the previous method (Fig. 3.7a). Here however, the contribution of each pair of adsorbates was counted as compared to the dynamic analysis where only isolated dimers were considered. This results in a significant increase of the number of statistical data which are typically in the range of 3000 to 50000 of individual adsorbate observations depending on the experimental data. As in the previous method, adsorbates located at distances smaller than $4a_0$ from the edge of the visible scanning area were excluded from the further analysis.

The pair correlation function $g^{exp}(r_i)$ calculated for the given experimental data recorded at -0.47 V_{SCE} is presented in Fig. 3.7b by the dark blue bars. Its shape confirms the already observed tendency for adsorbate interactions: the next-nearest sites are occupied with higher probability than for the case of a random distribution, while the nearest sites are less favorable. The magnitude of interactions is decreasing fast with the distance and already at separations larger than $3a_0$ its value can be neglected. This additionally confirm our consideration about the range of interactions.

In order to calculate the effective pairwise potential $V_{eff}(r_i)$ from the pair correlation function the Monte Carlo procedure (MC) was performed [73]. It consists in the generation of simulated pair correlation functions $g^{MC}(r_i)$ and their iterative fitting to the experimentally obtained one $g^{exp}(r_i)$ by variation of the values of the effective pairwise potential $V_{eff}(r_i)$ [46, 47].

The MC procedure was implemented on a square lattice which represents the $c(2 \times 2)$ adlayer of a size of 1000×1000 adsorbate sites with applied Born-Karman periodic

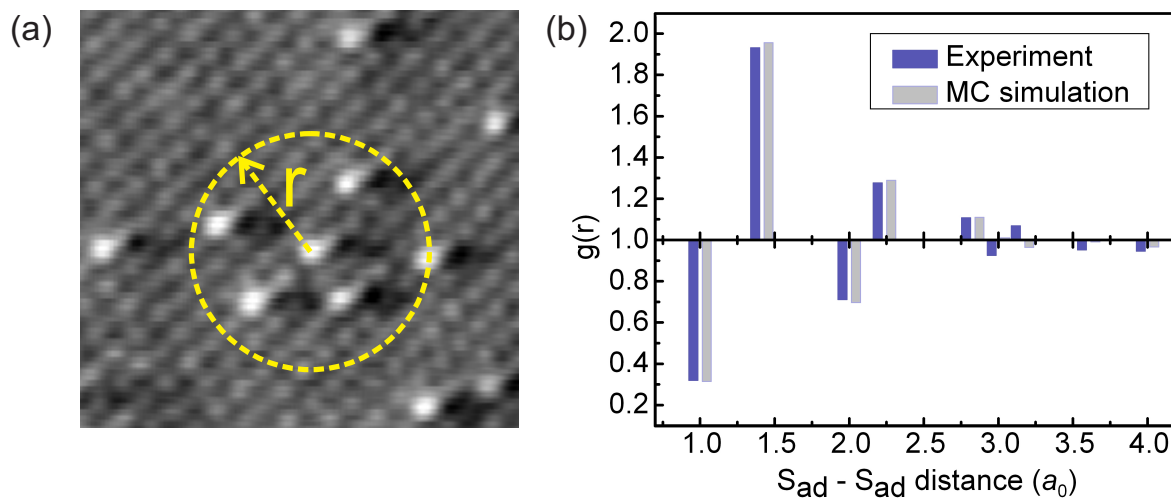


Figure 3.7.: a) Example of the spatial distribution of sulphur adsorbates around the selected one. b) The experimental (dark blue bars) and simulated (light grey bars) $S_{ad} - S_{ad}$ pair correlation functions obtained at $-0.47 V_{SCE}$. The experimental data were collected from 4934 STM images.

boundary conditions. Initially, the sulfur adsorbates were randomly distributed on the matrix according to the value of the surface coverage obtained from the experimental data (in the range of 0.005–0.02 ML). The equilibrium condition, under which the total energy of the system approaches its minimal value and afterwards only fluctuates around it, was reached after performing 100 MC steps. During one MC step, each individual adsorbate had the possibility to change its location to an arbitrary chosen free adsorption site on the lattice.

In our simple scheme we consider only the effective interactions between the sulfur adsorbates which are specified by the values of the effective pair interaction potentials $V_{eff}(r_i)$ for 5 different distances between them $r_k = 1a_0, \sqrt{2}a_0, 2a_0, \sqrt{5}a_0, 2\sqrt{2}a_0$, for larger separations its values are assumed to be equal to zero. The lattice gas Hamiltonian, or the total energy of the system, for the simulated adsorbate distribution was calculated as the sum of the effective pair interactions:

$$H = H_0 + \frac{1}{2} \sum_{A,B} V_{eff}(r_{AB}) s_A s_B, \quad (3.17)$$

where H_0 is the Hamiltonian of the system without adsorbate interactions, s_A and s_B represent the occupation of the adsorption sites A and B , respectively, and are assigned a value of 1 if the given site is occupied by the sulphur adsorbate or 0 in the inverse case. r_i

is the distance between the sites A and B .

For a single attempt of the individual adsorbate to occupy the new location, the change of the total energy of the system ΔH , corresponding to the changes in adsorbate configurations if this attempt would be realized, was calculated from eq. 3.17. The probability of the transition to the new configuration p was determined according to the Metropolis algorithm [74]:

$$p = \begin{cases} 1 & \text{if } \Delta H \leq 0 \\ e^{-\frac{\Delta H}{kT}} & \text{if } \Delta H > 0. \end{cases} \quad (3.18)$$

Once the system reaches the equilibrium condition, the adsorbate pair correlations were calculated from the simulated distributions. Due to the finite size of the matrix and low surface coverage, the total number of adsorbate observations in one run of the MC procedure can be even smaller than for the case of experimental data. To get a statistically sufficient number of observations (≥ 100.000), the whole procedure was repeated for the given set of $V_{eff}(r_i)$ required number of times depending on the simulated adsorbate surface coverage (at least 10 times for the coverage of 0.01 ML) and the obtained results were accumulated and then the MC simulated pair correlation function $g^{MC}(r_i)$ was calculated.

For each STM measured distribution, the iterative procedure based on the Neadler-Mead simplex downhill algorithm [75] was used for the fitting of the simulated distributions to the experimentally found ones by variation of the values of effective pair interactions $V_{eff}(r_i)$ at the 5 mentioned separations between them (Fig. 3.7b, light gray bars). The best set of energy parameters $V_{eff}(r_i)$ corresponds to the maximum agreement between the measured and simulated distribution, i.e. the minimal value of the parameter:

$$f = \sum_i (g^{MC}(r_i) - g^{exp}(r_i))^2. \quad (3.19)$$

The fitted values of the effective pair potential for the case of experimental data recorded at $-0.47 \text{ V}_{\text{SCE}}$ are represented in the plot in Fig. 3.8 by black circles. The obtained potential $V_{eff}(r_i)$ shows good agreement, in the distance dependence as well as in the absolute values, with the pairwise potential $V_{pair}(r_i)$ (Fig. 3.5) determined via the dynamic method of the analysis of the same experimental data. Here we also observe repulsion on nearest neighbor sites and attraction on next-nearest neighbor sites with similar values on the order of a few 10 meV.

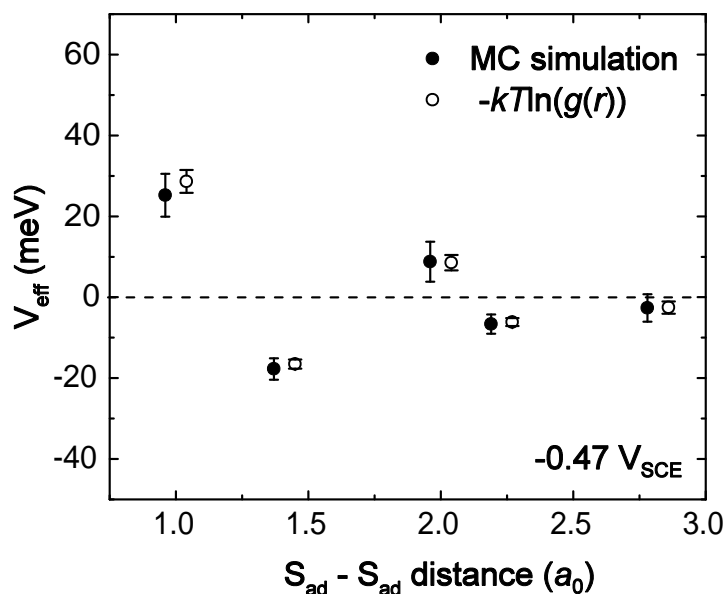


Figure 3.8.: Effective $S_{ad} - S_{ad}$ potential $V_{eff}(r_i)$ obtained from the analysis of S_{ad} distributions at $-0.47 V_{SCE}$. Values of the best fit MC parameters (black circles) are almost equivalent to the simple estimate from the pair correlation function via eq. 3.20 (white circles).

The estimation of the confidence intervals for the $V_{eff}(r_i)$ parameters was performed in the following way. First, by using the obtained values of $V_{eff}(r_i)$ (shown in Fig. 3.8) as input parameters, 50 different sets of adsorbate distributions corresponding to this interatomic potential were generated via Metropolis MC simulations. The statistical counting for the obtained distributions was chosen to be exactly the same as for the experimentally obtained one. The simulated distributions were fitted separately, in a similar way as for the case of the experimental data, using the IMC procedure described above. This results in the production of 50 sets of the effective interatomic potentials $V_{eff}^*(r_i)$, which values can be treated as measured in the computer experiments. The estimation of confidence intervals is based on the assumption that the shape of the distribution of these values around the values of $V_{eff}(r_i)$ previously fitted from the experimental data, would be nearly the same as around the 'real' value of measured parameter [76]. The confidence limits for each parameter are taken then as twice the standard deviation of this parameter in the performed simulations. The illustration of this approach is given in Fig. 3.9, where the correlation between the values of $V_{eff}(r_i)$ at nearest neighbor and next-nearest neighbor sites obtained in 50 MC experiments are shown. The distribution of two parameters shows the expected elliptical shape.

It is necessary to remember that the interatomic potentials obtained by both methods

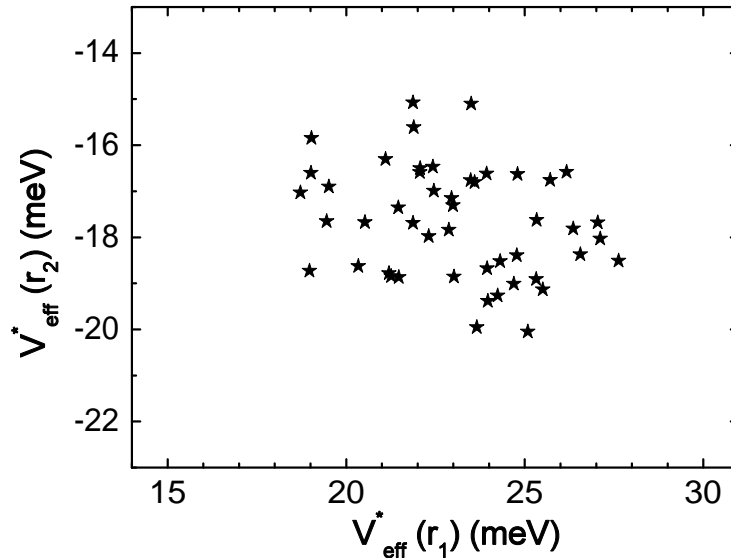


Figure 3.9.: Distribution of the fitted parameters $V_{eff}(r_1)$ and $V_{eff}(r_2)$ obtained in the 50 MC simulations.

in general are not identical and reflect the different conditions under which the adsorbate interactions were studied. The pairwise potential $V_{pair}(r_i)$ (Fig. 3.5) describes the interaction between two isolated adsorbates, while the effective potential $V_{eff}(r_i)$ (Fig. 3.8) characterizes the interaction within an ensemble of adsorbates [41], where trimer, quadrimer etc. configurations make additional contribution to the adsorbate interactions [45].

In order to estimate how correctly the obtained values of $V_{eff}(r_i)$ represent the real pairwise interactions, one needs to consider the entropic effects. Those become apparent when interactions at certain adsorption sites have an influence on the pair correlation function measured in the close neighborhood of these sites and, consequently, on the derived values of $V_{eff}(r_i)$. In our case, the repulsion at the distance $1a_0$ may lead to an entropic attraction at neighboring locations $\sqrt{2}a_0$ and $2a_0$. Or else, the attraction at the distance $\sqrt{2}a_0$ may cause the entropic attraction also at distance $2\sqrt{2}a_0$. However, due to the low surface coverage of the adsorbates, these effects don't seem to be significant, and as a result, we obtain comparably similar values of $V_{pair}(r_i)$ and $V_{eff}(r_i)$.

As soon as the surface coverage approaches zero, the contribution of entropic forces vanishes. In the ideal case, when only a pair of adsorbates is considered, the pair interaction potential $V_{pair}(r_i)$ can be obtained directly from the pair correlation function $g(r_i)$ as was showed by Tsong et al. [32]:

$$V_{pair}(r_i) = -kT \ln(g(r_i)). \quad (3.20)$$

The results of this simple estimation are presented in Fig. 3.8 by white circles. They are in very good agreement with the best fit MC parameters.

The necessary conditions for the application of both methods - dynamic and equilibrium - are different. The dynamic analysis requires the determination of configurations of isolated dimers in consecutive frames and can be successfully performed if the jump rates of the adsorbates are comparable to the recording rate (10–20 Hz). If the mobility of the particles is higher, the identification of certain isolated dimers after the frame-to-frame time interval becomes more difficult. At the same time, higher mobility of adsorbates reduces the correlations in the distributions of the adsorbates at the measured time intervals, resulting in the production of larger number of statistically independent observations, and consequently increases the reliability of the results obtained by the equilibrium method.

4. Results of the quantitative study of the S_{ad} - S_{ad} interactions

4.1. Synopsis

Recently, a study of the S_{ad} tracer diffusion on the Cu(100) in the aqueous solution of 0.01 M HCl was performed by the direct in situ high-speed STM technique [1, 61, 70]. It reveals that the diffusion of the adsorbates can be considered as a thermally activated hopping between neighboring sites of $c(2 \times 2)$ adlayer and can be described in the terms of the random walk model. The mobility of S_{ad} was found to be dependent on the electrode potential, with the diffusion activation barrier linearly increasing towards the direction of the positive potentials with a slope of 0.5 eV/V. Such behavior can be explained by the interaction of the adsorbates dipole moment with the electric field of the double layer.

In the following study, the S_{ad} - S_{ad} interactions in the given electrochemical system were the object of our further analysis. Here we present the first results on adsorbate-adsorbate interactions at the metal-electrolyte interface obtained by direct high-resolution microscopy. Altogether, we have analyzed seven data sets from different STM experiments recorded formerly by T. Tansel at various electrode potentials in the range -0.52 to -0.32 V_{SCE} . The original data were processed with the image recognition software (see chapter 2) and analyzed by both quantitative methods described in chapter 3. As the result, the pairwise $V_{pair}(r_i)$ and the effective $V_{eff}(r_i)$ interatomic potentials were extracted, which are shown in Fig. 3 in the following PRL paper [80]. Here two columns a and b represent $V_{pair}(r_i)$ and $V_{eff}(r_i)$ for each electrode potential, correspondingly. The absence of the data for $V_{pair}(r_i)$ at the potential -0.52 V_{SCE} is related to the complexity to follow the dimer motion under this condition since the mobility of adsorbates become very high as compared to the recording rate.

All the data show similar trends: repulsion at nearest neighbor sites $r = a_0$ and attraction at next-nearest sites $r = \sqrt{2}a_0$. At larger separation of $r = 2a_0$ we observe a weaker repulsion which is pronounced to a higher extent at the positive potentials between -0.40 and -0.32 V_{SCE} . The verity of this phenomena will be discussed below.

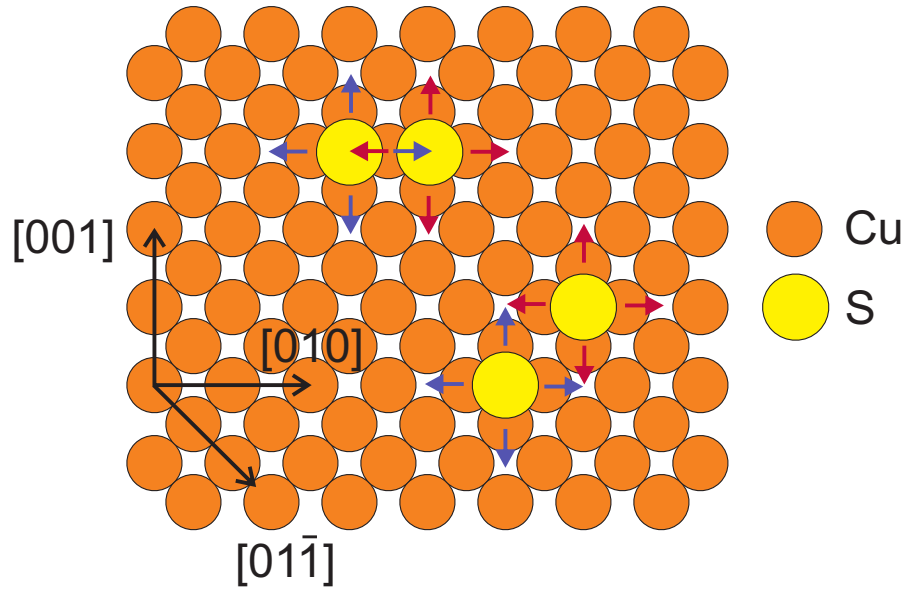


Figure 4.1.: The relaxation of the Cu atoms forming the fourfold hollow site induced by sulphur adsorption. Repulsion of S_{ad} at the nearest neighbor position can be account for by the opposite strain in the Cu(100) top layer along $[010]$ direction, while for the next-nearest neighbor configuration it has a common component in the $[01\bar{1}]$ direction.

The oscillatory distance behaviour of the interaction energies can be also considered as direction dependent with repulsion along the $[001]$ and an attraction along the $[011]$ lattice directions. This suggests that the major contribution to the interaction energies is made by the indirect interactions caused by elastic Cu lattice relaxation or electronic polarization of the metal substrate as compared to the direct interactions such as repulsive dipole-dipole interactions or van-der-Waals interactions. The electrostatic interactions are significant only at short distances and can be screened by solvating water molecules in the outer part of the double layer. Also the van-der-Waals diameter for S was found to be not larger than the regular $\sqrt{2}$ distance of copper [77].

It is known from the previous studies [78,79], that the specific adsorption of S on Cu(100) is characterized by a strong attraction of S_{ad} to the copper substrate. As was determined in [79], the specific adsorption of S_{ad} is accompanied by a radial outward displacement of the Cu atoms which form the fourfold hollow site (Fig. 4.1), thus inducing lateral strain. Therefore, the lattice strains induced by S_{ad} located at nearest neighbor sites oppose each other, causing a repulsion along the $[010]$ direction. However, in the case of the next-nearest neighbor configuration, S_{ad} have a common component of lattice displacement vector ori-

ented in the $[01\bar{1}]$ direction. Thus, they may interact less repulsively or even assist each other.

Similar pairwise interactions were obtained by a direct quantitative analysis of a comparable system in UHV. A study of N adsorbate distributions on Fe(100) revealed nearest neighbor repulsion (130 meV), next-nearest neighbor attraction (-18 meV) and third neighbor repulsion (15 meV) [45].

4.2. Publication *Physical Review Letters* 104, 106101(2010).

Copyright (2010) The American Physical Society [80]. The article is available via the internet at <http://prl.aps.org/abstract/PRL/v104/i10/e106101>.

Quantitative Measurements of Adsorbate-Adsorbate Interactions at Solid-Liquid Interfaces

A. Taranovskyy, T. Tansel, and O. M. Magnussen

Institut für Experimentelle und Angewandte Physik, Universität Kiel, Olshausenstr. 40, 24098 Kiel, Germany

(Received 18 December 2009; published 11 March 2010)

The interactions between adsorbates at a solid-liquid interface were studied by video-rate STM for the case of sulfur on Cu(100) electrode surfaces in HCl solution. Quantitative data were obtained by analyzing the S_{ad} dimer dynamics within the surrounding $c(2 \times 2)$ -Cl adlattice as well as the adsorbate configurations. The interactions are repulsive for S_{ad} separated by one or two lattice spacings and attractive at a separation of $\sqrt{2}$ with energies comparable to adsorbates at the solid-vacuum interface. The S_{ad} diffusion barriers are significantly reduced in the vicinity of a neighboring adsorbate.

DOI: 10.1103/PhysRevLett.104.106101

PACS numbers: 68.43.De, 68.08.-p, 68.37.Ef

Interatomic interactions between species adsorbed on solid surfaces in contact with a liquid solution are of key importance in numerous processes occurring at these interfaces, e.g., catalytic reactions, crystal growth, surface phase transitions, or self-assembly. Up to now, very little was known about such adsorbate-adsorbate interactions, mostly due to lack of quantitative experimental data. Even for adsorbates on clean surfaces in ultrahigh vacuum (UHV), quantitative microscopic studies of their mutual interactions are scarce and have been performed only for a few selected systems [1–5]. No such data at all currently exist for adsorbates at solid-liquid interfaces, where the effective adsorbate-adsorbate interactions may be modified by the presence of other coadsorbed species of the liquid phase, such as solvent molecules and ions, as well as by surface charges and the resulting strong electric field at the interface. Although clear qualitative evidence for a pronounced influence of the liquid environment on the adsorbate dynamics was found experimentally as well as in theoretical studies [6,7], the nature of the interactions in these complex systems is therefore largely not understood.

Experimental studies of the atomic-scale dynamics at solid-liquid interfaces are challenging for several reasons: First, these buried interfaces are not accessible to many of the surface-sensitive techniques employed for such studies under UHV conditions, e.g., field ion microscopy. Second, the temperature range is severely restricted, prohibiting studies at cryogenic temperatures, where the dynamic is slow. In addition, adsorbate-adsorbate interaction energies are small, typically only of the order of a few to a few ten meV, and hence large data sets have to be acquired to obtain statistically significant numbers that allow determining these energies with sufficient precision. In a recent study of adsorbed sulfur on Cu(100) electrode surfaces immersed in HCl solution, we demonstrated that the motion of adsorbates could be followed *in situ* by scanning tunneling microscopy with high temporal resolution (video-STM) [8]. While that study concentrated on the tracer diffusion of isolated S_{ad} adsorbates, we here present a quantitative statistical analysis of the S_{ad} - S_{ad} interactions

in this prototypical, but very well defined adsorbate system.

Details on the employed home-build *in situ* video-STM system and on the experimental procedures are given in the preceding publications [8–10]. The measurements were performed at room temperature under electrochemical control in 0.01 M HCl solution containing 10–30 μ M Na_2S , resulting in S_{ad} coverages between 0.005 and 0.02 ML. In the studied potential regime (-0.32 to -0.52 V vs the saturated calomel reference electrode), the Cu(100) surface is covered by an ordered $c(2 \times 2)$ chloride adlayer with a lattice spacing $a_0 = 3.61$ Å. At low surface coverage, each sulfur adsorbate substitutes one the more weakly bound chloride adsorbates in the $c(2 \times 2)$ superstructure. The S_{ad} species is clearly visible in the STM images due to a larger apparent height as compared to the Cl_{ad} adlattice [Fig. 1(a)]. As can be directly observed in the recorded videos (see supplementary information in Ref. [8] for examples), the presence of non-negligible S_{ad} - S_{ad} interactions manifests in the qualitative behavior of the S_{ad} ensembles. Specifically, the S_{ad} mobility is enhanced in the vicinity of other S_{ad} , as illustrated by the rapid positional fluctuations of the S_{ad} dimer in Fig. 1(b). Furthermore, the S_{ad} are not randomly distributed on the surface but certain interatomic distances are favorable [see Fig. 1(a)].

For the quantitative analysis, the STM video data, consisting of several hundred to a few thousand images recorded with a frequency of 10 to 20 fps, was first transformed into a digital map by a dedicated image recognition software developed by our group. The resulting series of occupation maps, which describes the S_{ad} locations on the $c(2 \times 2)$ lattice at regular time intervals, was the basis for the statistical analysis. Sulfur-sulfur interaction energies were determined by two different methods: (i) by studying the dynamics of isolated S_{ad} dimers and (ii) by configuration analysis of the (static) S_{ad} distributions. In the first approach, the motion of dimers, consisting of two sulfur adsorbates isolated from all other sulfur adsorbates by a distance of at least $3a_0$ [indicated by the circle in Fig. 1(b)] was determined. Our previous studies of

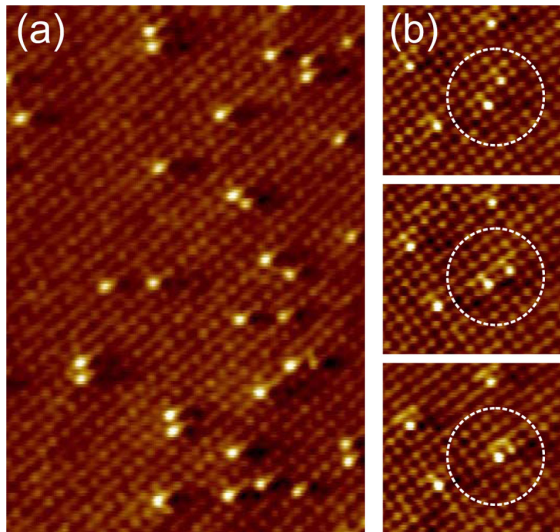


FIG. 1 (color online). *In situ* video-STM images of S_{ad} on Cu(100) in 0.01 M HCl. (a) Example showing a characteristic S_{ad} distribution ($-0.38 V_{SCE}$, $95 \times 140 \text{ \AA}^2$). (b) Three successive images recorded at 15 images/s ($-0.47 V_{SCE}$, $50 \times 44 \text{ \AA}^2$), illustrating the enhanced dynamics of the S_{ad} dimers (marked by circle).

S_{ad} tracer diffusion showed that at these distances the interatomic interactions were negligible [8]. Hence, this analysis provides true pairwise interaction potentials $V_{pair}(r)$. The changes in the configurations of these dimers were used to determine the two-particle jump distribution functions [Fig. 2(a)], which correspond to the probability that for a given initial dimer configuration, a new dimer configuration is found in the following frame, i.e., after a time interval Δt . For each experimental data set, 5 dimer configuration with initial S_{ad} - S_{ad} distances r_i of a_0 , $\sqrt{2}a_0$, $2a_0$, $\sqrt{5}a_0$, $2\sqrt{2}a_0$ were studied, consisting of a few hundreds up to thousand observations each.

To describe theoretically the motion of an adsorbate in the vicinity of a second S_{ad} , we consider modified adsorption energies E_i at S_{ad} - S_{ad} distances (index i being numbered according to the distance between the S_{ad}) as well as modified values for the saddle point energies E_{ij}^S which the adsorbates have to overcome for a jump from the site denoted i to a neighboring site j [see scheme in Fig. 2(b)]. This set of parameters describes the spatial modulation of the energy landscape for an S_{ad} adsorbate by a neighboring S_{ad} . The resulting S_{ad} diffusion barriers for a jump from site i to j are then given by $E_{ij}^D = E_{ij}^S - E_i$, the corresponding hopping rates by $\gamma_{ij} = \gamma_0 \cdot \exp(-E_{ij}^D/kT)$, where $\gamma_0 = 2.35 \times 10^{12} \text{ s}^{-1}$ is the attempt frequency [8]. For values $i \geq 5$, the E_i values were chosen to be identical to the adsorption energy of an isolated S_{ad} . A model where only the saddle point energies E_{12}^S , E_{13}^S , and E_{∞}^D were free parameters (with E_{∞}^D being the tracer diffusion bar-

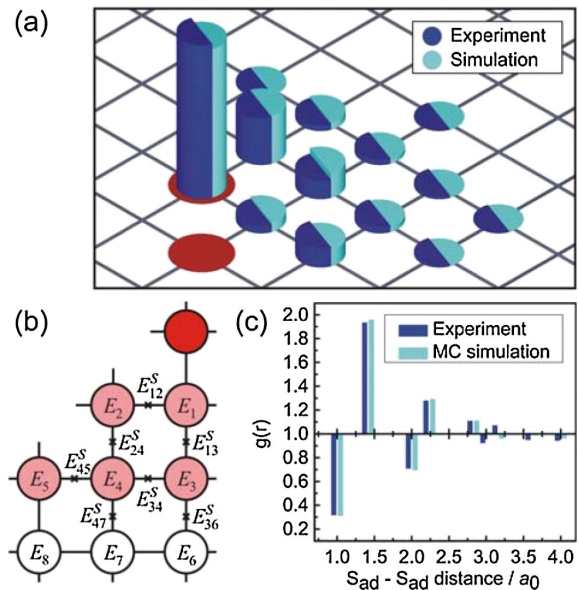


FIG. 2 (color online). (a) Example of experimental and simulated two-particle jump distribution functions (shown for a S_{ad} - S_{ad} distance of $\sqrt{2}a_0$ as starting configuration; experimental data correspond to 310 events). (b) Schematic model of the modified energy landscape in the vicinity of another coadsorbate. (c) Example of experimental and simulated S_{ad} pair correlation functions. The experimental data is based on 10 Hz videos consisting of (a) 4934 and (c) 4483 frames obtained at $-0.47 V_{SCE}$.

rier) whereas all other E_{ij}^S were calculated via $E_{ij}^S = 1/2(E_i + E_j) + E_{\infty}^D$ gave almost identical results. For a given parameter set, the two-particle distribution functions for the 5 experimentally studied dimer configurations were calculated numerically via a master equation approach similar to that used in Ref. [3], assuming that S_{ad} jumps only occur between neighboring lattice sites [example shown in Fig. 2(a)]. Using a grid search algorithm, the set of energy parameters was fitted to the experimental functions, resulting in the pairwise interaction potential $V_{pair}(r_i) = E_i - E_5$ (error bars were calculated from the local curvature of χ^2 at the minimum).

As a second, alternative approach, the effective pair interaction potential $V_{eff}(r)$ was determined by comparing the experimental spatial distribution of the adsorbates with equilibrium configurations generated via Monte Carlo simulations. For this, first the radial pair correlation function $g(r)$ was calculated from the spatial S_{ad} distributions in the frames of each video (typically based on the positions of 3000 to 50 000 individual adsorbates). Because of the dependence of $g(r)$ on the S_{ad} coverage, frames with clearly deviating coverage were excluded from the analysis. A typical experimental pair correlation function of S_{ad} on Cu(100), obtained at $-0.47 V_{SCE}$, is presented in Fig. 2(c). Its shape reflects the qualitatively observed ten-

dencies in the S_{ad} surface distribution: the next-nearest neighbor sites are occupied with higher probability than for the case of random distribution, while the nearest neighbor sites are unfavorable. These correlations decrease fast with distance and can be neglected already at separations $\geq 3a_0$, in agreement with the range of interactions considered in the statistical analysis. Next, assuming pairwise S_{ad} - S_{ad} interactions, specified by the values of $V_{eff}(r)$ for $r = a_0, \sqrt{2}a_0, 2a_0, \sqrt{5}a_0, 2\sqrt{2}a_0$, theoretical equilibrium pair correlation functions were calculated via the Metropolis method [11], which were fitted to the experimental data via a simplex downhill algorithm [12] (the confidence limits of these parameters were estimated as twice the standard deviation of the corresponding parameters calculated from 50 Monte Carlo distributions). This method has disadvantages as well as advantages as compared to the study of dimer dynamics described above: On the one hand, $V_{eff}(r)$ may deviate from the true $V_{pair}(r)$ in the case of nonpairwise interactions (especially at higher S_{ad} coverage) and saddle point energies cannot be obtained; on the other hand, this approach uses the data on all S_{ad} adsorbates rather than only that on isolated dimers, i.e., can provide better statistics, and can be employed also at high S_{ad} mobility, where the S_{ad} diffusion length between successive frames exceeds the average distance between the adsorbates.

The S_{ad} interaction potentials obtained by these two methods for different electrode potentials are shown in Fig. 3. Obviously, the distance dependence as well as the absolute energy values are in good agreement. Specifically, an oscillatory dependence of the interaction energy on the S_{ad} - S_{ad} spacing is found at all potentials with repulsive interactions at separations $r = a_0$ (nearest neighbors), attractive interactions at $r = \sqrt{2}a_0$ (next-nearest neighbors), and more weakly repulsive interactions at $r = 2a_0$. This type of interaction is supported by the observation of a $p(2 \times 2)$ sulfur structure formed at higher S_{ad} coverages on clean Cu(100) surfaces under UHV conditions [13] as well as in electrochemical environment [14]. The S_{ad} - S_{ad} interaction energies are of the order of a few 10 meV.

Interaction energies of this magnitude and a characteristic spatial extension of the interaction over several lattice distances were also found in the few comparable STM studies of adsorbate-adsorbate interactions, performed for similar adsorbates at metal surfaces under UHV conditions [3–5,15]. In particular, studies of N on Fe(100), i.e., a square lattice as in our study, also found an oscillatory dependence on the distance [4,15]. The qualitatively similar behavior in both environments suggests that for these strongly bound adsorbates, the interactions are not decisively affected by presence of the electrolyte. To discuss this, we consider the different contributions to these interactions, which are direct interactions (e.g., dipole-dipole) and indirect interactions, mediated by elastic lattice relaxation or electronic polarization of the metal substrate. The

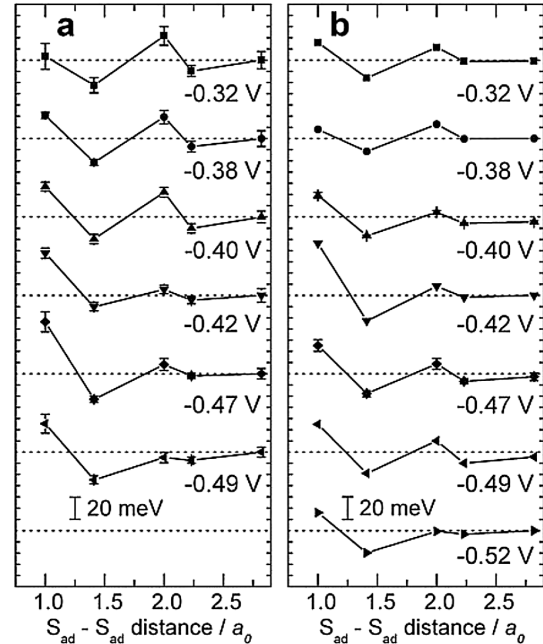


FIG. 3. Distance-dependent S_{ad} - S_{ad} interaction energies obtained from analysis of (a) the S_{ad} dimer dynamics (V_{pair}) and (b) the S_{ad} distributions (V_{eff}) as a function of the electrode potential.

former are even at the metal-vacuum interface only significant at very short distances and should be significantly screened by solvating water molecules and counterions in the outer part of the electrochemical double layer. The dominant contribution at distances of a few Cu lattice spacings should come from indirect interactions. In principle, also those may be noticeably influenced by the presence of the solution, in particular, of the coadsorbed $c(2 \times 2)$ chloride adlayer, which should affect the S_{ad} induced lattice relaxation and the metal electronic structure. However, according to our data, these effects seem not to result in a fundamentally different adsorption behavior, although a precise estimation is difficult due to the lack of quantitative data for S_{ad} on Cu(100) in UHV. This is in accordance with recent DFT calculations for S_{ad} diffusion on a $c(2 \times 2)$ -Cl covered surface, which indicate a rather small influence of the Cl coadsorbate even for S_{ad} embedded in a perfect, defect free $c(2 \times 2)$ -Cl lattice [16].

The oscillatory dependency of the S_{ad} - S_{ad} interaction on distance can be also interpreted as a directional dependence of the interaction energies, with a repulsive interaction along the [001] and an attractive interaction along the [011] directions, respectively. The latter can be rationalized by a dominant contribution of indirect elastic interactions via lattice distortions, as proposed for N/Fe(100) by Pedersen *et al.* [15]. Upon sulfur adsorption, the Cu atoms that form the fourfold hollow adsorption site are displaced radially outward (i.e., move in [001] direction)

[13], which explains the repulsive interaction between neighboring S_{ad} along these axes. In contrast, the S_{ad} in next-nearest neighbor positions ($r = \sqrt{2}a_0$), i.e., oriented along [011], have a common component of the displacement vector in $[0\bar{1}\bar{1}]$ direction and hence interact less repulsively or even may assist each other.

Of particular interest in electrochemical systems is the effect of the electrode potential on the interaction energy. Despite some scatter in the experimental data and the limited potential range, a common trend towards more long-range interactions at more positive potentials can be recognized. Specifically, the interaction energy at $r = a_0$ seems to decrease whereas that at $r = 2a_0$ seems to increase with increasing potential. The origin of this potential effect is currently not clear, since all contributions to $V_{pair}(r)$ —indirect elastic and electronic interactions as well as direct interactions between the adsorbates—may be affected by changes in the potential-dependent surface charge density and the corresponding electric field at the interface induced. However, the observed behavior qualitatively agrees with the results by Spaenig *et al.* for the sulfur adlayer phase behavior at low sulfide concentrations [14]. In that study, the $p(2 \times 2)$ sulfide adlayer was found to transform at more positive potentials to a more densely packed $c(6 \times 2)$ structure, which features S_{ad} interatomic distances of a_0 and $\sqrt{2}a_0$, whereas some of the of S_{ad} - S_{ad} spacings at $2a_0$ are systematically omitted. Our data on the (pairwise) interatomic interactions of isolated S_{ad} suggest that this transition may be directly driven by potential-induced changes in the distance-dependent S_{ad} - S_{ad} interaction energy rather than solely by an increase in the S_{ad} coverage and resulting packing constrains.

In addition, the analysis of the dimer dynamics provides the saddle point energies and diffusion barriers in the vicinity of neighboring S_{ad} . The latter are noticeably lowered with respect to the tracer diffusion barrier of isolated particles E^D_∞ , manifesting in significantly higher jump rates for S_{ad} in dimers [see Fig. 1(b)]. Comparing the average diffusion barriers between the adsorption sites $E^{av}_{ij} = E^S_{ij} - (E_i + E_j)/2$ to E^D_∞ , we find ≈ 30 meV lower values for E^{av}_{12} , i.e., jumps between neighbor and next-nearest neighbor sites, and ≈ 70 meV lower energies for E^{av}_{13} at all potentials. Consequently, the modified barriers near other adsorbates have the same dependence on electrode potential as the diffusion barriers of isolated sulfur adsorbates [8]. Similar modifications of the adsorbate dynamics by neighboring adsorbates were previously found for strongly bound species on metal surfaces under UHV conditions [3,15] as well as in *ab initio* theoretical studies [17].

In summary, we have demonstrated that *in situ* video-STM studies allow a quantitative determination of adsorbate-adsorbate interactions and distance-dependent diffusion barriers at solid-liquid interfaces, specifically

for adsorbates on metal surfaces in aqueous electrolytes. Our measurements provide first data on the complete energy landscape for an adsorbate at this type of interface. The measured interaction potentials were shown to be in good agreement with the (potential-dependent) adsorbate phase behavior at higher coverages and comparable to those of adsorbates on clean surfaces under UHV conditions. Furthermore, the S_{ad} mobility was strongly enhanced by neighboring adsorbates. As pointed out previously [17], adsorbate-adsorbate interactions profoundly influence the mesoscopic system properties, such as the nucleation and growth behavior. Detailed understanding of such interactions, as can be obtained by more systematic studies of this type, will therefore provide fundamental insight that is relevant for a large range of processes at these complex interfaces.

We gratefully acknowledge financial support by the Deutsche Forschungsgemeinschaft (MA1618/5, MA1618/15) and by the Deutsche Akademische Austauschdienst for financial support for A. T.

-
- [1] T. T. Tsong, Rep. Prog. Phys. **51**, 759 (1988).
 - [2] G. Ehrlich and F. Watanabe, Langmuir **7**, 2555 (1991).
 - [3] S. Renisch, R. Schuster, J. Winterlin, and G. Ertl, Phys. Rev. Lett. **82**, 3839 (1999).
 - [4] L. Österlund, M. Ø. Pedersen, I. Stensgaard, E. Laegsgaard, and F. Besenbacher, Phys. Rev. Lett. **83**, 4812 (1999).
 - [5] T. Mitsui, M. K. Rose, E. Fomin, D. F. Ogletree, and M. Salmeron, Phys. Rev. Lett. **94**, 036101 (2005).
 - [6] M. T. M. Koper, J. Electroanal. Chem. **450**, 189 (1998).
 - [7] P. A. Rikvold, A. Wieckowski, and R. A. Ramos, Mater. Res. Soc. Symp. Proc. **451**, 69 (1997).
 - [8] T. Tansel and O. M. Magnussen, Phys. Rev. Lett. **96**, 026101 (2006).
 - [9] L. Zitzler, B. Gleich, O. M. Magnussen, and R. J. Behm, Proc. Electrochem. Soc. **99-28**, 29 (2000).
 - [10] O. M. Magnussen, L. Zitzler, B. Gleich, M. R. Vogt, and R. J. Behm, Electrochim. Acta **46**, 3725 (2001).
 - [11] N. Metropolis, A. W. Rosenbluth, M. N. Rosenbluth, and A. H. Teller, J. Chem. Phys. **21**, 1087 (1953).
 - [12] J. A. Nedler and R. Mead, Computer Journal (UK) **7**, 308 (1965).
 - [13] H. C. Zeng, R. A. McFarlane, and K. A. R. Mitchell, Phys. Rev. B **39**, 8000 (1989).
 - [14] A. Spaenig, P. Broekmann, and K. Wandelt, Z. Phys. Chem. (Frankfurt/Main) **217**, 459 (2003).
 - [15] M. Ø. Pedersen, L. Österlund, J. J. Mortensen, M. Mavrikakis, L. B. Hansen, I. Stensgaard, E. Laegsgaard, and J. K. Nørskov *et al.*, Phys. Rev. Lett. **84**, 4898 (2000).
 - [16] J. Stremme, diploma thesis, Kiel University, 2009.
 - [17] A. Bogicevic, S. Ovesson, P. Hyldgaard, B. I. Lundqvist, H. Brune, and D. R. Jennison, Phys. Rev. Lett. **85**, 1910 (2000).

4.3. Publication ChemPhysChem 11, 1438(2010).

Reprinted with permission from ChemPhysChem **11**, 1438(2010). Copyright (2010) Wiley-VCH Verlag GmbH & Co. KGaA, Weinheim [81]. The article is available via the internet at <http://onlinelibrary.wiley.com/doi/10.1002/cphc.200900939/full>.

DOI: 10.1002/cphc.200900939

In Situ Video-STM Studies of Adsorbate Dynamics at Electrochemical Interfaces

Tunay Tansel, Andriy Taranovskyy, and Olaf M. Magnussen*^[a]*Dedicated to Prof. Dr. R. Jürgen Behm on the occasion of his 60th birthday*

The dynamic behavior of individual adsorbates at electrochemical interfaces was studied directly by in situ high-speed scanning tunneling microscopy, using sulfur adsorbed on Cu(100) electrodes in 0.01 M HCl solution as an example. By dosing from diluted Na₂S solutions S_{ad} coverages of a few percent can be prepared, with the sulfur adsorbates occupying positions within the c(2×2) lattice of coadsorbed chloride. S_{ad} tracer diffusion occurs via hopping between neighboring c(2×2) lattice sites at considerably higher rates than those of sulfur on Cu(100) under UHV conditions, indicating a pronounced influence of the electrochemical environment on the adsorbate surface dynamics. The diffusion barrier linearly increases by 0.5 eV

per V with potential and is strongly affected by neighboring S_{ad} and surface defects. The S_{ad}–S_{ad} interactions extend over ≈ 7 Å. They are repulsive between nearest-neighbor and attractive between next-nearest-neighbor sites, respectively, and result in significantly reduced diffusion barriers. S_{ad} on the upper terrace side of steps are transiently trapped and exhibit lower diffusion rates, leading to the formation of small metastable p(2×2) domains. Attractive interactions between S_{ad} and domain boundaries in the c(2×2) adlayer result in boundary pinning as well as transient trapping and enhanced diffusion of S_{ad} along the boundary.

1. Introduction

The surface diffusion of adsorbates on metal surfaces and the mutual interactions between adsorbed species as well as between adsorbates and surface defects are essential elementary steps in almost any electrochemical reaction, ranging from galvanic deposition to electrocatalysis. To clarify in detail how the interface structure affects these processes is of key importance for developing an in-depth understanding of these electrode reactions and a focus of current experimental and theoretical studies. In contrast to surfaces under ultrahigh vacuum (UHV) conditions, where the surface diffusion and interaction of adsorbates have been studied at length by high-resolution microscopic techniques, such as field ion microscopy (FIM) and scanning tunneling microscopy (STM),^[1,2] detailed data on adsorbate dynamics at electrochemical interfaces are currently missing. This is largely caused by the high mobility of adsorbates at room temperature and the lack of suitable in situ methods for the direct investigation of atomic-scale surface dynamic phenomena in electrochemical environment. We have recently demonstrated that in a suitable chosen model system, adsorbed sulfide on Cu(100) in HCl solution, the dynamics of individual adsorbates can be directly followed by in situ video-STM and we employed this for quantitative studies of the potential-dependent diffusion of isolated S_{ad} (“tracer diffusion”).^[3] Herein, a more comprehensive overview of this adsorbate system is presented, focusing on the effect of neighboring S_{ad}, surface defects, and coadsorbates.

From the extensive previous studies performed under UHV conditions, a detailed picture of adsorbate dynamics on clean, single crystalline surfaces has emerged. Surface diffusion of isolated, simple atomic adsorbates can often be described as a

thermally activated hopping between the energetically preferred adsorption sites on the surface with an activation energy (“diffusion barrier”) given by the spatial modulation of the adsorption energy in the surface plane and a preexponential factor (“attempt frequency”), which is typically of the order of the adsorbate vibration frequencies. This process can be strongly affected by interactions with other adsorbates, an unalterable condition in electrochemical environment, and by interactions with structural defects on the substrate surface, such as steps. Adsorbate–adsorbate interactions include contributions from direct dipole–dipole interactions as well as substrate-mediated interactions and accordingly can exhibit a rather complex dependence on the distance between neighboring species and their arrangement on the substrate lattice. Consequently, the influence of these interactions on surface transport is also far more complex than simple site blocking. Even for adsorbates at the solid–vacuum interface only a few experimental studies of metallic^[4] and non-metallic^[5] adsorbate–adsorbate interactions by quantitative microscopic studies have been reported. How these diffusion barriers and interaction energies are modified by the electrochemical environment is currently unclear and cannot easily be predicted.

The in situ video-STM developed by our group^[6] provides the necessary temporal resolution for direct atomic-scale stud-

[a] Dr. T. Tansel, A. Taranovskyy, Prof. Dr. O. M. Magnussen
Institut für Experimentelle und Angewandte Physik
Universität Kiel
Olshausenstr. 40, 24098 Kiel (Germany)
Fax: (+49) 431 8804884
E-mail: magnussen@physik.uni-kiel.de

ies of dynamic processes on electrode surfaces and allows to record in a short time sufficiently large data sets for a quantitative statistical analysis. We have applied this technique in the past for studies of metal deposition and dissolution^[7–9] as well as of collective nanoscale transport phenomena during the formation of the potential-induced Au reconstruction.^[10–12] Recently, we made the first in situ measurements of adsorbate surface diffusion with this method.^[3] For such direct video-STM studies the hopping rates of the adsorbates between neighboring sites have to be of the same order of magnitude as the time resolution, that is, the image acquisition rate (typically 200 to 33 ms). In the available temperature window of aqueous electrochemical systems this requires rather high diffusion barriers of > 0.6 eV (assuming typical pre-exponential factors of $\approx 10^{12} \text{ s}^{-1}$). In addition, no strong attractive interactions between the adsorbates should exist, which would result in islands of a close-packed adsorbate phase and consequently a low density of isolated adsorbates, and diffusion into the substrate should be negligible. Both of these problems occur for many metallic adsorbates and make a strongly bound anionic species the system of choice. In these first direct experiments on electrochemical adsorbate dynamics, we therefore investigated sulfide on Cu(100), which for the reasons given above is well suited for such studies. In particular, a high diffusion barrier may be expected, since sulfide is a strongly bound species on noble metal surfaces and adsorbs at low coverages in the (energetically very deep) fourfold hollow sites of the metal substrate.^[13] Indeed, previous qualitative STM observations of low-coverage sulfur adsorbates on a vicinal Cu(100) surface reported a low mobility at room temperature.^[14]

The adsorption of sulfide on Cu(100) electrodes has up to now only been studied at higher coverages by Spaenig et al.^[15] In that study S_{ad} was found to be irreversibly adsorbed in the entire double layer potential regime down to the onset of hydrogen evolution. At the lowest sulfide concentrations and most negative potentials a $p(2 \times 2)$ structure with a high defect density was observed by in situ STM. After longer immersion times this low-coverage phase was irreversibly replaced by a more densely packed $c(6 \times 2)$ adlayer structure. Domain boundaries between the two different $c(6 \times 2)$ domains were found to exhibit rapid fluctuations, indicating a high surface mobility of the adsorbates. More detailed data on the low-coverage regime have not been published up to now.

Herein we present an overview on our video-STM observations of individual sulfur adsorbates on Cu(100) in 0.01 M HCl solution. We have focused on the potential range in which the Cu surface is covered by the well-known $c(2 \times 2)$ chloride adsorbate layer,^[16–18] where the adsorbate motion was sufficiently low to be observed directly. After describing our method of preparing Cu(100) electrodes with the required, low S_{ad} coverage and demonstrating that the dynamic behavior of these adsorbates is not significantly altered by the STM measurement, we describe the tracer diffusion of isolated S_{ad} in the undistorted $c(2 \times 2)$ adlayer and the influence of the $S_{\text{ad}}-S_{\text{ad}}$ interactions on the adsorbate dynamics. In these sections a short review of our previous quantitative results is also given to allow a more detailed discussion of the role of the electrochemical environ-

ment—in particular of coadsorbates—on these processes. Then, the interactions of S_{ad} with defects in the Cu substrate, that is, the Cu steps, and defects in the $c(2 \times 2)$ adlayer, which are present in form of translational domain boundaries, is described.

Experimental Section

A home-build video-STM for in situ measurements in the electrochemical environment was used in the experiments.^[6] The electrochemical cell was kept at a fixed temperature between 277 and 296 K by a Peltier element, controlled by a Lakeshore 331 temperature controller. Potentials were measured using a Cu wire, calibrated vs a saturated calomel electrode (SCE). The Cu(100) single-crystal samples (diameter 6 mm) were prepared by the procedure described in ref. [17], which involves electropolishing in orthophosphoric acid, rinsing with ultrapure water, and immersion into 0.01 M HCl solution, prepared from HCl (Merck, suprapure) and ultrapure water. Subsequently, small amounts of Na_2S solution, prepared from 38% sodium sulphide hydrate (Merck, p. a.), were added into the STM cell (total volume ≈ 1 mL), to achieve total S^{2-} concentrations of 12 to 55 $\mu\text{mol dm}^{-3}$ and by this dose the desired S_{ad} coverage on the surface. To ensure that the S_{ad} coverage on the Cu surface had reached a steady-state value the cell was inserted into the STM only after a waiting time of ≈ 1 hour. For the STM measurements W tips coated by Apiezon wax were used. Video-STM experiments were performed in “constant height” mode. Typically, 1 to 3 min. long video sequences were recorded at image acquisition rates of 10 to 30 images per second.

2. Results and Discussion

2.1. S_{ad} Structure and Dynamics on Cl-covered Cu(100)

In situ video-STM images show the characteristic $c(2 \times 2)$ lattice of the Cl-covered Cu(100) surface with a lattice spacing $a_0 = 3.6 \text{ \AA}$ as well as isolated maxima. As visible in Figure 1 a, these maxima are located precisely on positions of the $c(2 \times 2)$ lattice and move between different lattice sites on timescales between several ten milliseconds to several seconds, depending on potential, temperature, and local environment. This motion proceeds via jumps that occur much faster than the time between two successive scan lines (see for example, Figure 1 a, lower left corner), that is, within less than 0.25 ms, as expected

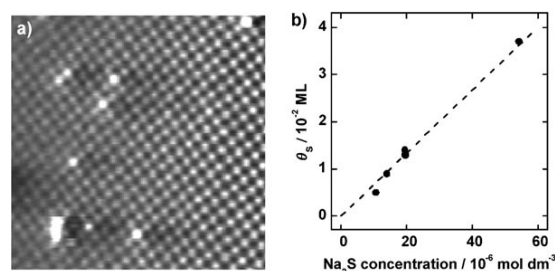


Figure 1. a) In situ video-STM image ($65 \times 65 \text{ \AA}^2$) of Cu(100) in 0.01 M HCl containing $12 \times 10^{-6} \text{ M Na}_2\text{S}$, showing the $c(2 \times 2)$ -Cl adlattice and individual S_{ad} adsorbates. b) S_{ad} coverage on Cu(100) in 0.01 M HCl as a function of Na_2S concentration in the solution.

for thermally activated hopping. We associated these mobile maxima with adsorbed sulfide embedded within the $c(2\times 2)$ Cl lattice.

To verify that the observed maxima indeed correspond to sulfide adsorbates, the sulfide concentration in the solution was systematically varied. The resulting coverage of the maxima changes approximately linearly with the sulfide concentration (Figure 1 b), supporting this assignment and demonstrating that controlled dosing of adsorbate coverages in the range of 1 to 2% is feasible. Obviously, the sulfide adsorbate replaces individual chloride adsorbates in the adlattice due to its stronger adsorption. Within the STM's resolution no deviations of the neighboring chloride adsorbates from the $c(2\times 2)$ lattice sites could be detected, suggesting that S_{ad} does not induce substantial lattice distortions. As can be seen in the upper left corner of Figure 1 a, sulfide adsorbates can occupy neighboring sites on the $c(2\times 2)$ lattice, that is, S_{ad} - S_{ad} distances down to 3.6 Å are possible. Occasionally, several sulfide adsorbates form larger metastable clusters in which their mobility is significantly enhanced and the individual S_{ad} cannot be resolved anymore (Figure 1 a, lower left corner). In the potential regime studied (-0.55 to -0.30 V_{SCE}) sulfide was apparently completely irreversibly adsorbed. A spontaneous disappearance of a S_{ad} from the surface, indicating sulfide desorption into the electrolyte, was never observed in the STM images.

A longer sequence of successive images from a video is shown in Figure 2, showing characteristic jumps of the S_{ad} between lattice sites. For example, S_{ad} jumps occur between the images recorded at 50 and 100 ms as well as between those at 300 to 350 ms, respectively (jump directions in each case indicated by arrows). As reported in our previous publication,^[3] the average jump frequency depends strongly on the potential. To

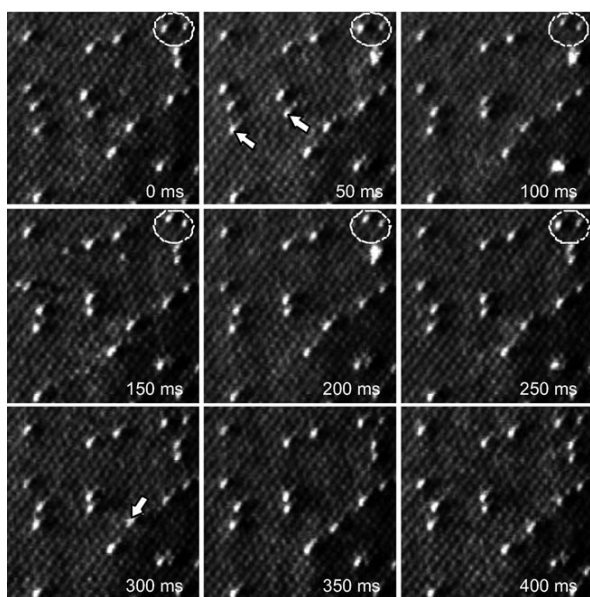


Figure 2. Subsequent images taken from an in situ video-STM sequence (85×85 Å²) of S_{ad} on Cu(100) in 0.01 M HCl at -0.32 V_{SCE} and 290 K, recorded at 20 Hz. Arrows and circled areas mark S_{ad} hopping events.

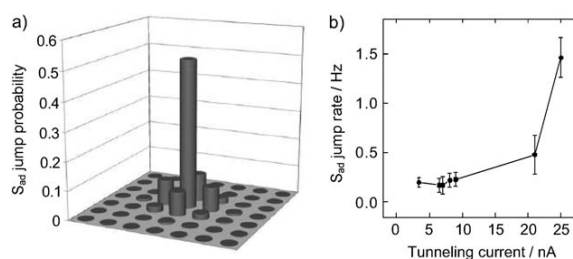


Figure 3. a) Probability for S_{ad} jumps to neighboring sites obtained from an in situ video-STM sequence on Cu(100) in 0.01 M HCl at -0.49 V_{SCE} and 294 K. b) Dependence of the average S_{ad} jump rate to nearest neighbor sites on the tunneling current, showing tip-enhanced diffusion for $I_t > 10$ nA.

quantify the mobility of the adsorbates, jump probability distributions were determined for S_{ad} adsorbates with a minimum spacing $> 4 a_0$ to the nearest neighboring S_{ad} . At these S_{ad} - S_{ad} spacings no influence on the mobility could be detected (see Section 3.2), that is, the measured hopping rates correspond to S_{ad} tracer diffusion. As an example, a jump distribution function of such isolated adsorbates at -0.49 V_{SCE} is shown in Figure 3 a. Here as well as under all other experimental conditions, the measured distribution functions are within the experimental errors in good agreement with a diffusion mechanism where the S_{ad} perform sequential jumps between neighboring sites of the $c(2\times 2)$ lattice, whereas direct jumps over larger distances do not seem to contribute significantly. Evidently, the jumps occur with similar rates to all four nearest-neighbor sites, as expected from the symmetry of the substrate. Hence, the scanning direction of the tip does not have a noticeable influence on the diffusion events. Experiments at different tunneling currents reveal that the hopping rates are significantly enhanced only at currents > 10 nA, whereas at lower currents the jump rates were identical within the experimental errors (Figure 3 b). Therefore, all dynamic studies of S_{ad} on Cu(100) were performed at tunneling currents ≤ 10 nA.

From a detailed quantitative analysis of the video data as a function of potential and temperature, the hopping rates and diffusion barriers can be obtained, respectively.^[3] As can be seen in Figure 4, all the data can be described by an effective S_{ad} diffusion barrier that increases linearly with potential with a slope of 0.5 eV V_{SCE}⁻¹. This strong potential dependence can be explained by electrostatic contributions to the adsorption energies, caused by the interaction of the adsorbate surface dipole moment with the electric field of the electrochemical double layer, as discussed at length in ref. [3]. Even at the most positive potentials, jumps of the S_{ad} to neighbor sites occur every few seconds at room temperature. In contrast, under UHV conditions a much lower mobility was reported for sulfur adsorbates on Cu(111), a vicinal Cu(100) surface, in a room-temperature STM study by Masson et al.^[14] Here S_{ad} adsorbed on Cu(100) terraces was found to be positional stable on time scales of minutes, suggesting that the diffusion barrier is strongly reduced by the electrochemical environment.

This behavior is rather surprising and contrary to expectation for several reasons. First, the most appropriate reference point for a quantitative comparison of surface diffusion in elec-

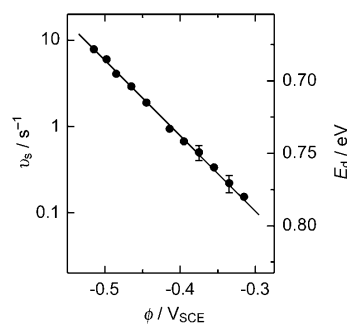


Figure 4. S_{ad} hopping rates and diffusion barriers E_d as a function of potential, obtained from a quantitative analysis of the in situ video-STM data.

trochemical environment with that under UHV conditions should be the potential of zero charge, which is several hundred millivolts more negative than the potential range studied herein (the pzc in weakly specifically adsorbing $KClO_4$ is reported as $-0.79 V_{SCE}$ ^[19]). Extrapolating the data in Figure 4 to this potential regime the surface mobility should be higher by several orders of magnitude. Second, in the study by Masson et al. S_{ad} was diffusing on a Cu surface free of coadsorbates whereas at the electrochemical interface the S_{ad} is embedded within a densely packed $c(2\times 2)$ -Cl adlayer. In a simple picture, these coadsorbates should increase the diffusion barrier by geometric blocking of neighboring sites, as often observed in studies under UHV conditions.^[20] Third, in hopping between neighboring adsorption sites on the bare Cu(100) surface, the adsorbate only has to traverse bridge sites of the Cu substrate. In contrast, jumps between $c(2\times 2)$ lattice sites require that the adsorbate crosses over an energetically unfavorable top site or performs two successive jumps across bridge sites. In the first case the diffusion barrier would be significantly higher, in the second one the preexponential factor should be reduced, likewise resulting in a reduced mobility.

For these reasons, the tracer diffusion of S_{ad} in electrochemical environment should be considerably slower than that of S_{ad} on bare Cu(100) surfaces in vacuum. The observed decrease in the barrier can only be rationalized by a pronounced influence of coadsorbates, specifically the coadsorbed chloride and water in the partial hydration shells of S_{ad} and Cl_{ad} , on the potential energy surface of the sulfur adsorbate. In view of the sparse data on adsorbate surface diffusion we discuss these electronic effects by considering the adsorption energies, with which the diffusion barriers increase in many cases. Although direct data on the modification of the S_{ad} adsorption energies by chloride and water coadsorbates do not exist, the effect of the $c(2\times 2)$ Cl_{ad} coadsorbate layer can qualitatively be estimated from the results of a recent DFT study, where a 0.54 eV lower binding energy was found per adsorbate for a $c(2\times 2)$ - S_{ad} layer on Cu(100) than for the more open $p(2\times 2)$ - S_{ad} adlayer.^[21] In view of the similar (anionic) nature of S_{ad} and Cl_{ad} this coadsorbate is also expected to decrease the S_{ad} binding energy.

Furthermore, the binding energies of the adsorbed anions may also be reduced by coadsorption of water on top of the $c(2\times 2)$ adlayer. In this context, recent electrochemical video-

STM observations of S_{ad} diffusion on a Cu(100) electrode covered by a $c(2\times 2)$ adlayer of bromide are interesting, where an even higher surface mobility was found.^[22] In view of the stronger specific adsorption of bromide as compared to chloride, this result seems to support the idea that the competitive adsorption of S_{ad} and the halide coadsorbate reduces the S_{ad} adsorption energies and diffusion barriers.

S_{ad} hopping to a neighbor site also requires the displacement of the Cl_{ad} on this site, which is a further factor to be considered in assessing the influence of coadsorbates on the S_{ad} diffusion mechanism. It is currently not clear whether the S_{ad} and the displaced Cl_{ad} move together in a concerted step or whether a vacancy is first formed in the $c(2\times 2)$ - Cl_{ad} lattice, followed by the S_{ad} jump. In the second case S_{ad} hopping could only take place if a neighboring site is unoccupied and hence should depend on the potential-dependent coverage of vacancies in the Cl adlayer. As shown in ref. [3], the latter could account for the observed potential dependence. However, this mechanism would result in a strongly lowered S_{ad} mobility as compared to a Cl_{ad} -free Cu surface, which does not seem to be the case. To account for the apparent absence of blocking effects, one may assume that the vacancies are not statistically distributed on the surface, but have a significantly higher probability to occupy neighboring sites around S_{ad} . Indeed observations of S_{ad} at domain boundaries suggest weak net attractive interactions between defects in the Cl adlayer and S_{ad} (see Section 3.4.), which would support this idea. However, such a vacancy-assisted diffusion mechanism is difficult to reconcile with the observed jump statistics. As recently shown for In atoms embedded within a Cu(100) surface layer, jump distributions for vacancy-assisted diffusion significantly deviate from the simple Poisson-like behavior found for hopping between neighboring sites.^[23] Specifically, the attachment/detachment of a vacancy to the diffusing species may result in abrupt changes in its mobility, which was never observed in our experiments. Vacancy-assisted diffusion of S_{ad} on Cl-covered Cu(100) would therefore only be in accordance with the observed statistical behavior if vacancies are either permanently attached to each S_{ad} or if vacancy attachment/detachment occurs on much faster time scales than the average time between jumps, for example, due to a fast adsorption equilibrium between Cl_{ad} and chloride in the electrolyte. To clarify the S_{ad} diffusion mechanism in more detail, ab initio calculations are in progress, which could shed light on the role of Cl_{ad} coadsorbates and vacancies.^[24]

2.2. S_{ad} Dynamics in the Presence of Neighboring S_{ad}

At small distances the mutual interactions of the sulfur adsorbates strongly influence the surface dynamic behavior. This can be seen for example, in Figure 2 where between 0 and 250 ms two S_{ad} in the upper right corner of the image (marked by a dashed circle), which occupy nearest and next-nearest neighbor sites, respectively, undergo several jumps. These positional fluctuations occur on a much faster timescale than the diffusion of more isolated S_{ad} , which under these conditions jump only about once every 5 s to a neighbor site (see

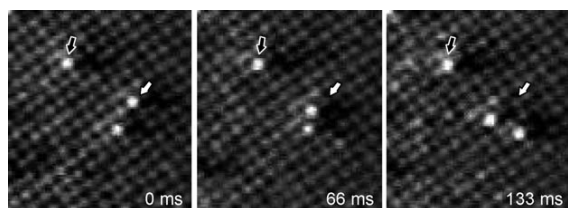


Figure 5. Subsequent images taken from an in situ video-STM sequence ($35 \times 35 \text{ \AA}^2$, frame rate 15 Hz) of S_{ad} on Cu(100) in 0.01 M HCl at -0.47 V_{SCE} and 293 K, showing the enhanced surface dynamics of neighboring S_{ad} .

Figure 4), indicating that neighbor species increase the surface mobility by an order of magnitude. A second example, obtained at -0.47 V where the average jump rate of isolated S_{ad} is $\approx 3 \text{ s}^{-1}$, is presented in Figure 5 and likewise shows clearly enhanced jump rates for neighboring S_{ad} (center of images, white arrow) as compared to isolated species (upper right corner, black arrow). Similar behavior was found in all video-STM sequences, independent of potential and temperature.

A quantitative analysis of this phenomenon is possible for S_{ad} dimers that are well separated from all other S_{ad} ($> 4a_0$). As shown in previous studies under UHV conditions,^[5] the video data for such dimers can be analyzed by two-particle jump distribution functions, from which the modified jump rates and the adsorbate–adsorbate interaction energies at different S_{ad} separations can be extracted via a master equation model. The resulting site-dependent S_{ad} – S_{ad} interaction energies, that is, the interatomic interaction potential for these adsorbates, is presented in Figure 6. The curves for the two video-STM sequences, which were independently recorded at similar electrode potentials, are in good agreement, demonstrating that reliable adsorbate interaction potentials can be obtained by this method. For the studied potentials clearly repulsive interactions are found for nearest-neighbor sites as well as at distances of $2a_0$ whereas between next-nearest-neighbor sites and (to a lesser extent) at distances of $\sqrt{5}a_0$ the interaction is attractive. In addition, the S_{ad} diffusion barriers were clearly decreasing with decreasing S_{ad} – S_{ad} spacing, resulting in more than an order of magnitude higher jump rates for atoms in

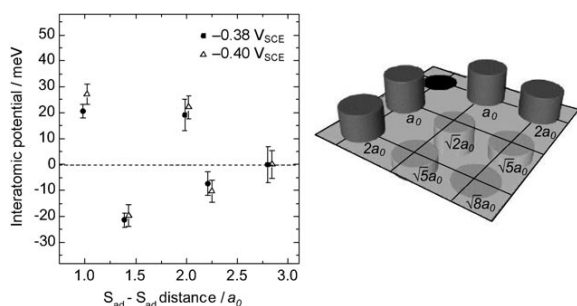


Figure 6. S_{ad} – S_{ad} interaction potential obtained from a detailed quantitative analysis of dimer dynamics in two in situ video-STM sequences. In the 2D representation (right) the interaction energy for different S_{ad} positions relative to the second S_{ad} in the reference position (●) is shown with the plane denoting the origin of the energy scale.

nearest-neighbor sites. A detailed description of this quantitative analysis of the adsorbate–adsorbate interactions is given elsewhere.^[25]

These quantitative data are in accordance with the observation that S_{ad} are seldom and only transiently found on neighboring, but very frequently on next-nearest neighbor sites. Furthermore, this interaction potential is consistent with the $p(2 \times 2)$ structure found at low coverages for S_{ad} on Cu(100) under UHV conditions^[13] and in the electrochemical environment.^[15] The repulsive interactions between S_{ad} on neighboring $c(2 \times 2)$ lattice sites may be rationalized by the known tendency of adsorbed sulfur to induce an outward relaxation of the underlying Cu surface atoms, resulting in opposing strain fields for an S_{ad} dimer in this geometry.^[13] In contrast, S_{ad} in next-nearest neighbor sites share a component of this strain field, which should lead to less repulsive or even net attractive interactions. In addition, electronic interactions mediated by the metal substrate may contribute. The range of the interactions is in agreement with recent studies by infrared spectroscopy^[26] and surface resistivity measurements,^[27] which reported an unusual nonlinear behavior at low S_{ad} coverages. The latter results were attributed to significant overlap of the adsorbate wave functions at distances up to approximately 6 to 7 Å, that is, at similar distances as the effective spatial extension of the interaction potential obtained herein, and were also found to affect the coadsorption of CO in this range.^[26]

2.3. S_{ad} Dynamics near Cu Steps

Surface defects such as the steps of the Cu substrate likewise have a pronounced influence on the dynamic behavior of the sulfur adsorbates. On Cu(100) in 0.01 M HCl the steps are structurally well defined in the presence of the $c(2 \times 2)$ Cl adlattice, consisting of long straight sections parallel to the [001] directions with a low kink density.^[16,17] In this section the S_{ad} dynamics on the upper terrace near descending steps is discussed, where the adsorbates can clearly be observed. Imaging of the sulfur adsorbates on the lower terraces is usually difficult in the constant-height-mode video-STM frames, as the larger tip-sample distance results in strongly reduced image contrast. For this reason, no clear data on the interactions of S_{ad} with ascending steps could be obtained.

An example of the S_{ad} interaction with steps is shown in Figure 7 where the diffusion of an isolated S_{ad} near a step can be traced over a time of 0.5 s (several frames where the adsorbate position remained constant were omitted). Immediately after approaching the step at the characteristic tracer diffusion rate found at this potential ($\approx 10 \text{ s}^{-1}$), the S_{ad} appears to be transiently pinned, that is, it neither moves parallel nor away from the step for 400 ms (Figure 7, 134 to 467 ms). The latter indicates that adsorbates at descending steps experience a deeper potential well. As discussed in detail by Kyuno and Ehrlich^[28] such step–edge traps have been experimentally observed for a number of systems under UHV conditions. In particular, pinning of sulfur adsorbates at the upper terrace side of steps was also found in the UHV–STM study on the vicinal Cu(100) surface by Masson et al.^[14] In that study an even lower

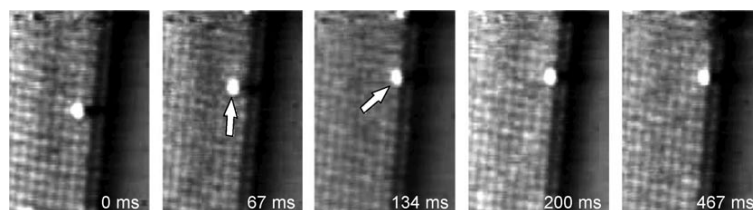


Figure 7. Selected images taken from an in situ video-STM sequence ($70 \times 50 \text{ \AA}^2$, frame rate 15 Hz) of S_{ad} on Cu(100) in 0.01 M HCl at $-0.52 V_{\text{SCE}}$ and 293 K, showing the S_{ad} diffusion near a Cu step.

S_{ad} mobility than in our experiments was reported, with S_{ad} being positional stable on the time scale of minutes, suggesting a reduced diffusion barrier in the electrochemical environment. Furthermore, adsorbate trapping at step edges was also found in several density functional theory studies, for example, for N and O on stepped Ru(0001)^[29] and Br on stepped Cu(111)^[30] surfaces, where it was attributed to changes in the local electronic structure of substrate atoms at steps, specifically to a positive shift of the metal d-band center.^[29] The adsorbates are not completely pinned at steps, but detach with a certain probability. For example, the S_{ad} in Figure 7 detaches from the step by moving back onto the upper terrace after 1.2 s. As for S_{ad} on the terraces (see section 3.1.) the adsorbate mobility at steps is much higher than that found in the UHV-STM study by Masson et al.^[14]

Due to these trapping effects, the average residence time of S_{ad} in the surface areas near steps is significantly enhanced. The resulting accumulation of S_{ad} near the steps can clearly be observed in the STM images (Figure 8). In accordance with the results on $S_{\text{ad}}-S_{\text{ad}}$ interactions presented in Section 3.2. the adsorbates are preferentially arranged at next-nearest-neighbor distances along the step edge. In some areas even small metastable patches of a $p(2 \times 2)$ S_{ad} adlattice structure can be recognized (example marked by arrow in Figure 8, 334 ms), a consequence of the higher local coverage in these areas. Similar, but larger metastable $p(2 \times 2)$ islands were also found on the Cu terraces at larger S_{ad} coverages, in accordance with the previous

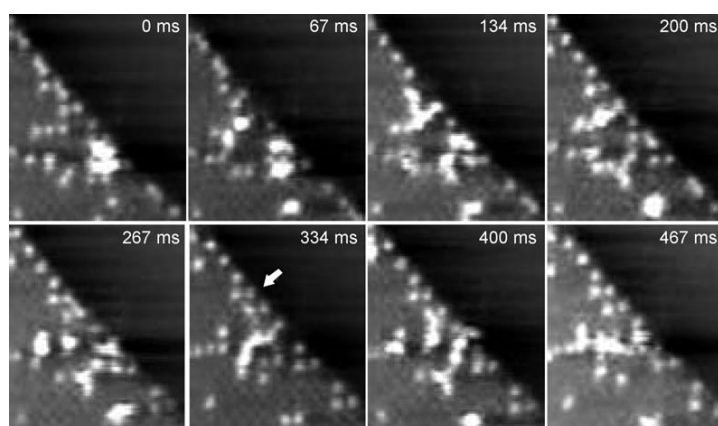


Figure 8. Subsequent images of an in situ video-STM sequence ($51 \times 43 \text{ \AA}^2$, frame rate 15 Hz) of S_{ad} on Cu(100) in 0.01 M HCl at $-0.32 V_{\text{SCE}}$ and 290 K. S_{ad} accumulation near the step edge and the formation of metastable $p(2 \times 2)$ islands on the upper terrace in the lower left part of the images is clearly visible.

in situ STM results by Spaenig et al.^[15] The adsorbate configurations in the sequence in Figure 8 exhibit clear changes between successive images ($\Delta t = 67 \text{ ms}$), that is, the S_{ad} mobility is much higher than for isolated adsorbates (e.g. as shown in Figure 7), despite the more positive potential. This again is a manifestation of the significant enhancement

of the S_{ad} mobility by neighboring coadsorbates.

2.4. S_{ad} Dynamics in $c(2 \times 2)$ Domain Boundaries

Another defect in the perfect $c(2 \times 2)$ Cl adlayer that affects the S_{ad} dynamics are translational domain boundaries (Figure 9, boundary marked by arrow), which were observed in a few of the video sequences. These boundaries can be recognized by the anti-phase shift of the adsorbate rows on both sides of the boundary with respect to each other. Near the boundaries the $c(2 \times 2)$ lattice cannot be resolved clearly, but the lattice appears blurred even at image acquisition rates of 20 s^{-1} . These blurred areas extend over an area as wide as 2 to 7 lattice spacings around the boundary, indicating that the Cl adsorbates in this range change their position faster than the time between successive scan lines ($\leq 0.2 \text{ ms}$). We attribute this behavior to rapid positional fluctuations of the domain boundaries, which is also supported by the pronounced changes in the position and extension of these blurred areas between successive video-STM images.

The boundaries motion is strongly impeded by sulfur adsorbates, which act as pinning centers. This is illustrated by the boundary visible in Figure 9, whose position in all the images coincides with the position of several S_{ad} . In agreement with such a pinning effect, the extension of the blurred areas is typically much smaller at the location of S_{ad} (see for example, Figure 9, 0 ms, upper border) than in those further away from S_{ad} species (same image, lower border). As a second example, selected images from a long video sequence are shown in Figure 10, where a boundary slowly sweeps from left to right through the imaged area over a time of $\approx 1 \text{ min}$. Obviously, the boundary motion is much slower than that expected on the base of the rapid boundary fluctuations in the S_{ad} -free areas. In fact, domain boundaries in the $c(2 \times 2)$ Cl adlayer were only observed in the presence of S_{ad} , whereas in extensive previous video-STM studies of Cu(100) in sulfide-free HCl solution^[7,9] the Cu terraces always appeared to

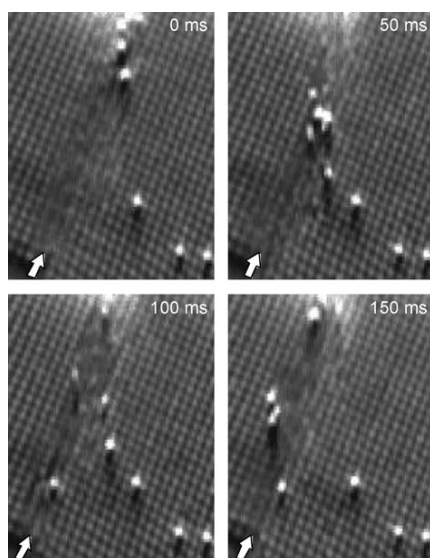


Figure 9. Subsequent images of an in situ video-STM sequence ($90 \times 110 \text{ \AA}^2$, frame rate 20 Hz) of S_{ad} on Cu(100) in 0.01 M HCl at $-0.32 \text{ V}_{\text{SCE}}$ and 297 K, showing the interaction of S_{ad} with a domain boundary (marked by arrows) in the $c(2 \times 2)$ -Cl adlattice.

be covered by a single $c(2 \times 2)$ domain. Probably the fast, unimpeded domain boundary motion within the pure Cl adlayer either prevents the STM imaging of these boundaries or leads to rapid ripening of the domain distribution, resulting in a single domain on each terrace. Only in the presence of the pinning S_{ad} species the domain fluctuations become sufficiently slow to allow observation of the boundaries, although even then domain boundaries are found rather rarely.

Vice versa, the sulfur adsorbates are pinned by domain boundaries and therefore tend to accumulate in these areas. During the boundary motion, S_{ad} are incorporated and temporarily trapped in the area close to the boundary, leading to a locally increased S_{ad} coverage (particular well visible in Figure 10 at 34 s). Since the Cl_{ad} surface density is reduced along the domain boundaries,^[31] this suggests net repulsive interactions between S_{ad} and Cl_{ad} species or, phrased differently, a net attraction between S_{ad} and defects in the Cl adlayer. As at step edges, the trapping of S_{ad} at domain boundaries is only a transient effect (typically for several seconds in the video se-

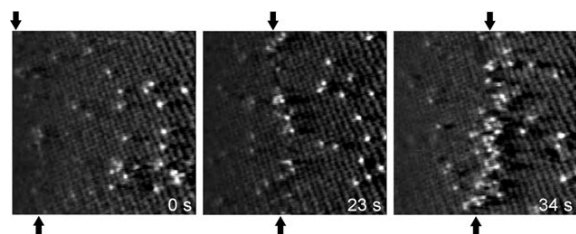


Figure 10. Selected images of an in situ video-STM sequence ($160 \times 160 \text{ \AA}^2$, frame rate 20 Hz) of S_{ad} on Cu(100) in 0.01 M HCl at $-0.32 \text{ V}_{\text{SCE}}$ and 297 K. During the recording of the image a domain boundary (marked by arrows), accompanied by a local accumulation of S_{ad} , was slowly sweeping from left to right through the image.

quences partly shown in Figure 9 and 10), after which the adsorbates are ejected again from the boundary, indicating that S_{ad} binding energies at domain boundaries are not much larger than a few tens of meV. More quantitative studies were not possible due to the rather rare observation of domain boundaries.

In addition to these trapping effects, the surface mobility of S_{ad} along the domain boundaries is strongly enhanced as compared to that of S_{ad} within the undistorted $c(2 \times 2)$ domains. For example, in Figure 9 the S_{ad} in or close to the domain boundary are typically displaced by 3 to 4 lattice spacings between subsequent images, whereas those within the domain (e.g. in the lower right corner of the images) do not move at all on this time scale (average jump rate for isolated S_{ad} is 0.2 s^{-1} under the conditions of this experiment). That is, the S_{ad} diffusion in domain boundaries is apparently accelerated by approximately two orders of magnitude, suggesting that the chloride coadsorbates indeed may block the S_{ad} hopping and that these blocking effects are reduced in the more open boundaries. As illustrated in the model in Figure 11, S_{ad} motion along the domain boundary may occur via jumps across a bridge site to a neighboring fourfold hollow site of the Cu substrate lattice, with the adsorbate crossing over to the other translational domain (indicated by arrows). The energy barrier associated with such jumps is expected to be lower than that for direct jumps between two sites of the $c(2 \times 2)$ lattice within a single domain of the Cl adlayer, resulting in an increased probability for this process. By a sequence of such jumps, where the S_{ad} is alternating between the two domains, rapid diffusion along the boundary should be possible. Together with the enhancement of the S_{ad} diffusion in the electrochemical environment discussed in Section 2.1, this mechanism may explain the much higher mobility along domain boundaries as compared to S_{ad} within the domains and on the bare Cu surface in vacuum.

3. Conclusion

Our detailed video-STM data on sulfur adsorbate dynamics on Cu(100) electrodes reveal complex and partly unexpected behavior, demonstrating that on the atomic scale the present understanding of such processes at electrochemical interfaces is

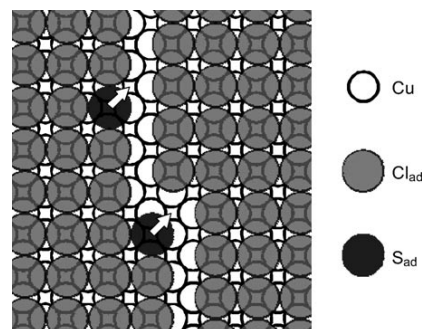


Figure 11. Schematic model of a domain boundary in the $c(2 \times 2)$ adlayer.

sketchy at best. The S_{ad} adsorbates occupy sites of the $c(2 \times 2)$ adlayer and diffuse within this lattice via sequential jumps between neighboring sites, providing a well-defined model system. The potential dependence of the diffusion barrier can be rationalized by electrostatic contributions, caused by the interaction of the adsorbate dipole moment with the electric field of the double layer. However, the much higher diffusion rate as compared to S_{ad} on clean Cu(100) under UHV conditions is surprising and cannot be fully explained at present. Specifically, in the electrochemical system the sulfur adsorbate is surrounded by a close-packed adlayer of chloride coadsorbates, which is expected to block the S_{ad} diffusion, as also suggested by the enhanced S_{ad} mobility along domain boundaries. That the opposite, namely an increased surface mobility, is observed, points toward drastic modifications of the adsorbate-substrate interactions in the electrochemical environment, probably induced by coadsorbates and solvent molecules. On the other hand, the extension of the adsorbate-adsorbate interactions and the trapping of S_{ad} at the upper terrace side of the steps closely resemble observations for this adsorbate system under vacuum conditions.

These results may have important consequences for detailed models of electrochemical processes involving adsorbed species, such as surface phase transitions or electrocatalytic reactions. Although up to now restricted to a single adsorbate system, our data indicate that the dynamic behavior of electrochemical adsorbates may often be considerably more complex than anticipated in current models of electrode reactions. For example, an enhancement of the mobility by neighboring adsorbates as observed here will result in a steep increase in surface mass transport rates with coverage, with corresponding effects on the reaction kinetics. Even more important may be the strong potential dependence of the diffusion barrier, which apparently can be comparable to that of the charge transfer kinetics. Whether these phenomena can be observed in other adsorbate systems and how the potential-dependent diffusion barriers and interaction energies are related to the adsorbed species, coadsorbates, and the substrate will be a challenge for future quantitative studies.

Acknowledgements

We thank the Deutsche Forschungsgemeinschaft for financial support via MA 1618/5-3. A.T. gratefully acknowledges a fellowship by the Deutscher Akademischer Austauschdienst.

Keywords: adsorption · adsorbate-adsorbate interactions · interfaces · scanning tunneling microscopy · surface chemistry

- [1] G. Ehrlich, *Scanning Microsc.* **1990**, *4*, 829.
- [2] J. V. Barth, *Surf. Sci. Rep.* **2000**, *40*, 75.
- [3] T. Tansel, O. M. Magnussen, *Phys. Rev. Lett.* **2006**, *96*, 026101.
- [4] G. Ehrlich, F. Watanabe, *Langmuir* **1991**, *7*, 2555.
- [5] S. Renisch, R. Schuster, J. Winterlin, G. Ertl, *Phys. Rev. Lett.* **1999**, *82*, 3839.
- [6] L. Zitzler, B. Gleich, O. M. Magnussen, R. J. Behm, *Proc. Electrochem. Soc.* **2000**, 99–28, 29.
- [7] O. M. Magnussen, L. Zitzler, B. Gleich, M. R. Vogt, R. J. Behm, *Electrochim. Acta* **2001**, *46*, 3725.
- [8] O. M. Magnussen, W. Polewska, L. Zitzler, R. J. Behm, *Faraday Discuss.* **2002**, *121*, 43.
- [9] W. Polewska, R. J. Behm, O. M. Magnussen, *Electrochim. Acta* **2003**, *48*, 2915.
- [10] M. Labayen, C. Ramirez, W. Schattke, O. M. Magnussen, *Nat. Mater.* **2003**, *2*, 783.
- [11] M. Labayen, O. M. Magnussen, *Surf. Sci.* **2004**, *573*, 128.
- [12] M. Labayen, C. Haak, O. M. Magnussen, *Phys. Rev. B* **2005**, *71*, 241409.
- [13] H. C. Zeng, R. A. McFarlane, K. A. R. Mitchell, *Phys. Rev. B* **1989**, *39*, 8000.
- [14] L. Masson, L. Barbier, J. Cousty, B. Salanon, *Surf. Sci.* **1995**, *338*, 60.
- [15] A.S. paenig, P. Broekmann, K. Wandelt, *Z. Phys. Chem.* **2003**, *217*, 459.
- [16] D. W. Suggs, A. J. Bard, *J. Phys. Chem.* **1995**, *99*, 8349.
- [17] M. R. Vogt, F. Möller, C. M. Schilz, O. M. Magnussen, R. J. Behm, *Surf. Sci.* **1996**, *367*, L33.
- [18] M. R. Vogt, A. Lachenwitzer, O. M. Magnussen, R. J. Behm, *Surf. Sci.* **1998**, *399*, 49.
- [19] J. Lecoq, J. P. Bellier, *Electrochim. Acta* **1985**, *30*, 1027.
- [20] R. Q. Hwang, J. Günther, J. Schröder, S. Günther, E. Kopatzki, R. J. Behm, *J. Vac. Sci. Technol. A* **1992**, *10*, 1970.
- [21] L. Chiodo, P. Monachesi, *Phys. Rev. B* **2007**, *75*, 075404.
- [22] W. Polewska, M. Bazarnik, O. M. Magnussen, unpublished results.
- [23] R. van Gastel, E. Somfai, S. B. van Albada, W. van Saarloos, J. W. M. Frenken, *Phys. Rev. Lett.* **2001**, *86*, 1562.
- [24] J. Stremme, E. Pehlke, unpublished results.
- [25] A. Taranovskyy, T. Tansel, O. M. Magnussen, unpublished results.
- [26] X. F. Hu, C. J. Hirschmugl, *Phys. Rev. B* **2005**, *72*, 205439.
- [27] R. G. Tobin, *Surf. Sci.* **2003**, *524*, 183.
- [28] K. Kyuno, G. Ehrlich, *Surf. Sci.* **1997**, *394*, L179.
- [29] B. Hammer, *Surf. Sci.* **2000**, *459*, 323.
- [30] D. M. Rampulla, A. J. Gellman, D. S. Sholl, *Surf. Sci.* **2006**, *600*, 2171.
- [31] Due to size constraints, heavy domain walls with an increased packing density seem unlikely. In that case the chloride adsorbates would have to approach to a distance of one Cu surface lattice spacing, which would require substantial overlap of their ion cores.

Received: December 1, 2009

Published online on March 18, 2010

4.4. MC simulation of high coverage structures

Of particular interest was a possible effect of the electrode potential on the interactions between the sulphur adsorbates. From the data of $V_{pair}(r_i)$ presented in Fig. 3 in the preceding PRL paper [80] it is not obvious to draw a solid conclusion due to some scatter in the experimental data. Nevertheless, some tendency to have more long range interactions could be observed at more positive potentials. Indeed, one can recognize more pronounced repulsion at the 3rd and attraction at the 4th neighbour sites at $-0.40 V_{SCE}$ and $-0.38 V_{SCE}$ comparing to the data at more negative potentials $-0.49 V_{SCE}$ and $-0.47 V_{SCE}$.

The formation of adsorbate surface phases correlates with the lateral adsorbate-adsorbate pair interactions [82–84]. Slight changes in the interaction energies may result in the observation of different adlayer structures [85]. In our test simulations, we have chosen two typical sets of $V_{pair}(r_i)$ obtained for $-0.40 V_{SCE}$ and $-0.47 V_{SCE}$ representing both distinct distance dependences in order to check which surface phases at higher coverages would correspond to the given interatomic potentials.

As was previously reported by Spaenig in his STM study of electrochemically deposited sulfide layers on Cu(100) a transition from a highly defective $p(2 \times 2)$ to a more stable $c(2 \times 6)$ phase was observed [78]. This transition was explained exclusively by the increased coverage of the sulfide adsorbates.

In our analysis, the high coverage phases were simulated by the MC procedure using the values of $V_{pair}(r_i)$ obtained for $-0.40 V_{SCE}$ and $-0.47 V_{SCE}$ (shown in Fig. 4.2a and 4.2c) as input parameters. In these simulations, the total energy of the system H (in an assumption that the interactions are pairwise additive) was minimized by a series of arbitrary changes of the adsorbate positions. As distinct from the MC simulations described in the previous section, in the present simulations only changes in adsorbate distributions which decreased the total energy of the system $\Delta H < 0$ were accepted.

The simulated adsorbate distributions are shown in Fig. 4.2b and 4.2d for two different coverages $\theta = 0.25$ ML and $\theta = 0.33$ ML respectively. On these figures the Cu substrate is not depicted but only the $c(2 \times 2)$ adlayer with S_{ad} (black circles) and Cl_{ad} (white circles). As shown in Fig. 4.2b, in simulations at coverage $\theta = 0.25$ ML, one can observe domains of a $c(2 \times 6)$ phase with two different surface coverages, $\theta = 0.17$ ML and $\theta = 0.33$ ML, respectively, whereas at coverage $\theta = 0.33$ ML, only a $c(2 \times 6)$ phase with this coverage exists. Therefore, the formation of a $c(2 \times 6)$ phase occurs independent of the surface coverage for the interatomic potential $V_{pair}^I(r_i)$. However, in the case of potential $V_{pair}^{II}(r_i)$, we observe the formation of a $p(2 \times 2)$ phase at coverage $\theta = 0.25$ ML and domains of $p(2 \times 2)$

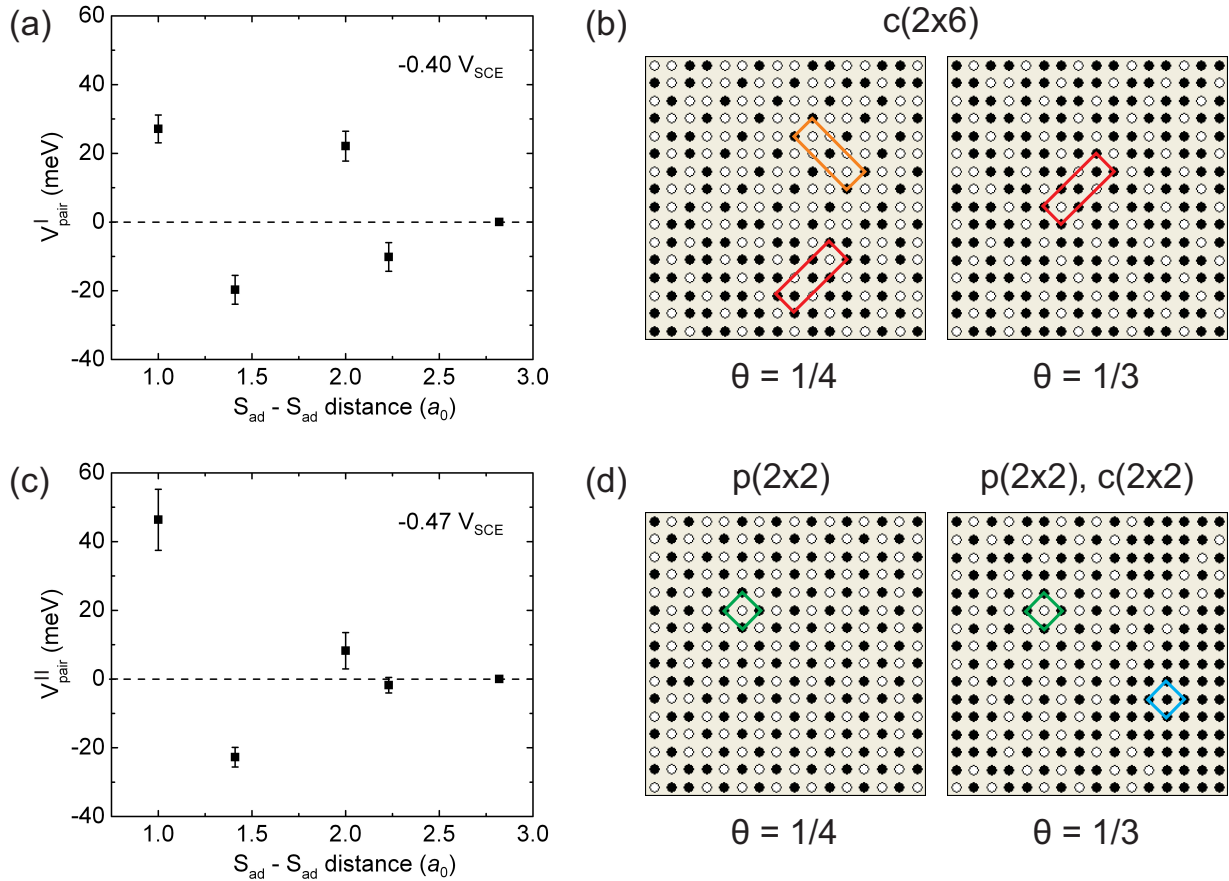


Figure 4.2.: a) The interatomic potential $V_{pair}^I(r_i)$ measured at $-0.40 V_{SCE}$ and b) the corresponding simulated $c(2 \times 6)$ structures at surface coverages $\theta = 0.25$ ML and $\theta = 0.33$ ML. c) The interatomic potential $V_{pair}^{II}(r_i)$ measured at $-0.47 V_{SCE}$ and d) the corresponding simulated $p(2 \times 2)$ structure at the same coverages. Here, by simply increasing the S_{ad} coverage the formation of the $c(2 \times 6)$ phase can not be observed. Unit cells of surface phases are marked respectively: $c(2 \times 6)$ phase with $\theta = 0.17$ ML by orange rectangle, $c(2 \times 6)$ phase with $\theta = 0.33$ ML by red rectangle, $p(2 \times 2)$ by green square, $c(2 \times 2)$ by blue square.

and $c(2 \times 2)$ phases at coverage $\theta = 0.33$ ML. The simultaneous existence of a $p(2 \times 2)$ and a $c(2 \times 2)$ phase certainly can not correspond to the real case but is a coverage effect. In our simple model, the many-body effects and elastic energy terms, which usually make considerable contributions at high coverages, were not included. Anyway, the results show a tendency to obtain the two different surface phases, already reported in literature [78, 79], for the given interatomic potentials, also in accordance with the potential dependence of the transition of the given phases.

The observed trend can be qualitatively explained by the different interaction energies at distances of $2a_0$ in the pairwise potentials $V_{pair}^I(r_i)$ and $V_{pair}^{II}(r_i)$. In the case of $V_{pair}^{II}(r_i)$, the repulsion energy 8 ± 5 meV at distance of $2a_0$ is rather small as compared to the repulsion energy 46 ± 9 meV at nearest-neighbor site and the attraction energy -23 ± 3 meV at next-nearest-neighbor site. Thus, the simulated $p(2 \times 2)$ structure is determined by the last two interaction energies [86]. In the case of $V_{pair}^I(r_i)$, the repulsion energy 22 ± 4 meV at distance of $2a_0$ is comparable to interaction energies at shorter distances, 27 ± 4 meV and 22 ± 4 meV at nearest-neighbor and next-nearest-neighbor sites, respectively, and therefore makes a considerable contribution to the total surface energy. Consequently a $c(2 \times 6)$ structure formed, where the distances of $2a_0$ between the adsorbates occur 1.5 times less often than in a $p(2 \times 2)$ structure, despite 1.33 times higher coverage of adsorbates.

As follows from our data, in the simulations for both potentials any transition of $p(2 \times 2)$ and $c(2 \times 6)$ surface structures was observed. Therefore, the transition from the $p(2 \times 2)$ to the $c(2 \times 6)$ phase may be caused not just by increasing the surface coverage, as was proposed before [78], but can be driven also by the changes in $V_{pair}(r_i)$, induced by the electrode potential.

4.5. Adsorbate mobility and residence times

The dynamic method allows to determine not only the interatomic potentials but also gives full information about the mobility of one adsorbate located at close distances to another. This is a main advantage of the dynamic method as compared to the equilibrium method. From the extracted set of energy parameters—adsorption sites and saddle point energies—one can obtain the diffusion activation barriers in the direction of the jump by using eq.(3.1) and consequently the corresponding hopping rates from eq.(3.2). Their values can be directly compared with the tracer diffusion barrier. One example of the data obtained at -0.47 V_{SCE} is shown in Fig. 4.3. The diffusion barrier of isolated adsorbates is equal to $E_{\infty}^D = 710$ meV at this potential. The figure gives information about the differences

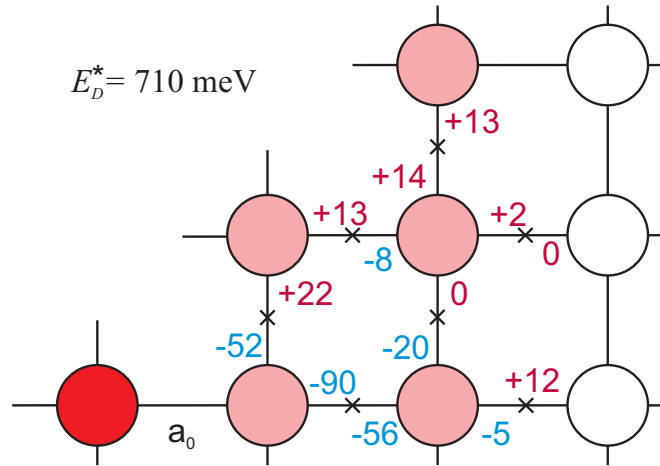


Figure 4.3.: The differences of the modified jump activation barriers (given in meV) of S_{ad} diffusing in the close neighborhood of another S_{ad} as compared to an isolated S_{ad} obtained at an electrode potential of $-0.47 V_{SCE}$. The measured value of the tracer diffusion barrier is $E_{\infty}^D = 710$ meV.

between the corresponding jump barriers and the tracer diffusion barrier. The motion of adsorbates in this case is different from a random walk since jump barriers strongly depend on the direction of the jump. A significant reduction of barriers is observed for jumps out of the sites $1a_0$ and $2a_0$, which are known for their repulsive interactions. It is interesting that this reduction can be even bigger than just the repulsive modification of adsorption sites ($V_{pair}(1a_0) = +46$ meV). This is due to the fact that the saddle point energies undergo considerable modifications as well (see Fig. 4.4). Here the highest modification is observed for the transition state energy E_{13}^S between two repulsive adsorption sites — $r = a_0$ and $r = 2a_0$. It indicates a quite complex behavior of S_{ad} during the jumping process on Cu(100) in the neighborhood of another S_{ad} within the $c(2 \times 2)$ matrix of Cl coadsorbates.

In addition, we have calculated the total hopping rate out of the adsorption sites $\Gamma_i(r_i)$ according to eq.(3.5). Results for different dimer separations between $1a_0$ and $\sqrt{10}a_0$ and for isolated adsorbates are given in Fig. 4.5 as a function of electrode potential. A common trend in these data is the similar electrode potential dependency, with mobility decreasing towards positive potentials for all separations between S_{ad} and for isolated S_{ad} as well. The hopping rates of S_{ad} out of repulsive sites with separations of $1a_0$ and $2a_0$ are distinctly higher than those for all other separations, which are comparable close to hopping rate of isolated adsorbates. Especially it is strongly pronounced for S_{ad} at nearest neighbour configuration where the mobility is higher one order of magnitude. For all of separations

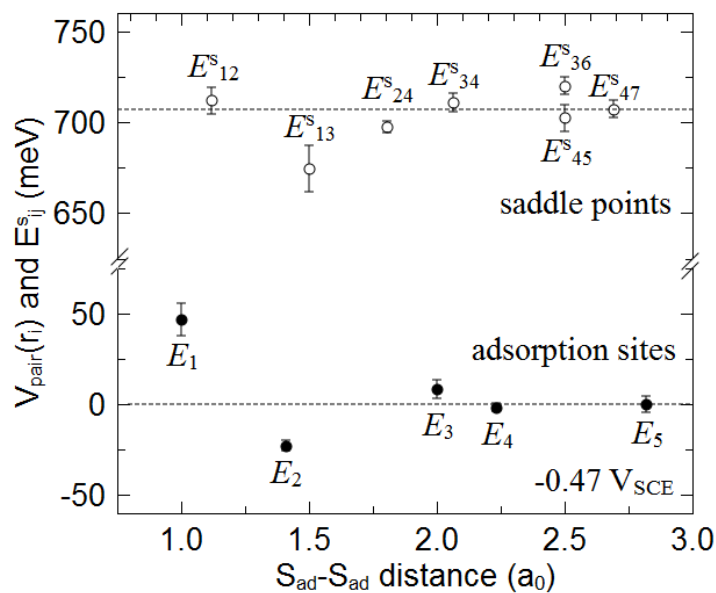


Figure 4.4.: Pairwise interaction potential $V_{pair}(r_i)$ and transition-state energies E_{ij}^S for the S adsorbates.

except $\sqrt{2}a_0$, $\Gamma_i(r_i)$ can be represented as exponential decay function of electrode potential with approximately similar decay parameter.

From the given data, the residence time of S_{ad} located at a distance r_i from another S_{ad} , can be obtained as the inverse of the corresponding hopping rate out of this site:

$$\tau(r_i) = \frac{1}{\Gamma_i(r_i)}. \quad (4.1)$$

The residence times τ as a function of the distance r_i between two S_{ad} and the electrode potential Φ are shown in a generalized 3D plot in Fig. 4.6. The obtained results are in agreement with the previously discussed shape of $V_{pair}(r_i)$. For adsorption sites $1a_0$ and $2a_0$ characterized by repulsive interactions we observe a local minimum of residence times as could be expected. For $r_i > 2a_0$, the residence time doesn't change significantly with the distance and have values close to the residence time of the isolated adsorbate.

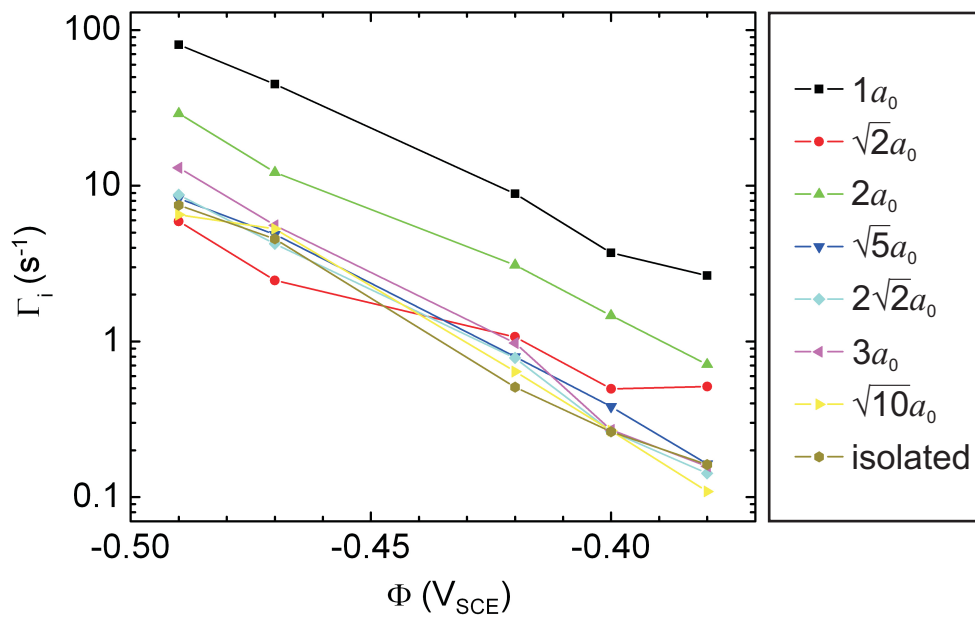


Figure 4.5.: Jump rates out of the adsorption sites for S_{ad} located at different distances from another S_{ad} as a function of electrode potential.

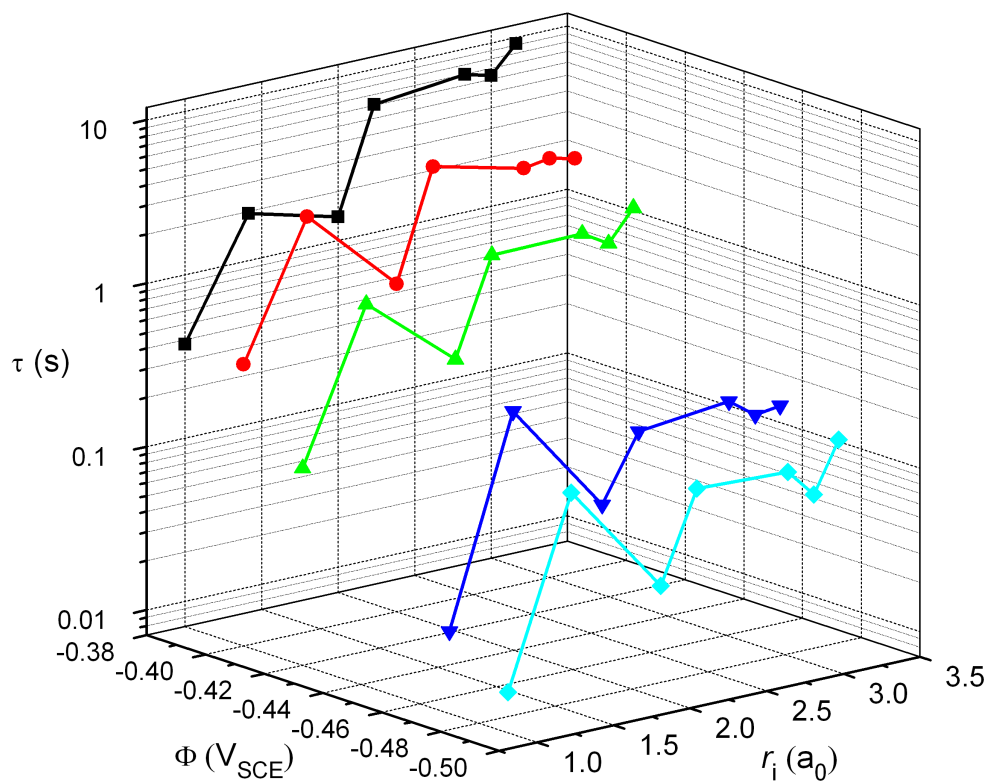


Figure 4.6.: Residence time of S_{ad} in the close neighborhood of another S_{ad} as a function of their separation r_i and electrode potential Φ .

5. *In situ* STM study of Pb on Cu(100) in Cl containing solution

5.1. Pb surface diffusion and interactions

In the previous studies ([1,80], chapter 4 of this thesis) the tracer diffusion and adsorbate–adsorbate interactions of anionic sulphur adsorbates on Cu(100) in solution of 0.1 M HCl were studied by *in situ* high speed STM. To reveal the general effect of electrochemical environment and, particularly, the effect of adsorbate type and halide adlayer on adsorbate diffusion and interactions we have chosen for further identical study the same system, i.e, the Cu(100) single crystal surface pre-covered by Cl $c(2 \times 2)$ adlayer in aqueous solution of 0.01 M HCl, with the only distinction that Pb adsorbates, which have a different, cationic nature, were added to the solution at a similar concentration. The choice of Pb adsorbates was due to their higher surface diffusion activation barriers as compared to other metallic adatoms [87–91] and consequently the lower jump rates, allowing the direct tracing of single Pb_{ad} motion in the electrode potential range -0.17 to -0.29 V_{SCE} . In this potential regime Pb_{ad} are present on the surface at coverages of a few percent of a monolayer. The reported results on the Pb adsorbates diffusion barrier on Cu(100) under UHV conditions are -0.68 eV, obtained in a quantitative Rutherford backscattering study by Cohen et al. [92], and -0.831 eV in an atom-tracking STM study by Anderson et al. [91]. The latter showed a the presence of vacancy assisted mechanism of Pb_{ad} diffusion, where the pronounced lead–vacancy attraction leads to the existence of Pb_{ad} long jumps and, consequently, the jump distribution was different from a simple random walk.

The image recognition software described in the Chapter 2 was applied for video data processing. Depending on the imaging conditions, in the STM images Pb_{ad} were visible as protrusions or depressions (Figures 1 and 2 in the following paper). In the latter case, as the most simple solution, the grey color scheme in the STM images was inverted and the following recognition analysis was identical as for S_{ad} . Thus, the quantitative analysis of relative distances between Pb adsorbates showed that they are occupying positions within the $c(2 \times 2)$ adlattice. The obtained series of digital occupation maps, providing information

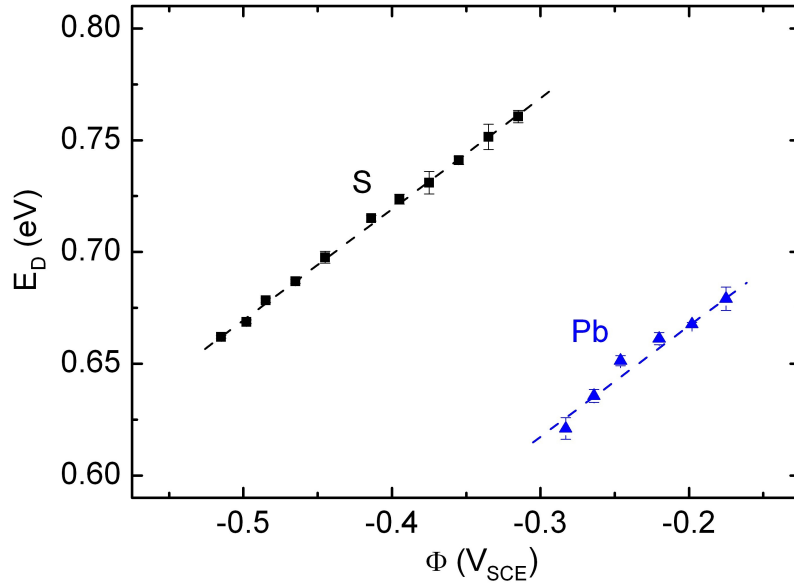


Figure 5.1.: Activation barriers of tracer diffusion measured for S_{ad} (black squares) and Pb_{ad} (blue triangles) on Cu(100) in 0.01 M HCl. The data are taken from Ref. [1] and [94] respectively.

about the Pb distribution on the $c(2 \times 2)$ lattice at regular time intervals, were used as input data for further statistical analysis of adsorbate tracer diffusion and adsorbate–adsorbate interactions.

In contrast to the data for Pb_{ad} tracer diffusion under UHV condition [91], the jump distributions of isolated Pb_{ad} could be described in terms of a two-dimensional random walk model with hopping only between neighboring sites. The jump rates and corresponding activation barriers were extracted from the fit of the theoretical model [93] to the experimentally obtained jump distributions. In the studied potential regime, the obtained absolute values of diffusion barrier were in the range 0.65 to 0.72 eV (Fig. 5.1). The diffusion barriers exhibited a linear dependence on electrode potential with a slope of -0.5 ± 0.1 eV/V, similar in sign and magnitude as in the previous study of S_{ad} diffusion on Cu(100) [1]. This result was quite surprising since according to the eq.(1.4) for cationic species with positive dipole moment one would expect a slope with opposite sign. This behavior was rationalized by a significant influence of Cl coadsorbates on the Pb_{ad} hopping process. Since Pb_{ad} is located within the $c(2 \times 2)$ matrix of Cl adlayer, any change of its position would lead to the displacements of surrounding Cl_{ad} from their adsorption sites. Therefore, the change of the total surface dipole moment during hopping would have contributions from Pb_{ad} as well as Cl_{ad} . Because of the similar potential dependence of the activation barriers as in the case of S_{ad} , one could conclude that the contribution of the distorted Cl adlayer plays

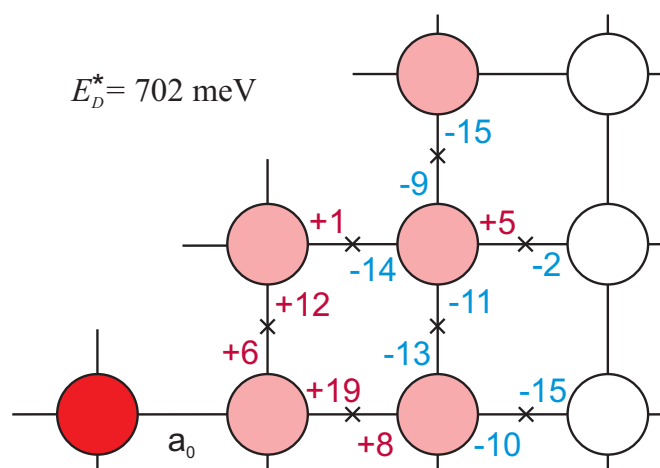


Figure 5.2.: The differences of the modified jump activation barriers (given in meV) of Pb_{ad} diffusing in the close neighborhood of another Pb_{ad} as compared to an isolated one for an electrode potential of $-0.20 \text{ V}_{\text{SCE}}$. The measured value of the tracer diffusion barrier is $E_{\infty}^D = 702 \text{ meV}$.

a dominant role in both cases.

In addition, a single video data set recorded at -0.20 V was selected for measurements of the pairwise interactions $V_{\text{pair}}(r_i)$ between Pb_{ad} by quantitative methods described in details in Chapter 3. The dynamic method based on the analysis of the relative motion of Pb_{ad} dimers revealed attractive interactions for nearest and next nearest neighboring sites with absolute values of $15 - 25 \text{ meV}$. Simultaneously, the transition-state energies were extracted, which together with adsorption sites energies, provide the complete information on the modification of the local energy landscape by interadsorbate interactions. Based on these data, it was found that average diffusion barriers are about $5\text{-}20 \text{ meV}$ higher at close distances between adsorbates (up to $1.5a_0$) and $10\text{-}15 \text{ meV}$ lower at intermediate distances ($1.5a_0$ to $2.5a_0$) as compared to the diffusion barrier of isolated Pb_{ad} (Fig. 5.2).

The effective interadsorbate potential $V_{\text{eff}}(r_i)$ determined from the analysis of spatial distribution of Pb_{ad} showed a satisfactory agreement with the pairwise potential $V_{\text{pair}}(r_i)$ in distance dependence as well as in absolute values, which is the consequence of low adsorbate coverage in the present case, where local adsorbate configurations containing considerable number of Pb_{ad} meet rarely and thus the contribution of many-body effects is rather small.

**5.2. Publication The Journal of Physical Chemistry C 115,
19336(2011).**

Reprinted with permission from The Journal of Physical Chemistry C **115**, 19336(2011).
Copyright (2011) American Chemical Society [94]. The article is available via the internet
at <http://pubs.acs.org/doi/full/10.1021/jp2079988>.

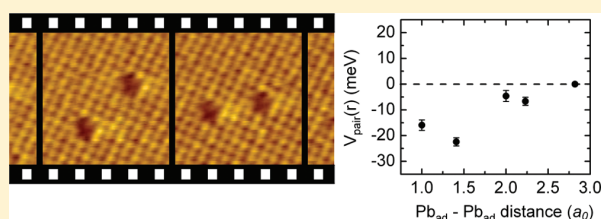
Surface Dynamics of Lead Adsorbates at the Cu(100)–Electrolyte Interface

Sophie Guézo,[†] Andriy Taranovskyy, Hisayoshi Matsushima,[‡] and Olaf M. Magnussen*

Institut für Experimentelle und Angewandte Physik, Christian-Albrechts-Universität zu Kiel, 24098 Kiel, Germany

Supporting Information

ABSTRACT: Direct quantitative studies of the dynamic behavior of individual cationic adsorbates at an electrochemical interface have been performed for Pb on Cu(100) electrode surfaces in Cl-containing electrolyte. Using in situ high-speed scanning tunneling microscopy, the motion of the Pb adsorbates on the $c(2 \times 2)$ -Cl covered Cu surface was monitored and analyzed by statistical models. Contrary to Pb on Cu(100) under ultrahigh vacuum conditions, the tracer diffusion of isolated adsorbates can be described by simple activated hopping between neighboring sites within the $c(2 \times 2)$ lattice, with an activation energy that increases linearly by 0.5 eV/V with potential. This surprising behavior, which is opposite in sign to that expected for a cation and similar to that for adsorbed sulfide at this interface, suggests a decisive influence of the surrounding Cl coadsorbates on the Pb diffusion. Furthermore, attractive interactions of ~ 20 meV were found between Pb adsorbates on nearest and next-nearest neighbor sites of the $c(2 \times 2)$ lattice. The effective diffusion barriers are increased in the vicinity of neighboring Pb, resulting in a mutual stabilization of the adsorbates.



I. INTRODUCTION

The surface dynamics of adsorbates and interactions between them are of key importance in numerous interface processes, such as crystal growth and dissolution, self-assembly processes, and catalytic reactions. Specifically, the adsorbate dynamics also plays a significant role in such processes at interfaces between metal electrodes and liquid electrolytes. Contrary to surfaces under ultrahigh vacuum (UHV) conditions, where surface diffusion and adsorbates interactions have been extensively studied by high-resolution microscopic techniques, for example, field ion microscopy (FIM)^{1–4} or scanning tunneling microscopy (STM),^{5–8} only very limited information on adsorbates dynamics at electrochemical interfaces exists. This is largely due to the high mobility of adsorbates at room temperature and the lack of sufficiently fast in situ techniques that allow a direct study of the elementary dynamic processes on the electrode surface with atomic resolution. Consequently, the influence of the complex environment at metal–electrolyte interfaces, for example, the presence of surface charges, corresponding electric fields, and coadsorbed species, is only poorly understood. Qualitatively, a pronounced influence of the potential and electrolyte composition on the surface dynamics has been frequently observed. Especially for the self-diffusion of metal surface atoms, an increase in surface mobility toward more positive potentials, resulting in enhanced mass transport, is well documented^{9–11} and in accordance with theoretical considerations that explain this effect by an electrostatic energy contribution, resulting from the interaction of the metal adsorbate's dipole moment with the electric field in the electrochemical double layer.^{11,12} However, in all of those experimental studies, the dynamic processes were deduced only indirectly from

observations of time-dependent changes in the nanoscale surface morphology. Direct observations of the elementary steps in metal adatom dynamics have not yet been reported.

Of particular importance for understanding surface dynamic processes at solid–liquid interfaces is clarifying the role of coadsorbate species, for example, counterions and solvent molecules, which necessarily are a component of these systems. In particular, chemisorbed species, such as halide ions, are well-known for their decisive influence on interface processes. For example, chloride ions are an indispensable additive in modern electroplating methods for the microelectronics industry,¹³ and adsorbed bromide is a “spectator” species in electrocatalytic processes, which can strongly modify the electrode kinetics without actually participating in the actual chemical interface reactions.¹⁴ These effects are generally attributed to an influence of these coadsorbates on the dynamics and interactions of the reacting species. However, deeper insight into these phenomena is impeded by the lack of direct data on the atomic-scale dynamics in such coadsorption systems.

Recently, the development of electrochemical video-STM^{15–17} has allowed first quantitative studies of the surface diffusion and the adsorbate–adsorbate interactions of an adsorbed anion at a metal–electrolyte interface, specifically of sulfide on Cu(100) electrode surfaces in HCl solution.^{15,18} In the investigated potential range, where the surface is covered by a $c(2 \times 2)$ -Cl adlayer, isolated sulfide adsorbates were found to move via thermally activated hopping between neighboring sites of the $c(2 \times 2)$ lattice. The activation energy increases linearly with

Received: August 19, 2011

Published: August 26, 2011

electrode potential by 0.50 eV per V,¹⁵ which could be rationalized by changes in the adsorbate dipole moment during the hopping process. Furthermore, the potential energy surface for sulfide in the neighborhood of other sulfide adsorbates was elucidated, revealing repulsive as well as attractive adsorbate–adsorbate interactions.¹⁸ Here we present first studies of this type for a cationic adsorbate species – adsorbed lead. To better assess how the adsorbate type (anion or cation) affects the dynamic behavior, especially its potential dependence, the same well-defined electrochemical system was chosen, that is, $c(2 \times 2)$ -Cl-covered Cu(100) in 0.01 M HCl solution.

According to previous studies under UHV conditions, the diffusion barrier for Pb on Cu(100) is rather high as compared with other metallic species,^{19–23} making this adsorbate species particularly suitable for video-STM measurements.^{20,24} The high barrier was attributed to partial embedding of the Pb atom into the Cu surface, resulting in energetically deep adsorption sites. Lead adsorption on Cu(100) in the submonolayer range is also of interest for other reasons, for example, the immiscibility of Pb and Cu in the bulk and the large mismatch of 37%, and represents a well-known adsorbate system, investigated thoroughly in UHV^{21,25–27} and electrochemical environment.^{25,26} In both environments, the presence of isolated adsorbates with low surface mobility has been observed at surface coverages of a few percent,^{20,22,23,28,29} followed by a variety of ordered phases that involve Pb surface alloying and reconstruction of the Cu substrate with increasing coverage.³⁰ Under UHV conditions, quantitative Rutherford backscattering studies by Cohen et al. of the Pb surface diffusion on Cu(100) in the low-coverage regime at temperatures between 473 and 638 K reported a diffusion barrier of 0.68 eV.²⁴ More recently, detailed microscopic studies of isolated Pb adsorbates near room temperature were performed by Anderson et al. using atom-tracking STM,²³ revealing a vacancy-assisted diffusion mechanism with an activation barrier of 0.831 eV and a prefactor of $10^{12.4} \text{ s}^{-1}$.

Here we present a quantitative video-STM study of the dynamic behavior of isolated lead adsorbates on Cu(100) electrodes in HCl solution within the potential regime where the surface is covered by the ordered Cl $c(2 \times 2)$ adlayer. Surprisingly, the Pb surface mobility does not increase toward more positive potentials, as deduced for other metal adatoms in electrochemical environment,^{9–11} but decreases. In fact, the surface diffusion of this cationic adsorbate has a very similar potential dependence as adsorbed (anionic) sulfide.¹⁵ As will be discussed below, this observation indicates that the potential-dependent term in the diffusion barrier is dominated by coadsorbates. Furthermore, our data allow direct comparison with the tracer diffusion of Pb on Cu(100) under UHV conditions, revealing a different diffusion mechanism in electrochemical environment. In addition, we present first data on Pb–Pb interactions on the Cu surface, which are relevant to an in-depth understanding of the Pb phase formation processes at higher coverage.

II. EXPERIMENTAL DETAILS

Before each experiment, the Cu(100) single crystal electrode was electropolished in orthophosphoric acid (66%) and rinsed with sufficient amounts of ultrapure water, avoiding contact of the electrode surface with air. The sample was then immersed in 0.1 M HClO₄ solution, containing 30 μM Pb²⁺ and 2 mM NaCl, which was prepared from high-purity HClO₄ (Merck, suprapure), NaCl (Alfa Aesar, Puratronic 99,999%), Pb(ClO₄)₂·3H₂O

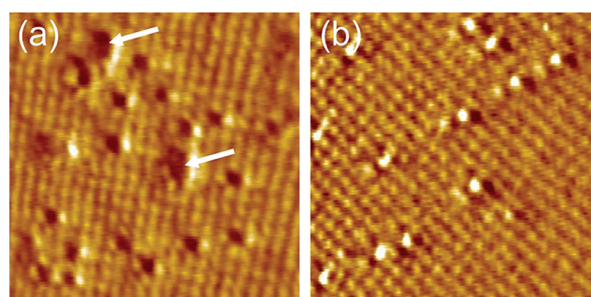


Figure 1. In situ video-STM images of Pb_{ad} on Cu(100), covered by the $c(2 \times 2)$ -Cl adlayer at (a) $-0.13 \text{ V}_{\text{SCE}}$ ($7.8 \times 7.8 \text{ nm}^2$) and (b) $-0.27 \text{ V}_{\text{SCE}}$ ($7.0 \times 7.0 \text{ nm}^2$). Arrows in part a mark examples where two Pb_{ad} are separated by the minimal distance a_0 .

(Alfa Aesar, Reagent grade, min 97%), and ultrapure water. Potentials were measured versus a Pt wire, calibrated with a reference saturated calomel electrode (SCE).

The STM experiments were performed in an electrochemical cell at controlled working electrode potential (-0.17 to $-0.29 \text{ V}_{\text{SCE}}$) and room temperature (290 K). Our home-built video-STM^{16,17} allows measurements in electrochemical environment with a rate of up to 20 images per second in constant height mode. Images are slightly high-pass filtered and hence appear as if illuminated from the left. Video sequences with a duration of 1 to 3 min were recorded, containing several hundred up to a few thousand images. This allows collection of data suitable for statistical analysis of the adsorbate surface dynamics. Typically, tunneling currents of 9–18 nA and a bias of several hundred millivolts were used.

The experimental video data were processed by an image recognition software developed by our group, which permits automatic recognition of the Pb_{ad} positions on the square $c(2 \times 2)$ lattice and converted those into series of binary occupation maps, describing the Pb_{ad} distribution on the surface at regular time intervals. These maps were subsequently analyzed by the statistical methods described below.

III. RESULTS AND DISCUSSION

III.1. STM Observations at Low Pb Coverage. Before the STM experiments, cyclic voltammograms were obtained in an external cell, employing the same conditions as those in the STM measurements. We observe the typical features previously reported in the literature for this system,^{28,29,31} with underpotential deposition (upd) in the range of -0.45 to $-0.30 \text{ V}_{\text{SCE}}$. In the potential regime between the upd peak and the onset of copper dissolution at about $-0.10 \text{ V}_{\text{SCE}}$, where the STM experiments were performed, the voltammograms are featureless and the Cu(100) surface is completely covered by the $c(2 \times 2)$ -Cl adlayer.^{32,33} The latter is clearly observed in the STM images (square lattice in Figure 1).

In the entire studied potential regime, even at potentials 200 mV more positive than that of the upd peak, we observe isolated adsorbates on the $c(2 \times 2)$ -Cl-covered Cu(100) surface. The surface coverages of these adsorbates are typically a few percent of a monolayer. They appear in the STM images as depressions (Figure 1a) or protrusions (Figure 1b), depending on the imaging conditions. These variations in contrast were already previously reported.^{21,22,28}

As directly visible in the STM images, the Pb adsorbates occupy well-defined positions within the $c(2 \times 2)$ lattice of the

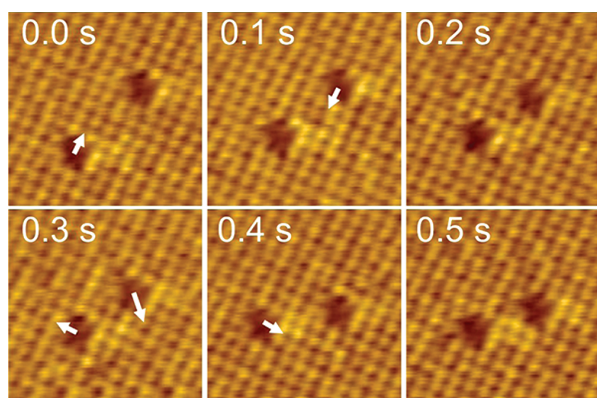


Figure 2. Consecutive in situ STM images of Pb_{ad} diffusion on the $c(2 \times 2)$ -Cl covered Cu(100) surface, taken from a video-STM sequence recorded with a frequency of 10 Hz at $-0.27 \text{ V}_{\text{SCE}}$ ($4.5 \times 4.5 \text{ nm}^2$). Arrows indicate the directions of Pb_{ad} jumps between neighboring $c(2 \times 2)$ lattice sites.

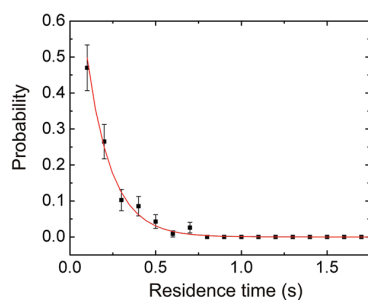


Figure 3. Residence time distribution of isolated Pb_{ad} at a potential $\Phi = -0.25 \text{ V}_{\text{SCE}}$, obtained at a time resolution of 0.1 s from 117 individual events. The data can be described by an exponential decay with a time constant $\tau = 0.14 \text{ s}$ (solid line).

Cl coadsorbates. This was confirmed by a systematic quantitative analysis of the positions of diffusion Pb adsorbates in the STM videos, which exclusively found Pb_{ad} jump lengths corresponding to distances between $c(2 \times 2)$ lattice sites. The closest distance between the Pb adsorbates corresponds to neighbor sites of the $c(2 \times 2)$ lattice, that is, a spacing of $a_0 = 3.61 \text{ \AA}$ (examples marked by arrows in Figure 1a). Whether the Pb_{ad} are embedded in the Cu surface layer, as inferred in UHV-STM studies,^{20,21,27} or are located in form of adatoms on top of the Cu surface, substituting chloride coadsorbates of the $c(2 \times 2)$ adlayer, cannot be ascertained on the basis of the present data. Full videos showing the dynamic behavior of the Pb_{ad} with high time resolution are provided in the Supporting Information.

III.2. Diffusion of Isolated Pb Adsorbates. Pb_{ad} surface diffusion manifested in discrete jumps of these adsorbates between $c(2 \times 2)$ lattice sites, as illustrated in sequence of STM images presented in Figure 2 (jump directions indicated by arrows). Depending on the potential, the typical residence times of an adsorbate in a lattice site are in the range 0.025 to 0.25 s in the investigated potential regime, making tracing individual Pb_{ad} by video-STM possible. As expected, no preferred direction for the adsorbate motion was observed; that is, Pb_{ad} surface diffusion is isotropic. To avoid influencing the adsorbate dynamics by the

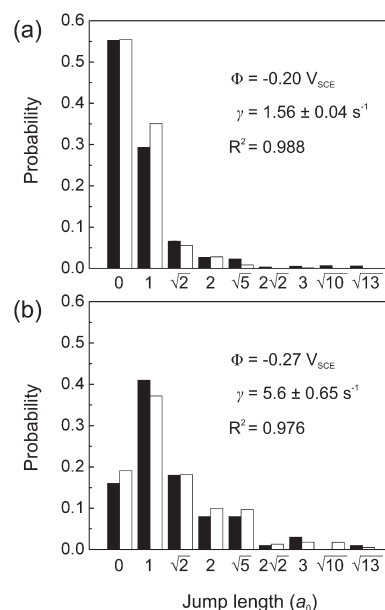


Figure 4. Jump distribution functions and obtained hopping rates γ for isolated Pb_{ad} at two different potentials Φ . Shown are the experimental distributions (black bars), obtained from a statistical analysis of the video-STM data and corresponding best fits by a random-walk model (white bars).

STM tip, the influence of the tunneling conditions was carefully examined. No significant change in the dynamics was found for tunneling currents up to 25 nA.

In our quantitative studies, we first investigated the tracer diffusion of isolated Pb adsorbates. For this, we analyzed the positional changes of Pb_{ad} that exhibited a sufficient separation to all neighboring Pb_{ad} . By systematically varying the minimum $\text{Pb}_{\text{ad}}-\text{Pb}_{\text{ad}}$ spacing, employed as criterion for selecting the analyzed Pb_{ad} , it was found that at separations smaller than three $c(2 \times 2)$ lattice spacings a_0 atomic interactions exert an influence on the adsorbate dynamics. Consequently, for the determination of the Pb_{ad} tracer diffusion, only adsorbates without a neighbor at distances closer than $4a_0$ were considered in the analysis.

First insight into the adsorbate dynamics is provided by the residence time distribution of isolated Pb adsorbates, that is, the probability that a Pb_{ad} occupies the same lattice position for a given time. As visible in the example shown in Figure 3, the data are well-described by an exponential decay function, with a time constant that is the average residence time. These results indicate that Pb_{ad} jumps are uncorrelated in time so that the diffusion can be described as a simple thermally activated hopping.

Pb_{ad} tracer diffusion was investigated by the same method as that in our previous study of sulfide diffusion.^{15,34} From changes of the Pb_{ad} positions between subsequent frames of a video-sequence, experimental jump distributions were obtained, which were fitted by a 2D random walk model. In the latter, only hopping of adsorbates between neighboring lattice sites was considered, with the hopping rate γ being the only free-fit parameter. Two typical experimental jump distribution functions (black bars), obtained at potentials of -0.20 and $-0.27 \text{ V}_{\text{SCE}}$, and the corresponding best fits of the data by the diffusion model (white bars) are presented in Figure 4. Obviously, the model provides a good description of the experimental data (coefficient

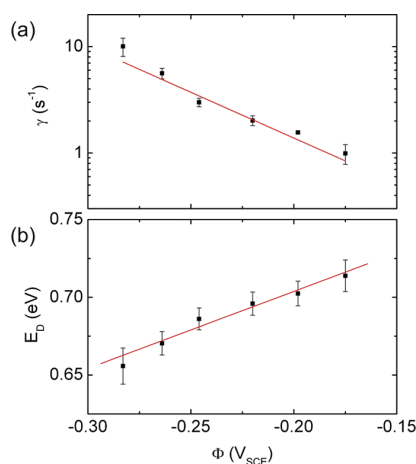


Figure 5. (a) Potential dependence of the hopping rates of isolated Pb_{ad} and (b) corresponding diffusion barriers calculated from part a by assuming an attempt frequency of $2.35 \times 10^{12} \text{ s}^{-1}$. The change of diffusion barriers with potential can be described by a linear increase with a slope of $0.5 \pm 0.1 \text{ eV/V}$.

of determination $R^2 \geq 0.95$), confirming that jumps are independent and occur between neighboring lattice sites. Evidence of “long jumps”, where the adsorbate moves instantaneously over distances of more than one lattice spacing, was not found. A different behavior was reported for Pb_{ad} diffusion on Cu(100) under UHV conditions, where atom-tracking STM studies revealed jump lengths longer than a single lattice spacing.²³ This was attributed to a vacancy-assisted mechanism, in which vacancies in the Cu surface interact attractively with embedded Pb adatoms, strongly accelerating their mobility until the Pb_{ad} –vacancy pair dissociates again. Vacancy-assisted diffusion leads to significantly different jump distribution functions³⁵ and would be easily distinguishable from a simple random walk between neighbor sites. On the basis of our statistical data, this mechanism can clearly be excluded in the electrochemical environment, suggesting a different diffusion process at the metal–electrolyte as compared with the metal–vacuum interface. This may be caused by the presence of the $c(2 \times 2)$ chloride adlayer as well as the double-layer electric field and the associated surface charge, which all may influence the vacancy surface concentration, mobility, and interactions with the Pb adsorbates.

Already the data shown in Figure 4, which are described by hopping rates γ of 1.56 ± 0.04 and $5.6 \pm 0.7 \text{ s}^{-1}$, respectively, indicate that the Pb_{ad} mobility changes substantially with the electrode potential. The hopping rates of all quantitative experiments as a function of potential are represented in Figure 5a, with each data point determined from an analysis of 100 to 4241 individual events observed by video-STM. Surprisingly, the Pb_{ad} hopping rates decrease toward more positive potentials; that is, the potential-dependence of the surface mobility has the opposite in sign as that found in previous experimental of metal surface diffusion.^{9–11} Moreover, this behavior is also contrary to that theoretically expected for a cationic adsorbate species, whose dipole moment should be directed away from the metal surface (“positive dipole moment”), resulting in an increase in mobility at more positive potentials.^{11,12} As will be shown in detail below, this behavior can be rationalized by a decisive contribution of the anionic chloride coadsorbate.

More detailed insight can be obtained from the quantitative potential dependence of the hopping rates. As in our previous study of sulfide surface diffusion,¹⁵ a pronounced, roughly exponential relationship is found. In the former study, temperature-dependent measurements revealed an Arrhenius dependence and a (potential-independent) attempt frequency. Assuming the same holds true in the Pb adsorbate system and that the attempt frequency has the value of $2.35 \times 10^{12} \text{ s}^{-1}$ similar to that found under UHV conditions or for sulfide surface diffusion at this interface,^{15,22} the corresponding potential-dependent diffusion activation barriers were calculated (Figure 5b). As for the sulfide system, these barriers exhibit a linear potential dependence with a slope of $0.5 \pm 0.1 \text{ eV/V}$. In the studied potential regime, the barriers are in the range 0.65 to 0.72 eV, which is comparable to the activation energy of 0.68 eV reported by Cohen et al.²⁴ but lower than the barrier of 0.831 eV found by Anderson et al.²³ In view of the substantial potential dependence and the presence of the Cl coadsorbate layer in the electrochemical environment, a more detailed comparison of the data for Pb_{ad} under UHV and under electrochemical conditions is difficult, however.

Interestingly, the diffusion behavior of Pb_{ad} strongly resembles that found in our previous study of S_{ad} tracer diffusion on Cu(100) under identical conditions.^{15,34} Although the mobility of the Pb_{ad} is two orders of magnitude higher than that of S_{ad} , reflecting its different chemical nature, not only the sign but also the magnitude of the potential-dependent contribution to the diffusion barrier is very similar. For a more detailed discussion of the surprisingly similar dynamic behavior of the anionic S_{ad} and the cationic Pb_{ad} in this system, we briefly review the origin of potential-dependent surface transport. According to current theories on adsorbate dynamics at electrified interfaces, the potential-dependence of surface diffusion (and effectively of all energies associated with surface defects) can be rationalized as an electrostatic energy term, resulting from the interaction of the surface dipole moment of the adsorbate or defect with the electric field of the electrochemical double layer.^{11,12,15} For metallic adsorbates on metal substrates, the surface dipole moments are positive and increase further during the adsorbate hopping because of the lower adatom coordination in the transition state. Because of this, the electrostatic energy contribution to the diffusion barrier should decrease with increasing potential, resulting in higher diffusion rates. Indeed, this type of behavior was found in density functional theory calculations for Cu, Ag, and Au adatoms on (100)-oriented surfaces of the same metals¹² and supported by studies of Au(100) monolayer island ripening in sulfuric acid solutions.¹¹

For a full description of an adsorbate at an electrochemical interface, not only the adsorbate on the (bare) metal surface alone but also its local environment has to be considered, however. Hopping to a neighboring adsorption site will also lead to displacements of counterions and solvent molecules in the vicinity of the studied adsorbate, which contribute to the total dipole moment of the adsorbate complex and consequently the activation energy for diffusion. Hence, the similar potential dependence of the anionic S_{ad} and the cationic Pb_{ad} adsorbate may be explained by a dominant role of the $c(2 \times 2)$ -Cl coadsorbate layer in both cases, that is, the matrix in which the studied adsorbates are embedded on the surface. In this model, the change in surface dipole moment and the corresponding electrostatic energy are primarily determined by the distortion of the surrounding Cl adlayer during the hopping of the adsorbate to a neighboring $c(2 \times 2)$ lattice site. Because displacement of a

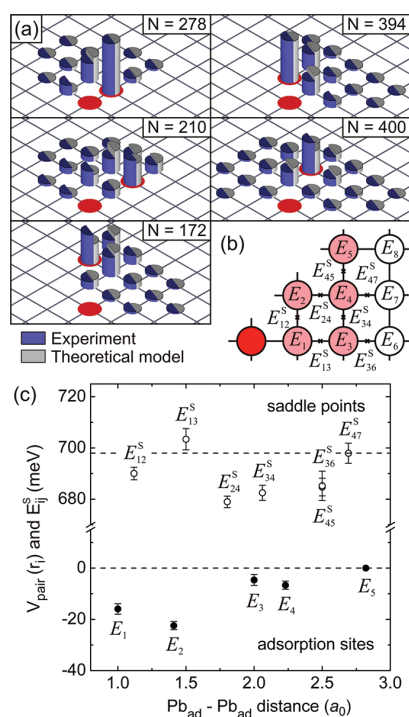


Figure 6. (a) Two-particle jump distribution functions for Pb dimers at five different initial configurations (indicated by red circles) with Pb_{ad}-Pb_{ad} distances of $1a_0$, $\sqrt{2}a_0$, $2a_0$, $\sqrt{5}a_0$, and $2\sqrt{2}a_0$. The functions obtained from the experimental data (dark blue bars, N denotes number of individual observations) are displayed together with the best fit by the theoretical model (light gray bars) and give the probability for a Pb_{ad} to occupy in the final state a specific lattice position relative to the second Pb_{ad} (red circle in the foreground) that serves as a reference. (b) Schematic illustration of the energy parameters employed in the model. (c) Resulting pairwise interaction potential $V_{\text{pair}}(r_i)$ and transition-state energies for the Pb adsorbates.

single Cl_{ad} could account only for a slope up to 0.2 eV/V,¹⁵ this would require a cooperative effect produced by the displacement of several Cl_{ad} in the vicinity of the diffusing sulfide or lead adsorbate. The latter actually is rather likely for a densely packed layer of a chemisorbed coadsorbate species such as the $c(2 \times 2)$ -Cl adlayer, where the Cl-Cl spacing is close to the Cl van der Waals diameter.³⁶ During hopping, the Pb_{ad} or S_{ad} adsorbate has to occupy positions transiently away from $c(2 \times 2)$ lattice sites (e.g., bridge sites or sites of the other $c(2 \times 2)$ sublattice), forcing neighboring Cl_{ad} via hard-core repulsion to deviate from the preferred four-fold-hollow adsorption sites, which will increase their (negative) dipole moment.³⁷ In other words, the adsorbates temporarily occupy interstitial sites of the 2D coadsorbate lattice, generating a longer-range strain field with an associated collective dipole moment in the latter. Support for this was found in a detailed density functional theory study of S_{ad} diffusion on $c(2 \times 2)$ -Cl-covered Cu(100).³⁸ This type of induced dipole moment change in the surrounding coadsorbed chloride layer could account for the sign of the observed potential dependence as well as for the similar magnitude of this effect in Pb_{ad} and S_{ad} surface diffusion.

III.3. Interactions between Pb Adsorbates. In the second part of this work, the interactions between lead adsorbates are

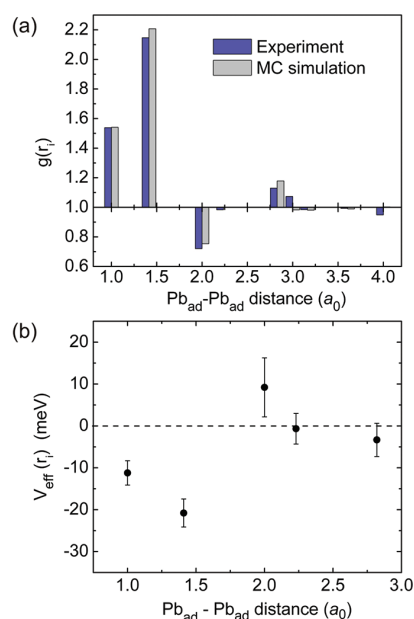


Figure 7. Results of a configuration analysis of Pb_{ad} on Cu(100), using equilibrium distributions generated by Monte Carlo simulations. (a) Experimental Pb_{ad} pair correlation function $g(r_i)$ (dark blue bars) and theoretical $g(r_i)$ (light gray bars), corresponding to the best fit of the data. (b) Resulting effective interaction potential $V_{\text{eff}}(r_i)$.

addressed, which play a central role in understanding the metal growth and the formation of 2D phases in the upd range. Because these studies require very extensive data sets for the statistical analysis, they were performed at a fixed electrode potential of -0.20 V_{SCF}. As in our previous investigation of interactions between sulfide adsorbates, two different methods were used for determining the adsorbate-adsorbate interactions:¹⁸ (i) studies of the dynamics of isolated Pb_{ad} dimers and (ii) analysis of the spatial Pb_{ad} distributions.

The first method is based on studying the temporal changes in the positions of two Pb adsorbates, which are in close vicinity to each other but well-separated (by distances of at least four $c(2 \times 2)$ lattice spacings a_0) from all other Pb_{ad}. Under these conditions, the two neighboring adsorbates mutually influence each other, whereas interactions with other Pb_{ad} are negligible. Because of the mutual interactions between the Pb_{ad} in the dimer, the local energy landscapes (adsorption sites and transition states) for each of the two adsorbates are modified, resulting in a deviation of the Pb_{ad} motion from a simple random-walk (as found in the case of tracer diffusion). To extract the Pb_{ad}-Pb_{ad} interaction potential and the modified activation energies for adsorbate hopping, the experimentally observed adsorbate dynamics is quantified by two-particle jump distribution functions (Figure 6a).^{6,18} These functions describe the probability that a given initial dimer configuration (marked by red circles in the histograms in Figure 6a) evolves into a defined final configuration in the following video-STM image. From the experimental data jump distribution, histograms (dark blue bars) were determined for the five closest Pb_{ad} spacings as initial dimer configuration (i.e., separations of $1a_0$, $\sqrt{2}a_0$, $2a_0$, $\sqrt{5}a_0$, $2\sqrt{2}a_0$). These distribution functions were fitted simultaneously by a model based on the master-equation approach,⁶ which contained as free

parameters the adsorption energies in the four nearest sites to the reference Pb_{ad} (E_1 to E_4) and the transition state energies E_{12}^S to E_{47}^S for jumps between these sites, indicated schematically in Figure 6b. For values $i \geq 5$, the E_i values were assumed to be identical to the adsorption energy of isolated Pb_{ad} .

The calculated distribution functions of the best fit (Figure 6a, light blue bars) and the corresponding energy parameters as a function of the $\text{Pb}_{\text{ad}}-\text{Pb}_{\text{ad}}$ spacing r_i (Figure 6c) are included in the Figure. For the pairwise interaction potentials $V_{\text{pair}}(r_i) = E_i - E_5$, a decrease in energy by 15–25 meV is found for nearest and next-nearest neighbor sites within the $c(2 \times 2)$ lattice, indicating a short-range attractive interaction. At larger distances, the attraction becomes weaker and approaches zero at distances $\geq 2\sqrt{2}a_0 \approx 10 \text{ \AA}$. The average diffusion barriers in the vicinity of a neighboring Pb_{ad} , defined via $E_{ij}^{\text{av}} = E_{ij}^S - (E_i + E_j)/2$, are $E_{12}^{\text{av}} = 0.714 \text{ eV}$, $E_{13}^{\text{av}} = 0.719 \text{ eV}$, $E_{24}^{\text{av}} = 0.693 \text{ eV}$, and $E_{34}^{\text{av}} = E_{45}^{\text{av}} = 0.688 \text{ eV}$. In comparison with the tracer diffusion barrier $E_{\infty}^D = 0.702 \text{ eV}$ at $\Phi = -0.20 V_{\text{SCE}}$, these average barriers are slightly higher (10 to 20 meV) at close distances up to $1.5a_0$ but $\sim 15 \text{ meV}$ lower in the intermediate range ($1.5a_0$ to $2.5a_0$). Hence, our data directly verify that binding to a Pb_{ad} in a directly neighboring $c(2 \times 2)$ lattice site stabilizes a Pb adsorbate, providing a quantitative measure of the elementary nucleation step in Pb deposition on the Cu(100) surface.

Before further discussing the implications of these findings, we present the results of the second method used for determining the $\text{Pb}_{\text{ad}}-\text{Pb}_{\text{ad}}$ interactions, which consists of calculating the effective interaction potential $V_{\text{eff}}(r_i)$, determined from the adsorbate spatial distributions. In this case, first the experimental pair-correlation function $g(r)$ is obtained from the Pb_{ad} spatial distributions of each frame of the video data (Figure 7a, dark blue bars). Obviously, nearest and next-nearest neighbor sites are occupied with a higher probability than in the case of a random distribution (i.e., $g(r) > 1$), indicating attractive interactions in these configurations, in accordance with the results of the dimer analysis (see above). To determine the effective interaction potential, we generated equilibrium configurations and corresponding theoretical pair-correlation functions (Figure 7a, light blue bars) for a given $V_{\text{eff}}(r_i)$ via Monte Carlo simulations,³⁹ assuming pairwise additive interactions. The best description of the experimental data was obtained by the $V_{\text{eff}}(r_i)$ shown in Figure 7b.

The Pb_{ad} interaction potentials $V_{\text{pair}}(r_i)$ and $V_{\text{eff}}(r_i)$ obtained by the two different methods are in good agreement, both in the distance dependence as well as in the absolute energy values. This is not self-evident because $V_{\text{eff}}(r_i)$ contains contributions from larger Pb_{ad} ensembles (e.g., trimers, quadruplets, etc.) whereas $V_{\text{pair}}(r_i)$ represents the true pairwise interaction potential. In particular, the assumption of additive interactions employed in the determination of $V_{\text{eff}}(r_i)$ is often not valid for metallic species. However, in the low-coverage range investigated in this work, the fraction of adsorbates located in larger ensembles is rather small and apparently does not substantially affect the effective adsorbate–adsorbate interactions.

These results agree well with expectations and previous data for the Pb/Cu(100) adsorbate system. Both $V_{\text{pair}}(r_i)$ and $V_{\text{eff}}(r_i)$ indicate an attraction for nearest and next-nearest neighbor sites, as expected for metal adatoms. Furthermore, these interactions would be compatible with the $c(2 \times 2)$ -Pb adlayer phase, found close to the potential of the upd peak^{28,40} as well as under UHV conditions.^{20,41,42} For Pb on clean Cu(100) surfaces under UHV conditions, Pb_{ad} interactions were inferred from macroscopic diffusion data in the study by Cohen et al.²⁴ In that work, the

dependence of the diffusion coefficients on coverage and potential could be reproduced by a simple statistical model with repulsive interactions between Pb_{ad} on nearest neighbor and next-nearest neighbor sites of the Cu substrate lattice (i.e., at adsorbate spacings of $a_0/\sqrt{2}$ and a_0), which clearly is at variance with our results. However, it is not clear whether this truly indicates a difference between the interactions in electrochemical environment and in vacuum or is a consequence of the rather simple model employed by Cohen et al. (e.g., the omission of interactions at larger distances and of modified diffusion barriers) and the much higher Pb coverages in his study.

Overall, the interaction energies obtained in our measurements have a comparable magnitude to those found by direct microscopic studies of metal adatoms and nonmetallic chemisorbed adsorbates.^{4,6,7,18,43,44} Contrary to other adsorbate systems, which report attractive as well as repulsive adsorbate–adsorbate interactions, only $\text{Pb}_{\text{ad}}-\text{Pb}_{\text{ad}}$ attraction is observed, however. For example, for S_{ad} on $c(2 \times 2)$ -Cl-covered Cu(100) electrode surfaces, repulsive interactions to nearest neighbors but attractive ones to next-nearest neighbors were found, which were attributed to indirect elastic interactions via distortions of the substrate lattice.¹⁸ Apparently, these are less pronounced for Pb adsorbates or compensated by the attraction between the metal adatoms. Finally, we point out that the general presence of repulsive interactions cannot be ruled out because the Pb_{ad} are confined to $c(2 \times 2)$ lattice sites in our studies and hence only $\text{Pb}_{\text{ad}}-\text{Pb}_{\text{ad}}$ distances within this superlattice are probed. In particular, a repulsion of Pb_{ad} on neighboring sites of the Cu(100) substrate lattice is likely because of the size mismatch of Pb and Cu. Nevertheless, the good agreement of the measured interactions with those expected for metal adatoms demonstrates that the nature of the adsorbate itself is not altered in the electrochemical environment, supporting our assignment of the inverted potential dependence to the contribution of the coadsorbed chloride anions.

IV. CONCLUSIONS

The presented quantitative in situ video-STM study of lead adatoms on Cu(100) surface in chloride-containing solution provides first direct data on the surface diffusion and adsorbate–adsorbate interactions of metal adsorbates at electrochemical interfaces. The chosen system allowed direct comparison of the adsorbate dynamics under UHV conditions and in electrochemical environment, suggesting a pronounced influence of the latter on the diffusion mechanism and the adsorbate interactions. Even more interesting is the comparison with the data obtained (under identical conditions) for sulfide adsorbates. Although the adsorbate–adsorbate interactions and the absolute diffusion rates of the cationic Pb_{ad} and the anionic S_{ad} species are strongly different, owing to their different chemical nature, both exhibit a linear increase in the activation energy for tracer diffusion with increasing potential, which is identical in sign and magnitude. This has several important implications for adsorbate dynamics at electrochemical interfaces: First, it suggests that strongly potential-dependent surface transport may be a rather general phenomenon at electrochemical interfaces. Hence, this effect, which up to now has been mostly neglected, should be considered to a larger extent in future microscopic modeling of electrochemical processes, such as electrocatalytic reactions, electrodeposition, or surface phase transitions. Second, the surprising similarity in the potential-dependence of the two species can be explained only by a decisive effect of the

coadsorbed chloride adlayer, that is, the local environment of the adsorbates on the electrode surface. Our measurements indicate that coadsorbates can completely dominate the potential dependence of the surface transport processes and even reverse its sign. This sheds new light on the way chemisorbed coadsorbates can significantly affect the electrochemical reactivity, even if they do not participate directly in the reactions (“spectator species”). On the basis of our results, such coadsorbates form an effective 2D medium that can strongly modify the surface transport of the main adsorbate species. This modification is a more subtle effect than simple site blocking: Depending on the change in the collective dipole moment induced in this medium by the adsorbate during the elementary diffusion step, the potential-dependent term in the diffusion barrier can be enhanced, reduced, or even reverted. This phenomenon, on the one hand, makes describing electrochemical interface processes on an elementary level more complex but, on the other hand, allows tuning such processes by suitably chosen coadsorbates, an effect that may be at work in many empirically developed additive systems. Whether coadsorbates exert a similar influence on adsorbate–adsorbate interactions and thus can affect processes such as nucleation or surface reactions remains a challenge for future studies.

■ ASSOCIATED CONTENT

S Supporting Information. In situ STM video of Cu(100) in 0.1 M HClO₄ solution, containing 30 μM Pb²⁺ and 2 mM NaCl at $-0.24 V_{SCE}$, showing the surface diffusion of individual Pb adsorbates (dark depressions) on the c(2 × 2)-Cl covered surface. This material is available free of charge via the Internet at <http://pubs.acs.org>.

■ AUTHOR INFORMATION

Corresponding Author

*E-mail: magnussen@physik.uni-kiel.de.

Present Addresses

[†]Equipe de Physique des Surfaces et Interfaces, Institut de Physique de Rennes, UMR URI-CNRS 6251, Université de Rennes 1, F-35042 Rennes Cedex, France.

[‡]Interdisciplinary Graduate School of Medicine and Engineering, University of Yamanashi, Takeda 4-3-11, Kofu 400–8511 Japan.

■ ACKNOWLEDGMENT

We acknowledge financial support by the Deutsche Forschungsgemeinschaft via MA 1618/14 and MA 1618/15.

■ REFERENCES

- (1) Tsong, T. T. *J. Chem. Phys.* **1971**, *55*, 4658.
- (2) Tsong, T. T. *Phys. Rev. Lett.* **1973**, *31*, 1207.
- (3) Kellogg, G. L.; Tsong, T. T.; Cowan, P. *Surf. Sci.* **1978**, *70*, 485.
- (4) Ehrlich, G.; Watanabe, F. *Langmuir* **1991**, *7*, 2555.
- (5) Mo, Y. W. *Phys. Rev. Lett.* **1993**, *71*, 2923.
- (6) Renisch, S.; Schuster, R.; Wintterlin, J.; Ertl, G. *Phys. Rev. Lett.* **1999**, *82*, 3839.
- (7) Österlund, L.; Pedersen, M. Ø.; Stensgaard, I.; Laegsgaard, E.; Besenbacher, F. *Phys. Rev. Lett.* **1999**, *83*, 4812.
- (8) Trost, J.; Zambelli, T.; Wintterlin, J.; Ertl, G. *Phys. Rev. B* **1996**, *54*, 17850.
- (9) Nichols, R. J.; Magnussen, O. M.; Hotlos, J.; Twomey, T.; Behm, R. J.; Kolb, D. M. *J. Electroanal. Chem.* **1990**, *290*, 21.
- (10) Giesen, M. *Prog. Surf. Sci.* **2001**, *68*, 1.
- (11) Giesen, M.; Beltramo, G.; Dieluweit, S.; Müller, J.; Ibach, H.; Schmickler, W. *Surf. Sci.* **2005**, *595*, 127.
- (12) Müller, J. E.; Ibach, H. *Phys. Rev. B* **2006**, *74*, 085408.
- (13) Vereecken, P. M.; Binstead, R. A.; Deligianni, H.; Andricacos, P. C. *IBM J. Res. Dev.* **2005**, *49*, 3.
- (14) Strmcnik, D. S.; Rebec, P.; Gaberscek, M.; Tripkovic, D.; Stamenkovic, V.; Lucas, C.; Markovic, N. M. *J. Phys. Chem. C* **2007**, *111*, 18672.
- (15) Tansel, T.; Magnussen, O. M. *Phys. Rev. Lett.* **2006**, *96*, 026101.
- (16) Zitzler, L.; Gleich, B.; Magnussen, O. M.; Behm, R. J. *Proc. Electrochem. Soc.* **2000**, *99–28*, 29.
- (17) Magnussen, O. M.; Zitzler, L.; Gleich, B.; Vogt, M. R.; Behm, R. J. *Electrochim. Acta* **2000**, *46*, 3725.
- (18) Taranovskyy, A.; Tansel, T.; Magnussen, O. M. *Phys. Rev. Lett.* **2010**, *104*, 106101.
- (19) Seebauer, E. G.; Allen, C. E. *Prog. Surf. Sci.* **1995**, *49*, 265.
- (20) Nagl, C.; Platzgummer, E.; Haller, O.; Schmid, M.; Varga, P. *Surf. Sci.* **1995**, *331*, 831.
- (21) Robert, S.; Gauthier, S.; Bocquet, F.; Rousset, S.; Duvault, J. L.; Klein, J. *Surf. Sci.* **1996**, *350*, 136.
- (22) Nagl, C.; Haller, O.; Platzgummer, E.; Schmid, M.; Varga, P. *Surf. Sci.* **1994**, *321*, 237.
- (23) Anderson, M. L.; Bartelt, B. S.; Swartzentruber *Surf. Sci.* **2003**, *538*, 53.
- (24) Cohen, C.; Girard, Y.; Leroux-Hugon, P.; L’Hoir, A.; Moulin, J.; Schmaus, D. *Eur. Phys. Lett.* **1993**, *24*, 767.
- (25) Li, W.; Vidali, G. *Phys. Rev. B* **1993**, *48*, 8336.
- (26) Gauthier, Y.; Moritz, W.; Hösler, W. *Surf. Sci.* **1996**, *345*, 53.
- (27) Robert, S.; Cohen, C.; L’Hoir, A.; Moulin, J.; Schmaus, D.; Barthes-Labrousse, M. G. *Surf. Sci.* **1996**, *365*, 285.
- (28) Moffat, T. P. *J. Phys. Chem. B* **1998**, *102*, 10020.
- (29) Vasiljevic, N. Ph.D. Thesis, Arizona State University, 2004.
- (30) Joco, V.; Martínez-Blanco, J.; Segovia, P.; Vobornik, I.; Michel, E. G. *Phys. Condens. Matter* **2009**, *21*, 474216.
- (31) Brisard, G. M.; Zenati, E.; Gasteiger, H. A.; Marković, N. M.; Ross, P. N., Jr. *Langmuir* **1997**, *13*, 2390.
- (32) Gründer, Y.; Kaminski, D.; Golks, F.; Krug, K.; Stettner, J.; Magnussen, O. M.; Franke, A.; Stremme, J.; Pehlke, E. *Phys. Rev. B* **2010**, *81*, 174114.
- (33) Vogt, M. R.; Lachenwitzer, A.; Magnussen, O. M.; Behm, R. J. *Surf. Sci.* **1998**, *399*, 49.
- (34) Tansel, T.; Taranovskyy, A.; Magnussen, O. M. *ChemPhysChem* **2010**, *11*, 1438.
- (35) Van Gastel, R.; Somfai, E.; Van Albada, S. B.; Van Saarloos, W.; Frenken, J. W. M. *Surf. Sci.* **2002**, *521*, 10.
- (36) Magnussen, O. M. *Chem. Rev.* **2002**, *102*, 679.
- (37) Franke, A.; Pehlke, E. *Phys. Rev. B* **2010**, *82*, 205423.
- (38) Stremme, J.; Franke, A.; Pehlke, E., private communication.
- (39) Metropolis, N.; Rosenbluth, A. W.; Rosenbluth, M. N.; Teller, A. H.; Teller, E. *J. Chem. Phys.* **1953**, *21*, 1087.
- (40) Wu, H. C.; Yau, S. L. *J. Phys. Chem. B* **2001**, *105*, 6965.
- (41) Hoesler, W.; Moritz, W. *Surf. Sci.* **1982**, *117*, 196.
- (42) Hoesler, W.; Moritz, W.; Tamura, E.; Feder, R. *Surf. Sci.* **1986**, *171*, 55.
- (43) Pedersen, M. Ø.; Österlund, L.; Mortensen, J. J.; Mavrikakis, M.; Hansen, L. B.; Stensgaard, I.; Laegsgaard, E.; Nørskov, J. K.; Besenbacher, F. *Phys. Rev. Lett.* **2000**, *84*, 4898.
- (44) Mitsui, T.; Rose, M. K.; Fomin, E.; Ogletree, D. F.; Salmeron, M. *Phys. Rev. Lett.* **2005**, *94*, 036101.

5.3. Underpotential deposition of metals

At a metal surface Me in contact with an electrolyte solution, containing metal ions Me^{z+} of the same species as the substrate, processes of adsorption and desorption of metal atoms and an associated electrochemical reaction occur: $\text{Me} \rightleftharpoons \text{Me}^{z+} + ze^-$. Under thermodynamic equilibrium this reaction proceed at the same rate in both directions. Such condition can be established at an equilibrium potential E_{eq} which is determined by the Nernst equation:

$$E_{eq} = E_{eq}^0 + \frac{RT}{zF} \ln a_{\text{Me}^{z+}}. \quad (5.1)$$

where E_{eq}^0 is the standard electrode potential, z is the electron transfer number, $a_{\text{Me}^{z+}}$ is the activity of metal ions in the solution (equal to concentration in dilute solutions), R is the universal gas constant, T is the temperature, and F is the Faraday constant.

If an applied electrode potentials is below the equilibrium potential $E < E_{eq}^0$, adsorption processes dominate ($\text{Me} \leftarrow \text{Me}^{z+} + ze^-$) and bulk deposition starts, if it is above $E > E_{eq}^0$, then desorption prevails ($\text{Me} \rightarrow \text{Me}^{z+} + ze^-$) and the metal electrode dissolves.

The deposition of metal ions Me^{z+} on a foreign metal substrate S can have distinctive features. If the interactions between the metal adsorbates and the substrate (Me-S) are stronger then the interactions between the metal adsorbates (Me-Me), the deposition starts already at potentials that can be significantly less negative than the equilibrium potential E_{eq} . In this case one speaks of underpotential deposition (upd) [95–97]. Depending on the studied system (the strength of interactions) it proceeds by formation of one or two metal monolayers on the substrate [98]. From the thermodynamic point of view this means that the chemical potential of metal atoms in monolayer is lower then the chemical potential in a bulk metal phase: $\mu_{\text{ML}} < \mu_{\text{Me}}$. For potentials $E < E_{eq}^0$, the Me bulk deposition begins (so-called overpotential deposition), similar as in the case of deposition of Me adsorbates on the same metal surface Me. The underpotential deposition leads to the formation of 2D well-ordered Me adsorbate overlayer structures or 2D Me-S surface alloy phases. The structure of upd surface phases and their properties depend on the crystallographic orientation of the electrode and can be varied with an adsorbate coverage.

Electrochemical methods such as measurements of cyclic voltamogramms (CV) has been commonly applied for studies of the underpotential deposition on polycrystalline [99–102] as well as on monocrystal metal surfaces [103–107]. Starting with an electrode potential at which no adsorption takes place and performing a negative potential scan with a slow

sweep rates (1-20 mV/s) one can detect a characteristic increase of the cathodic current, corresponding to underpotential deposition. It can be observed as one or several current peaks, which are related to different surface structures formed during the upd. The negative scan usually terminates at the onset of bulk deposition, i.e. at the Nernst potential. Then the potential scan is changed in opposite (positive) direction and dissolution of the upd layer occurs, observed as an anodic current peak (or several of them). Repeating these cycles many times may indicate if the upd reaction is reversible.

5.4. Pb surface alloying and dealloying

Deposition of Pb on Cu(100) in the submonolayer regime has been studied in detail in the last decades and showed similarities in surface structure formation under ultra-high vacuum condition [90, 108–111] as well as at electrochemical interfaces [112, 113, 117]. The formation of a $c(4 \times 4)$ surface alloy phase consisting of alternating Pb and Cu monoatomic chains at a Pb coverage of 0.375 ML was reported both in UHV [88, 90, 108, 114] and electrochemical environment [112], however, in the second case there was no direct proof of the given structure. Increase of the Pb coverages causes dealloying and successive formation of overlayer structures: the $c(2 \times 2)$ at 0.5 ML and $c(5\sqrt{2} \times \sqrt{2})R45^\circ$ at 0.6 ML [88, 90, 115–118].

In the electrochemical environment, where the Pb coverage can be easily controlled by changing the electrode potential, surface processes during Pb underpotential deposition and dissolution can be studied by in situ STM [112]. It was found that in the presence of Cl ions in the solution, which form a $c(2 \times 2)$ adlayer in a wide potential range, different morphological changes during Pb deposition/dissolution were observed. The most distinctive feature was the formation of a labyrinth network of Pb stripes during Pb dissolution. They were regarded as remnants of $c(4 \times 4)$ alloy phase, however no atomic resolution images were provided to confirm this assignment.

In the present study we focus on dynamic changes during Pb alloying/dealloying processes on Cu(100) in 0.01 M HCl. By successively decreasing the electrode potential into the upd range, the Pb alloy phase nucleates at the steps and continuously spreads along the upper terraces, replacing the Cl $c(2 \times 2)$ adlayer. Due to the very high mobility of the alloy phase, previous studies didn't succeed in obtaining high resolution images of the given phase. With our home-build high speed STM [56], allowing data recording at image acquisition rate up to 30 Hz, such observations become possible. Moreover, during the alloying process the formation of domains with two distinctive alloy phase structures was found. They both

correspond to a similar row-like pattern with different separation between Pb rows: $2a_{\text{Cu}}$ and $3a_{\text{Cu}}$ respectively, where $a_{\text{Cu}} = 2.55 \text{ \AA}$ is the copper nearest neighbor distance. The first structure is consistent with $c(4 \times 4)$ alloy phase and the second we regard as a transitional (4×3) structure, not reported yet in literature. Fast structural fluctuations within these phases occurring at millisecond regime by rearrangement of Pb rows or their parts were detected as well.

By reversible increasing the electrode potential, the Pb dissolution starts. It proceeds in three main stages. First, the partial dissolution of $c(4 \times 4)$ alloy phase occurs in the direction from the terrace to the step. As a result, a stable dilute $c(4 \times 4)$ alloy phase with supposed Pb coverage of 0.25 ML is formed. Further lead dissolution is combined with simultaneous adsorption of Cl ions from the electrolyte, which form $c(2 \times 2)$ domains. The Cl adlayer grows in an opposite direction—from the step to the terrace. The remaining lead agglomerates in stable ribbon-like structures, which were already reported [112, 119]. The high resolution STM images show that the Pb ribbon phase consists of two close-packed Pb atomic rows segregated at the boundary between anti-phase Cl $c(2 \times 2)$ domains. Based on these observations we suggest a new structural model for the Pb ribbon phase. In addition, the dynamics of ribbons during the final stage of Pb dissolution and attachment/detachment of single Pb adsorbates to ribbons were investigated.

5.5. Publication submitted to Physical Chemistry Chemical Physics.

Reproduced by permission of the PCCP Owner Societies. Copyright (2012) Owner Societies. The article is available via the internet at <http://pubs.rsc.org/en/content/articlelanding/2012/cp/c2cp41023k>.

**Studies of Electrochemical Surface Alloying and Dealloying
by *In Situ* High-Speed STM**

Andriy Taranovskyy, Sophie Guézo¹, Hisayoshi Matsushima², Yvonne Gründer³,

Olaf M. Magnussen *

*Institut für Experimentelle und Angewandte Physik, Christian-Albrechts-Universität zu Kiel,
24098 Kiel, Germany*

¹ Present address: Département Matériaux Nanosciences, Institut de Physique de Rennes, UMR UR1-CNRS 6251, Université de Rennes 1, F-35042 Rennes Cedex, France

² Present address: Interdisciplinary Graduate School of Medicine and Engineering, University of Yamanashi, Takeda 4-3-11, Kofu 400-8511 Japan

³ Present address: School of Chemistry, University of Manchester, Oxford Road, Manchester, UK M13 9PL

*Corresponding Author: Tel. + 49 431 880 5579, FAX + 49 431 880 1685, E-mail: magnussen@physik.uni-kiel.de

Abstract

The electrochemical formation and dissolution of a lead/copper surface alloy on Cu(100) in chloride-containing electrolyte solutions was studied on the atomic scale by *in situ* scanning tunneling microscopy with high temporal and spatial resolution. Alloy formation, induced by a negative potential sweep, starts predominantly at the Cu steps, followed by the formation of a novel transient (4×3) alloy phase with 0.25 ML Pb coverage, which continuously is transformed into the 0.375 ML coverage c(4×4) phase, observed under UHV conditions. Both of these phases consist of rows of Pb atoms embedded into the Cu surface and exhibit highly dynamic structural fluctuations on sub 100 ms time scales. Upon increasing the potential again, a second c(4×4) phase with a different appearance in the STM images forms, which is attributed to partial dealloying, involving desorption of Pb from energetically less favorable sites. Further dealloying results in the formation of ribbon-like structures, already reported in previous studies. These ribbons are shown to consist of Pb atoms decorating domain boundaries in the c(2×2) chloride adlayer, left behind on the Cu surface by the dissolving surface alloy phase. Furthermore, dynamic observations of the subsequent coarsening of the ribbon network and the attachment/detachment of isolated Pb adsorbates to the ribbons are presented. Both isolated Pb adsorbates and Pb atoms in the ribbons are proposed to be stabilized by coadsorbed Cl.

Keywords: binary alloy phase, surface dynamics, STM, cyclic voltammetry, solid-liquid interface, electrochemistry

I. Introduction

Growth of lead on copper has been intensively studied in the past, in both ultra-high vacuum (UHV)¹⁻⁸ and electrochemical environment.^{9,10} A distinct feature of the Pb/Cu system is that, despite a substantial lattice mismatch between lead and copper atoms (37%), and thus metal bulk immiscibility, 2D surface alloys can be observed at Pb coverages up to 0.375 monolayers (ML), in which lead atoms are incorporated into the Cu surface layer. Further Pb deposition leads to dealloying and the formation of overlayer structures. The formation of surface alloys in the intermediate coverage regime has been explained theoretically by the reduction of surface strains and thus the total surface energy for systems with large lattice mismatch.¹¹

Under UHV conditions, low energy electron diffraction (LEED)¹²⁻¹⁴ and scanning tunneling microscopy (STM) studies¹⁵⁻¹⁷ reported a variety of stable surface phases during the deposition of Pb on Cu(100) at room temperature. While at low coverages the Pb adsorbates are disordered, at higher coverages a $c(4\times 4)$ surface alloy with a nominal coverage of 0.375 ML is formed.² Upon further increasing the lead coverage dealloying commences, resulting first in a $c(2\times 2)$ overlayer phase with a coverage of 0.5 ML, followed by the insertion of antiphase boundaries that continuously transforms the overlayer phase into a $c(5\sqrt{2} \times \sqrt{2})R45$ phase with 0.6 ML coverage.¹⁸ The latter is the highest coverage phase for the Pb monolayer on Cu(100). Further Pb deposition occurs by a 3D island growth.

In electrochemical environment, Pb undepotential deposition (UPD) on Cu(100) is observed, where a range of surface phases is found, depending on the electrode potential. Both the $c(2\times 2)$ and the $c(5\sqrt{2} \times \sqrt{2})R45$ overlayer phase reconstructions and their phase transitions have been also observed by STM in 0.1M H_2SO_4 ¹⁷, 0.01 $HClO_4$ ¹⁰, and 1 mM $Pb(ClO_4)_2$ aqueous solutions in the UPD potential regime. The presence of Cl ions,⁹ which form a $c(2\times 2)$ adlayer on Cu(100) over a wide potential range, considerably influences the Pb surface phase behavior during deposition/dissolution. Specifically, the nanoscale surface structure exhibits a significant dependence on the sample history, where during the Pb dissolution narrow stripes form on the $c(2\times 2)$ -Cl covered surface. These Pb stripes

have been attributed to remaining parts of the $c(4\times 4)$ alloy phase, i.e., a Cu_4Pb_3 surface layer. However, no atomic resolution images of these stripes as well as of the Pb alloy phase in this electrolyte have been presented up to now, making this assignment somewhat speculative. The self-assembly of such stripe structures was explained by elastic interactions between stress domains of the anisotropic $c(4\times 4)$ Cu_4Pb_3 surface alloy phase separating domains of the isotropic $c(2\times 2)$ -Cl phase.¹⁹

Apart from the general interest in Pb/Cu(100) as a model system for surface alloying/dealloying, Pb acts as a surfactant for Cu growth.²⁰⁻²³ Via the Pb coverage and the associated surface structure the copper growth behavior can be controlled. Furthermore, Pb submonolayer deposits on the copper surface have a substantial influence on corrosion and electrocatalysis processes.^{24,25}

In this work we have studied the structure and dynamics of the surface phases in the Pb/Cu(100) UPD system in the presence of Cl coadsorbates on the surface, concentrating on the coverage range from the beginning of lead deposition to the formation of the $c(4\times 4)$ alloy phase. We present detailed atomic scale observations on the Pb alloying/dealloying processes obtained by video-STM. The high temporal and spatial resolution of this technique provides new insight into the structure and formation of the surface alloy phases, for which up to now no data have been reported in electrochemical environment, revealing the presence of the known $c(4\times 4)$ phase as well as novel transient phases. In addition, our high resolution STM images provide clearer structural data on the stripe network forming during Pb dissolution, disproving the previous assignment to a $c(4\times 4)$ alloy like structure.^{9,19}

II. Experimental details

Experiments were performed on Cu(100) single crystals (Mateck, $<0.1^\circ$ miscut) in aqueous solution containing $30\ \mu\text{M}\ \text{Pb}^{2+}$, $0.1\ \text{M}\ \text{HClO}_4$, and $2\ \text{mM}\ \text{NaCl}$. Prior to each experiment, the Cu(100) sample surface was prepared by electropolishing in orthophosphoric acid (66%) and then rinsed with ultrapure water.²⁶

Cyclic voltammograms (CV) were recorded in a three-electrode electrochemical cell in electrolyte deaerated for at least 30 minutes before and during voltammetry measurements, in order to reduce oxygen reduction. Similar voltammograms were obtained in the STM cell (not shown here), with similar positions of anodic and cathodic current peaks as in the dedicated cell. All potentials are reported versus a SCE reference electrode.

STM experiments were performed in an electrochemical cell at sample potentials in the range -0.24 to -0.47 V_{SCE} and at room temperature (290 K). Our home-built video-STM²⁷ allows *in situ* measurements in electrochemical environment with a rate of up to 30 images per second in constant-height mode. All STM images and videos presented in this study were obtained at an image acquisition rate of 10 Hz. Video-sequences with durations of 1 to 3 minutes were recorded, containing several hundred up to a few thousands images. Typically, tunneling currents of 9 to 23 nA and a bias of several hundred millivolts were used.

III. Results and Discussion

III.1 Electrochemical characterization

Prior to the video-STM studies, detailed electrochemical studies by cyclic voltammetry were performed. A characteristic series of cyclic voltammograms (CVs), recorded at 10 mV/s with the negative potential limit stepwise increased by 50 mV, is presented in Fig. 1. The characteristic features are in good agreement with those previously reported in the literature for this system.^{9,10,17,24} Underpotential deposition occurs in the potential range -0.45 to -0.30 V. In total, Pb deposition and dissolution in the UPD regime occurs in three steps, resulting in three partly overlapping peaks in the cathodic (I_c, II_c, and III_c) and anodic (I_a, II_a, and III_a) currents, respectively. In the sweeps covering the entire UPD range, the most positive peak only manifests as a shoulder (I_c/I_a) on peak II_c/II_a. For potential sweeps with negative limits ≤ -0.50 V an additional shoulder (IV_a) is found in the positive potential scan. This shoulder may be caused by the formation of Pb overlayer phases, which have been

reported to form in this potential regime.^{9,10,17} Pb bulk deposition starts at the Nernst potential of -0.55 V, but due to the low Pb concentration and corresponding low diffusion-limited currents could be detected in the CVs only at low scanning rates of 1 mV/s (not shown here). At potentials negative of -0.60 V, a pronounced increase in cathodic current due to hydrogen evolution can be observed (the vertical offset at potentials ≤ 0.40 V is due to residual oxygen reduction). The peak positions were found to depend only weakly on the potential sweep rate and shift by less than 15 mV in the range between 1 and 50 mV/s both for the cathodic and the anodic peaks. This observation differs from previous studies,^{10,28} where for Pb dissolution the potential shift with scan rate was reported to be less pronounced than that for deposition, which was attributed to a kinetic limitation of Pb growth.

The main pairs of peaks II_c/II_a and III_c/III_a were already reported in previous studies of Pb UPD on Cu(100) in Cl-containing electrolytes.^{9,10,17,28} Also the observed potential difference of 25 mV between peaks II_c and III_c is in good agreement with the literature. However, the shape of the cathodic wave differs from most previous observations, which may be a consequence of the 30 times lower Pb concentration in our experiments as compared to most of the CVs reported in the literature. A similar lead concentration (50 $\mu\text{M Pb}^{2+}$) was only used in the study by G.M. Brisard and coworkers,²⁸ where indeed also a double-peak structure in both potential scan directions can be discerned, confirming our results. Peaks II_c/II_a and III_c/III_a were attributed to different structural phases forming during Pb underpotential deposition and dissolution.^{9,10,17,28} Also the shoulders I_c/I_a were already observed previously and interpreted as structural changes related to a competition between lead dissolution/deposition and Cl adsorption/desorption.^{9,10} Due to its strong interaction with the copper surface, the chloride adlayer is expected to strongly affect surface structures for Pb deposition in the submonolayer regime.

As reported previously,⁹ some irreversibility exists between Pb underpotential deposition and dissolution, as indicated by the 45 mV potential shift between the main cathodic current peaks (II_c and III_c) and their anodic counterparts (II_a and III_a). A slightly larger shift of 80 mV was previously

reported by Moffat.⁹ In view of the rather weak dependence on the potential sweep rate (see above), this effect cannot be attributed to a slow deposition/dissolution kinetics, but suggests an energetic effect. The difference between the position of the bulk dissolution peak (-0.505 V at 1 mV/s scan rate) and the most negative surface alloy dissolution peak III_a (-0.34 V) is similar as in the CVs reported by Moffat. In view of the high sensitivity of CVs to the surface quality and sample preparation procedure we regard the agreement of our results with those of other groups as satisfactory.

III.2 Structural changes during Pb surface alloying

In the following section we first provide an overview on the *in situ* video-STM observations in the studied potential regime, describing the overall processes during Pb surface alloy formation in the UPD regime. Detailed data on the structure and dynamics of the various phases observed in this range will be given in section III.3.

In the absence of Pb²⁺ ions in the solution, the Cu(100) mono-crystal is covered in the corresponding potential regime by a c(2×2)-Cl adlayer.²⁹ This adlayer induces a strong faceting of the Cu surface, resulting in terraces separated by mono- and multilayer steps which are aligned in the <001> directions. This surface morphology is also observed in the presence of Pb²⁺ at potentials ≥ -0.30 V (Fig. 2a). Upon lead underpotential deposition (Fig. 2b-d), a new surface structure is observed, which spreads in both directions from the initial step position. Such an expansion of the terraces was also reported in previous studies by conventional *in situ* STM.⁹ It can be rationalized by the nucleation and growth of a Pb/Cu surface alloy, in which deposited Pb atoms penetrate the Cu surface layer at the steps, displacing Cu atoms in the near step region. These Cu atoms migrate on the neighboring lower terrace where they are incorporated into the growing surface alloy phase.

A detailed look on the dynamic processes during Pb deposition on a Cu(100) surface initially covered with a c(2×2)-Cl adlayer is provided by the sequence of high-resolution STM images in Fig. 3 (see also video file in Suppl. Inf.). Fig. 3a shows a c(2×2)-Cl reconstructed terrace with a step (right

side of image) oriented along the $\langle 001 \rangle$ direction, recorded at a potential of $-0.24 \text{ V}_{\text{SCE}}$ prior to Pb deposition. Subsequently, the potential was continuously changed to -0.47 V to initiate Pb surface alloying. In the initial stage of the deposition process the Cu step is decorated by a stripe-like deposit, which appears higher than the neighboring terrace (marked by arrow in Fig. 3b). This preferential was already observed in previous STM studies, both in UHV¹⁶ and in electrochemical environment.^{9,30} The stripe forms via stepwise extension of the upper terrace by a distance of about $5.0 \pm 0.3 \text{ \AA}$. As seen in Fig. 4, taken from a sequence where the growth of this stripe along the step was observed, the outmost row of the $c(2 \times 2)\text{-Cl}$ on the upper terrace disappears during stripe formation, i.e., the stripe extends to both sides of the original Cu step edge. This may be explained by a mechanism, in which Pb atoms are inserted in between the outmost row of Cu atoms and the remaining terrace, forming a 1D nucleus of the surface alloy. The most positive peak I_c in the negative potential sweep of the CV may be related to this initial adsorption along the steps.

At more negative potentials, the nucleation of a lead alloy phase takes place on the upper terrace along the Pb stripe decorating the step (Fig. 3c). Apart from the steps also defects on terraces such as domain boundaries (example marked by arrow in Fig. 2b) seem to be preferred nucleation sites. During the further potential sweep in the negative direction, the lead alloy phase growth from these nucleation sites onto the terraces, replacing the $c(2 \times 2)\text{-Cl}$ adlayer (Fig. 3d-f). Due to dynamic fluctuations in the surface alloy (see below), areas covered by this phase appear more fuzzy than the neighboring $c(2 \times 2)\text{-Cl}$ lattice in the video-STM images. However, contrary to previous *in situ* studies by conventional STM, where this surface alloy appeared completely disordered,^{9,17} clearly visible patterns, consisting of rows of higher apparent height (i.e., appearing bright in the images) oriented in $\langle 011 \rangle$ direction, can still be seen. Parallel to the growth of the alloy step faceting in $\langle 011 \rangle$ direction is observed. Furthermore, also the boundary between the growing alloy phase and the $c(2 \times 2)\text{-Cl}$ covered areas on the terraces also seems to be preferentially oriented along $\langle 011 \rangle$.

Although the formation of the lead alloy phase is fast, two separate alloy phases could be distinguished, differing by the distances between the characteristic rows, which are $2 \cdot a_{\text{Cu}}$ and $3 \cdot a_{\text{Cu}}$, respectively (with $a_{\text{Cu}} = 2.55 \text{ \AA}$ being the copper nearest neighbor distance). The first distance is in agreement with the $c(4 \times 4)$ alloy phase consisting of alternating chains of Pb and Cu atoms oriented in the $\langle 011 \rangle$ direction in the top surface layer (see Fig. 4f), which was reported previously in studies under UHV conditions¹⁶ and proposed already for the electrochemical system by Moffat on the basis of the observed Cu mass transport.⁹ The domains with the larger distance of $3 \cdot a_{\text{Cu}}$ between the rows are mainly observed in the initial stages of the alloying process and apparently correspond to a new transient phase, not yet reported in the literature. Based on the *in situ* STM observations, peak I_c in the voltammogram may correspond to the formation of Pb rows along the steps and the peaks II_c and III_c to the growth of the two surface alloy phases. The structure of these surface alloys as well as the dynamic fluctuations within these phases will be discussed in the next section.

III.3 Structure and dynamics of the surface alloy

More detailed structural data were obtained from atomic resolution video-STM sequences in the Pb UPD regime. As an example, four consecutively images from such a video, recorded during the initial stages of surface alloy formation, are shown in Fig. 5. In the right part of the images areas covered by the $c(2 \times 2)$ -Cl adlayer are visible, whereas a network of rows, characteristic of the alloy phases, is covering the left hand side of the imaged surface area. As clearly visible in those high-resolution STM images the rows consist of single atomic rows with a distance between the atoms in the row of $3.5 \pm 0.1 \text{ \AA}$, i.e., approximately $1.33 \cdot a_{\text{Cu}}$. This distance is consistent with the previous observations of the $c(4 \times 4)$ surface alloy phase,¹⁶ where along the row direction three Pb atoms occupy the four Cu surface lattice spacings a_{Cu} of the unit cell. We therefore also assign these structures to rows of Pb atoms embedded within the Cu surface layer. Due to the mismatch with respect to the Cu substrate lattice, the Pb atoms should occupy non-equivalent sites on the underlying metal substrate. For example, one of these Pb

atoms could be located on a bridge site of the second Cu layer and the two others on positions close to fourfold hollow sites (see models in Fig. 6b,d), as suggested for the c(4×4) phase.¹⁶ A difference in the apparent height of these atoms could not be observed, however, contrary to the UHV-STM observations of the c(4×4) phase.

The Pb rows exhibit a preferred spacing of $7.6 \pm 0.1 \text{ \AA}$ perpendicular to the row direction, corresponding to a distance of $3 \cdot a_{\text{Cu}}$ (see e.g. lower left corner in the images in Fig. 5). In contrast to the arrangement of these rows in the c(4×4) phase (Fig. 6d), where the Pb atoms in neighboring rows are anti-phase shifted relative to each other,³¹ our STM images suggest an alignment of these atoms. Based on these observations we suggest that this phase corresponds to a (4×3) superstructure with a lead coverage of 0.25 ML, as schematically illustrated in Fig. 6b. In this structure the Pb rows are separated by two rows of Cu atoms, rather than only one row as in the c(4×4) phase. The space between the Pb rows would be sufficiently large remains for the adsorption of other coadsorbates, such as Cl (see bottom right part of Fig. 6b). Indeed, we find additional, weaker maxima between the Pb rows in the STM images. However, the quality of these data is not sufficient for an unambiguous structural assignment of these features. The formation of a transient Cu/Pb surface alloy with a separation of $3 \cdot a_{\text{Cu}}$ between the Pb rows has not been reported up to now in studies under UHV conditions¹⁶ and in Cl-free electrolytes, suggesting that it is a genuine phase of the studied electrochemical system. Effects such as the coadsorption of Cl on the remaining double rows of Cu surface atoms discussed above could explain a stabilization of the (4×3) structure. Furthermore, also the location of this phase between the c(2×2)-Cl anion adlayer in the positive potential regime and the c(4×4) Pb/Cu surface alloy at more negative potentials could be rationalized by this.

Well-ordered domains of the (4×3) phase usually only have extensions of a few nanometers (see Fig. 6a). In addition to boundaries to other translational and 90° rotated domains also areas where the Pb rows have a less well defined lateral arrangement can be observed (see e.g. upper left corner of

Fig. 5). However, the 3.5 Å atomic spacing within the rows seems to be unaffected by this, indicating that these rows are the primary elements of the surface alloy.

Furthermore, this network of Pb rows is highly dynamic. As visible in the STM images in Fig. 5a-d the structures exhibit significant fluctuations on the time scale of 0.1 s, such as a shift of the Pb rows (or parts of those rows) in a direction perpendicular to their orientations by integer multiple of a_{Cu} (indicated in Fig. 5a-c by solid arrows, with the length equal to the magnitude of the corresponding shift), a growth or shrinking of Pb rows (dashed arrows in Fig. 5c), and a 90° rotation of small rows consisting of few Pb atoms (arched arrow in Fig. 5c). Despite these noticeable changes between the frames the Pb rows usually are clearly imaged in each individual frame, indicating that they are positionally stable on time scales required for imaging them (typically a few milliseconds). Thus, the characteristic time for the observed processes is in the range 5 to 100 ms.

In the further course of the surface alloying process the (4×3) structure is gradually transformed into the c(4×4) phase, in which the spacing of the Pb rows is reduced to $2 \cdot a_{\text{Cu}}$. Both surface alloy phases coexist over a wide range (see also Fig. 3) and have similar structural and dynamic properties. Specifically, also the fully developed c(4×4) phase (Fig. 6c) consists of small domains with a few nanometer in diameter and exhibits structural fluctuations on the same time scales as found for the (4×3) phase. This highly dynamic behavior explains why atomic-scale imaging of the Pb/Cu surface alloy had not been possible in previous *in situ* studies by conventional STM, which has a time resolution of the order of seconds to minutes. It furthermore shows clearly that the surface dynamics of the alloy formation in this system is fast and should hence not cause a significant kinetic barrier as also indicated by our electrochemical data.

III.4 Lead dealloying

Surface dealloying was initiated by increasing the potential from the regime of the c(4×4) alloy phase to more positive values. UPD at more negative potentials, were the Pb c(2×2) and

$c(5\sqrt{2}\times\sqrt{2})R45^\circ$ overlayer structure form,^{10,17} was already studied in detail previously by *in situ* STM and was not investigated in this work. The overall processes during the positive potential sweep are illustrated in Fig. 7 for a terrace close to a descending step (right side of images). Initially, the observed terrace is completely covered by the $c(4\times 4)$ alloy phase with a Pb coverage of 0.375 ML (Fig. 7a). Upon changing the potential in positive direction (Fig. 7b), a new surface phase emerges in the left hand side of the imaged area, which exhibits a characteristic square pattern that clearly differs from the ‘row-like’ pattern of the $c(4\times 4)$ structure. The close-packed directions in this pattern are oriented along the $\langle 001 \rangle$ direction with a nearest neighbor spacing of $7.1 \pm 0.2 \text{ \AA}$, corresponding to $2\sqrt{2}\cdot a_{\text{Cu}}$. The boundary to the original $c(4\times 4)$ phase (marked by dashed white line in Fig. 7b) in contrast is preferentially oriented parallel to the Pb rows, i.e., along the $\langle 011 \rangle$ directions of the substrate lattice.

We assign this new phase tentatively to a $c(4\times 4)$ surface alloy with lower Pb coverage, resulting from partial lead desorption, and will term it in the following as diluted $c(4\times 4)$ alloy. The STM data could be rationalized by a $c(4\times 4)$ structure (unit cell indicated in Fig. 6e,f) in which every third Pb atom of the original $c(4\times 4)$ phase (Fig. 6d) has been desorbed, resulting in a decrease in Pb coverage from 0.375 to 0.25 ML. This partial desorption may be explained by energetic effects, since every third Pb atom in the rows of the $c(4\times 4)$ alloy occupies a bridge site of the underlying second Cu layer, whereas the remaining atoms reside in sites close to fourfold hollow sites.¹⁶ It is currently not entirely clear whether the sites of the desorbed Pb atoms remain empty, as shown in the model in Fig. 6f, or are re-occupied by additional Cu surface atoms.

In the course of Pb dissolution the diluted $c(4\times 4)$ alloy phase propagates from the terrace towards the step, replacing the initial $c(4\times 4)$ structure (Fig. 7c). Subsequently, a second phase transition commences where the surface alloy is replaced by domains of the $c(2\times 2)$ chloride adlayer (Fig. 7d-f). The latter nucleate at the step from where they grow onto the neighboring terrace. Simultaneously we observe the formation of the ribbon-like structures with orientations along the $\langle 001 \rangle$ directions already reported in previous STM studies.^{9,10} This two-step dissolution process may cause the peaks II_a and III_a

observed in the positive potential sweep of the voltammogram, whereas the shoulder I_a may be linked to the dissolution of Pb stripes at boundaries between $c(2\times 2)$ -Cl domains and steps.

III.5 Pb ribbon phase

The formation of anisotropic ribbon-like structures during the desorption of UPD lead was already observed in previous *in situ* STM studies in Cl-containing electrolyte.^{9,19} In these studies the ribbons were interpreted as remnants of the $c(4\times 4)$ Pb surface alloy phase, although no high-resolution STM images could be obtained that allowed direct confirmation of this assignment – probably due to the rather dynamic behavior of these structures. Our video-STM observations suggest a different structure of these ribbons. As visible in the atomic-resolution image in Fig. 8a, the $c(2\times 2)$ -Cl adlattices on both sides of the ribbon are anti-phase shifted relative to each other, indicating clearly that the ribbon corresponds to a translational domain boundary. This effect readily explains why the ribbons form closed loops (see also Fig. 9 and video 1 in the supporting information) or end at steps. The distance between the closest Cl rows running parallel on both sides of the boundary is $9.0 \pm 0.1 \text{ \AA}$ which is equal to $2.5 \cdot \sqrt{2} \cdot a_{\text{Cu}}$. The ribbon itself consists of two atomic rows in a zigzag arrangement, which we assign to remaining Pb adatoms. Depending on the imaging conditions these central rows appear as protrusions (Fig. 8a) or depressions (see Fig. 10). The atomic spacings along the Pb rows are identical to those in the $c(2\times 2)$ lattice, i.e., $\sqrt{2} \cdot a_{\text{Cu}}$, leading to a well-defined phase relationship between the Pb atoms in the rows and the Cl adsorbates in the neighboring adlayer domains with a shift along the ribbon direction in the range 0.4 to 0.9 \AA . The measured distance between the two lead rows is $2.8 \pm 0.2 \text{ \AA}$. Consequently, the shortest distance between the atoms in the rows is about $3.4 \pm 0.2 \text{ \AA}$, which is close to the lead atomic diameter. Similar but less clear STM images were also obtained by Kukta et al.¹⁹

These data are inconsistent with a structure, in which the ribbons consist of thin segments of the $c(4\times 4)$ Pb surface alloy phase. In particular, the distances between the Pb atoms along the ribbon

direction (i.e., in $\langle 001 \rangle$ direction) would be $2\sqrt{2} \cdot a_{\text{Cu}}$ for that type of atomic arrangement, which is twice of the experimentally observed Pb spacing. We therefore suggest an atomic-scale structure of the ribbons, where the $c(2 \times 2)$ -Cl domain boundary is decorated by a zigzag chain of densely packed Pb atoms. However, it is unclear whether these Pb atoms are situated on top of Cu substrate (Fig. 8b) or embedded in a narrow groove in the Cu surface layer (Fig. 8c). In both cases the structural data of the STM observations could be reproduced by placing the Pb atoms in positions close to four-fold hollow sites of the underlying Cu layer. The larger atomic diameter of Pb as compared to Cu enforces a lateral displacement in $\langle 011 \rangle$ direction from these sites (indicated by arrows), leading to the observed slight phase shift relative to the neighboring $c(2 \times 2)$ -Cl lattice. This structure resembles the local arrangement of Pb in the $c(5\sqrt{2} \times \sqrt{2})R45$ overlayer, in which alternating heavy domain walls are inserted into the $c(2 \times 2)$ lattice of the Pb overlayer.¹⁴

In principle, it should be possible to distinguish between the two models on the basis of the Cu surface mass transport required for recovering the (defect-free) Cu surface: in the case of embedded Pb two additional Cu atoms would have to be reinserted per Pb atom into the copper surface during the dissolution of the ribbons. Unfortunately, the STM observations did not allow conclusively determining whether this type of mass transport occurs, since the expected changes are rather small and the steps undergo substantial rearrangement due to faceting along the $\langle 001 \rangle$ directions. Indirect support for the first model (Fig. 8b), where the ribbons consist of Pb adatoms on the Cu surface layer, comes from comparison with isolated Pb adsorbates, which have a very similar appearance in the STM images (see below).

As noted before, the ribbons self-assemble in networks with rather well-defined distances,^{9,19} with the minimal number of Cl rows between stable Pb ribbons being equal to two. The anisotropy of the ribbon loops was attributed by Moffat to two different stripe structures and consequently different line energies for the two $\langle 001 \rangle$ orientations.⁹ Our data do not support such an intrinsic structural anisotropy of the ribbons. As seen in the models and also supported by the atomic resolution images, the two

possible orientations do not show any differences in the structural properties of the ribbons along the two directions and therefore should be equivalent. Kukta et al. proposed attractive elastic interactions between the ribbons, caused by an anisotropy of the surface stress within the ribbons.¹⁹ Although the ribbons in the models in Fig. 8 do not exhibit the directional anisotropy assumed in Ref. (19), the basic principle of this explanation will hold independent of the concrete atomic structure of the ribbons. For the arrangement suggested in our models the stress associated with the displacements of the Pb atoms in the directions indicated by the white arrows should be different from that for displacements in opposite or perpendicular direction, which may be sufficient to explain the observed ribbon attraction.

As visible in the video sequences (see Fig. 7 and video 2 in the supporting information) nucleation and growth of the Pb ribbons proceeds at the boundary between the diluted $c(4\times 4)$ Pb alloy phase and the $c(2\times 2)$ -Cl covered Cu surface. Specifically, ribbon formation seems to occur predominantly at $\langle 001 \rangle$ -oriented segments of this boundary. Indeed, the Pb arrangement in the ribbons resembles that of a row of Pb dimers along the $\langle 001 \rangle$ direction in the diluted $c(4\times 4)$ alloy phase (see Fig. 6f) and could be formed by a short-range local rearrangement within such a row. In addition, ribbons are often found to form directly along the edge of $\langle 001 \rangle$ oriented Cu steps (see e.g. Fig. 7d). Since the transition from the Pb alloy to the $c(2\times 2)$ -Cl starts preferentially at the Cu steps, this is not surprising. After the initial formation of a single Pb ribbon at the edge of a $c(4\times 4)$ Pb alloy domain, further shrinking of that domain due to ongoing dealloying causes a detachment of the ribbon, resulting in the formation of a new $c(2\times 2)$ -Cl domain in the surface area between alloy and ribbon. Size fluctuations of this newly formed $c(2\times 2)$ -Cl area can either lead to reattachment of the alloy to the Pb ribbon and even annihilation of the latter or to the formation of a second parallel ribbon that can connect with the first one, leading to the formation of a closed loop. Also the formation of U-shaped ribbons, where the surface alloy domain terminates one of the short edges of the ribbon loop was observed. In this case the shrinking of the alloy domain results in elongation of the loop in one direction, creating the strongly anisotropic structures also found in previous studies.^{9,10,19} A related effect can be seen in Fig. 9a,b,

where two U-shaped half ribbon loops, attached to the same $c(4\times 4)$ Pb alloy domain (marked by black arrow in the first image of Fig. 9), interconnect after complete dissolution of the surface alloy.

The surface migration of the Pb ribbons during the final stages of lead dissolution and the associated ripening of the $c(2\times 2)$ -Cl domains is illustrated by the subsequent images in the sequence presented in Fig. 9. Here, the total ribbon length decreases with time, leading to a shrinking of the loops and a coarsening of the original labyrinthine polygonal $c(2\times 2)$ -Cl domain structure. This process proceeds predominantly via motion of the short side of the loops (examples marked by white arrows in Fig. 9), whereas the longer sections largely maintain their lateral positions. In the initial stages, where the surface is covered by a network of narrow loops, the individual segments of the Pb ribbons remain straight and oriented in $\langle 001 \rangle$ direction, even on the 0.1 s time scale of the STM image acquisition. However, in the final stages of this process, when most Pb is dissolved and only a few isolated Pb ribbons exist on the surface (Fig. 9h), the ribbons deviate from these preferred directions. In this case the ribbon exhibits rapid lateral fluctuations, as also apparent from the frizzy appearance in the image. The latter suggests a mobility of the ribbons on the millisecond time scales. Since the structural arrangement shown in Fig.8b is only possible for Pb ribbons in $\langle 001 \rangle$ direction, ribbons along other directions should be less stable, as verified by these observations. Most probably, the density of Pb atoms is significantly lower in these parts of the ribbon allowing a higher mobility of these atoms along the $c(2\times 2)$ -Cl domain boundary as well as of the boundary itself. A similar behavior was found for sulfur adsorbates in domain boundaries of the Cl adlayer on Cu(100).³² The higher mobility of the ribbons in the final stage of the Pb dissolution the domain ripening process accelerates and the domain boundaries annihilate quite fast at the steps (see e.g. end of video 2). Vice versa, the presence of substantial amounts of lead adsorbed on the surface considerably blocks the ripening of $c(2\times 2)$ -Cl domains.

III.6 Isolated Pb adsorbates

It has been already noticed^{9,19} that after the complete dissolution of the lead phase a substantial amount of point defects are found on the surface (with a coverage up to 0.1 ML), which were attributed to remaining individual Pb adsorbates. In a recent publication we reported quantitative data on the tracer diffusion and lateral interactions between lead adsorbates.³³ This study revealed hopping diffusion of the adsorbates between neighboring sites of the $c(2\times 2)$ lattice. The diffusion barrier changed linearly with potential with a slope of 0.5 eV/V, similar as found also for anionic sulphur adsorbates³⁴ – an effect attributed to a dominant influence of the Cl coadsorbates on the potential dependence of the diffusion barrier. To explain this phenomenon we proposed that during a Pb jump to a neighboring $c(2\times 2)$ lattice site the surrounding Cl adlayer is strongly deformed, leading to a pronounced contribution to the total change in dipole moment during the hopping process. The latter determines electrostatic contribution to the diffusion barrier, caused by the interaction of the dipole moment with the (potential dependent) electric field of the double layer. In addition, attractive interactions between lead adsorbates of magnitude 15 to 25 meV were found in this study for nearest and next-nearest Pb neighbors within the $c(2\times 2)$ -Cl matrix.

In STM studies of low coverages of Pb on clean Cu(100) surfaces under UHV conditions it was suggested that isolated Pb atoms do not occupy sites on top of the surface, but replace one of the Cu surface atoms.^{5,16} In view of the tendency towards surface alloying in the UPD regime, this adsorption geometry could in principle also be conceivable in electrochemical environment. However, for the studied system it can be excluded by simple symmetry considerations. As illustrated in the model in Fig. 8c (upper right corner), the Pb atom in this case would have to replace in two neighboring Cl adsorbates on the $c(2\times 2)$ -Cl covered surface. This would result in two symmetrically equivalent, but 90° rotated positions for the Pb adsorbate. As a consequence, Pb diffusion should occur via motion between neighboring sites of the Cu(100) surface, i.e., on a (1×1) lattice, with the shape of the adsorbates alternating between the two orientations at each individual jump. This behavior was never

observed in the STM videos, rather all adsorbates always exhibit the same (tip-dependent) shape and move on the $c(2\times 2)$ lattice. Similar arguments hold for geometries where the Pb adsorbate replaces two or three Cu surface atoms. Adsorption in $c(2\times 2)$ lattice sites on top of the Cu surface layer therefore seems to be the most probable alternative.

Why – contrary to the clean Cu surface – Pb adsorbates in this system are more stable in on top sites than in embedded sites may be potentially explained by characteristic properties of the electrochemical phase boundary: The isolated Pb species are observed at potentials clearly positive of the UPD peak in the voltammogram (up to -0.13 V), where a more cationic nature of these adsorbates is expected, and reside on a surface covered by a Cl adlayer, which has been shown to be clearly anionic in nature.³⁵ Stabilization of (partially positively charged) Pb adsorbates by electrostatic interactions with surrounding anionic coadsorbates is therefore highly conceivable and should be particularly strong for isolated Pb with Cl coadsorbates on all four neighboring sites. This type of anion-induced metal stabilization in the UPD regime has been supported by *ab initio* theory calculations³⁶ and may even lead to the formation of ionic salt-like adlayer phases in the intermediate potential regime between pure metallic UPD phases and purely anionic adlayers (see Ref. (37) and references cited therein). It could also explain the rather weak pairwise interactions between the isolated Pb species and why they do not form larger clusters or islands as expected for metal atoms. Since in that case the number of Cl neighbors on the surface would be reduced, energetically unfavorable weaker binding of the Pb adsorbates to the surface would result.

At potentials slightly positive of the Pb UPD range the isolated Pb adsorbates coexist and interact with the Pb ribbons. A sequence of subsequent images from a video recorded in this potential range is shown in Fig. 10. In this video both the Pb adsorbates and the Pb ribbons appear as depressions of similar depth (the small maxima correspond to contaminations, probably small amounts of adsorbed sulfur atoms, of much lower surface mobility), although the image contrast depends in detail on the tip state and imaging conditions. In other STM experiments both type of species were imaged as

protrusions (see Fig. 8,9 and Ref. (33), respectively), with changes in imaging occurring sometimes within a single video. However, the appearance of the adsorbates and the ribbons in the same STM image was always very similar, suggesting already a close relationship between the adsorbates and the ribbons. This is supported by the time-resolved observations, which show dynamic exchange of single Pb adsorbates with Pb in the ribbons. As an example, in Fig. 10 the motion of a single Pb adsorbate (marked by arrow in Fig. 10a) to the ribbon and its subsequent attachment to the corner of the ribbon is observed. Also the reverse process was found, where an isolated adsorbate was formed by separation from a ribbon.

These observations suggest that the state of the isolated Pb species and the Pb in the ribbons is very similar. Based on our previous assignment of the isolated Pb to adatoms, the Pb atoms in the ribbons should reside on top of the Cu surface as well, as shown in Fig. 8b. As visible in this model, also the latter Pb atoms have two Cl coadsorbates as direct neighbors, which could result in a similar electrostatic stabilization of Pb on the surface (see discussion above). Due to the lower number of counterion coadsorbates per Pb atom this effect should be weaker than for isolated Pb within the $c(2\times 2)$ -Cl phase, which could explain why the ribbons dissolve at potentials where isolated Pb adsorbates are still stable on the surface.

IV. Conclusion

Our *in situ* high-speed STM study of Pb surface alloying and dealloying on Cu(100) in Cl-containing electrolyte provide novel insight into the atomic-scale structure and dynamics of these phase formation processes. These measurements not only confirm the formation of the $c(4\times 4)$ Pb alloy phase with 0.375 ML Pb coverage, known from studies under UHV conditions,^{2,5,15,38} but also reveal new phases not reported previously. Specifically, we observe a transient (4×3) phase in the initial stages of Pb underpotential deposition and a modified “diluted” $c(4\times 4)$ Pb alloy phase during Pb dissolution. The (4×3) phase is structurally related to the known $c(4\times 4)$ alloy, with both consisting essentially of close-

packed rows of Pb atoms inserted in missing rows within the Cu surface layer. Both of these structures coexist on the surface and exhibit a similar highly dynamic behavior, where rows change lateral position and orientation on sub 100 ms time scales. The latter probably accounts for the inability of previous studies by conventional *in situ* STM to obtain high-resolution images of the surface alloy. The appearance of the diluted c(4×4) Pb alloy was assigned to partial Pb desorption from the known c(4×4) phase during dealloying.

In addition, the high-resolution STM images presented here shed new light on the origin of the well-known ribbons, formed after Pb dealloying in this system. Our observations unambiguously show that these ribbons correspond to Pb decorated anti-phase boundaries in the c(2×2)-Cl adlayer, rather than remnants of the surface alloy. These ribbons form at the boundaries between c(2×2)-Cl areas and domains of the diluted c(4×4) Pb alloy and subsequently ripen. Furthermore, the exchange of isolated Pb adsorbates on the c(2×2)-Cl covered surface with Pb atoms within the ribbons was observed, supporting that the ribbons are formed by Pb atoms on top of the Cu surface.

Together with the previous *in situ* STM observations our data indicate a complex sequence of potential-dependent adlayer phases in the UPD potential regime of this system, which can be rationalized by the (potential-dependent) mutual interactions of Pb adsorbates, Cl coadsorbates, and Cu surface atoms. According to the scenario proposed here, starting with simple metallic overlayers at the onset of bulk deposition, with increasing potential first the c(4×4) surface alloy known from UHV-STM studies, a partially dealloyed c(4×4) phase, a network of Pb-decorated c(2×2)-Cl domain boundaries, which can be considered as a Pb/Cl coadsorbate structure, and finally isolated, Cl-stabilized Pb adsorbates are formed on the Cu electrode surface. Many of these phases exhibit dynamic structural fluctuations on the sub-second scale. The high mobility in these surface phases explains the rather fast kinetics of the UPD, despite these pronounced restructuring processes, and may be of relevance for their action as surfactants in metal growth.

Acknowledgments

We acknowledge financial support by the Deutsche Forschungsgemeinschaft via MA 1618/15.

Supporting information

In situ STM video sequences of Cu(100) in 0.1 M HClO₄ solution, containing 30 μM Pb²⁺ and 2 mM NaCl, showing the Pb alloying and dealloying during potential cycles.

References

- (1) Cohen C. *Eur. Phys. Lett.* **1993**, *24*, 767-772.
- (2) Gauthier, Y.; Moritz W.; Hösler W. *Surf. Sci.* **1996**, *345*, 53-63.
- (3) Li W.; Vidali G.; Biham O. *Phys. Rev. B* **1993**, *48*, 8336-8344.
- (4) Robert S.; Cohen C.; L'Hoir A.; Moulin J.; Schmaus D.; Barthes-Labrousse M. G. *Surf. Sci.* **1996**, *365*, 285-296.
- (5) Robert S.; Gauthier S.; Bocquet F.; Rousset S.; Duvault J. L.; Klein J. *Surf. Sci.* **1996**, *350*, 136-144.
- (6) Sánchez A.; Ferrer S. *Phys. Rev. B* **1989**, *39*, 5778-5786.
- (7) Sanchez A.; Ibanez J.; Miranda R.; Ferrer S. *J. Appl. Phys.* **1987**, *61*, 1239-1241.
- (8) Sánchez A.; Ibañez J.; Miranda R.; Ferrer S. *Surf. Sci.* **1986**, *178*, 917-926.
- (9) Moffat T. P. *J. Phys. Chem. B* **1998**, *102*, 10020-10026.
- (10) Vasiljevic N. Ph.D. Thesis, Arizona State University, **2004**.
- (11) Tersoff J. *Phys. Rev. Lett.* **1995**, *74*, 434-437.
- (12) Henrion J.; Rhead G. E. *Surf. Sci.* **1972**, *29*, 20-36.
- (13) Hösler W.; Moritz W. *Surf. Sci.* **1982**, *117*, 196-203.
- (14) Hösler W.; Moritz W. *Surf. Sci.* **1986**, *175*, 63-77.
- (15) Nagl C.; Haller O.; Platzgummer E.; Schmid M.; Varga P. *Surf. Sci.* **1994**, *321*, 237-248.
- (16) Nagl C.; Platzgummer E.; Haller O.; Schmid M.; Varga P. *Surf. Sci.* **1995**, *331*, 831-837.
- (17) Wu H.-C.; Yau S.-L. *J. Phys. Chem. B* **2001**, *105*, 6965-6971.
- (18) Kellogg G. L.; Plass R. *Surf. Sci.* **2000**, *465*, L777-L782.
- (19) Kukta R. V.; Vasiljevic N.; Dimitrov N.; Sieradzki K. *Phys. Rev. Lett.* **2005**, *95*, 186103.
- (20) Müller S.; Prieto J. E.; Krämer T.; Rath C.; Hammer L.; Miranda R.; Heinz K. *J. Phys.: Condens. Matter* **2001**, *13*, 9897-9911.
- (21) Camarero J.; Spendeler L.; Schmidt G.; Heinz K.; Miguel J. J.; Miranda R. *Phys. Rev. Lett.* **1994**, *73*, 2448-2451.

- (22) Egelhoff J. W. F.; Chen P. J.; Powell C. J.; Stiles M. D.; McMichael R. D., *J. Appl. Phys.* **1996**, *79*, 2491-2496.
- (23) Passeggi, M. C. G. Jr.; Prieto J. E.; Miranda R.; Gallego J. M. *Phys. Rev. B* **2001**, *65*, 035409.
- (24) Kokkinidis G.; Jannakoudakis D. *J. Electroanal. Chem.* **1984**, *162*, 163-173.
- (25) Vasilic R.; Vasiljevic N.; Dimitrov N. *J. Electroanal. Chem.* **2005**, *580*, 203-212.
- (26) Vogt M. R.; Möller F. A.; Schilz C. M.; Magnussen O. M.; Behm R. J. *Surf. Sci.* **1996**, *367*, L33-L41.
- (27) Zitzler L.; Gleich B.; Magnussen O. M.; Behm R. J.; *Proc. Electrochem. Soc.* **2000**, 99-28, 29.
- (28) Brisard G. M.; Zenati E.; Gasteiger H. A.; Marković N. M.; Ross P. N., *Langmuir* **1997**, *13*, 2390-2397.
- (29) Vogt M. R.; Lachenwitzer A.; Magnussen O. M.; Behm R. J. *Surf. Sci.* **1998**, *399*, 49-69.
- (30) Van Gastel R.; Somfai E.; Van Albada S. B.; Van Saarloos W.; Frenken J. W. M. *Surf. Sci.* **2002**, *521*, 10-25.
- (31) Sepulveda A.; Rhead G. E. *Surf. Sci.* **1977**, *66*, 436-448.
- (32) Tansel T.; Taranovskyy A.; Magnussen O. M. *ChemPhysChem* **2010**, *11*, 1438-1445.
- (33) Guézo S.; Taranovskyy A.; Matsushima H.; Magnussen O. M. *J. Phys. Chem. C* **2011**, *115*, 19336-19342.
- (34) Tansel T.; Magnussen O. M. *Phys. Rev. Lett.* **2006**, *96*, 026101.
- (35) Saracino M.; Broekmann P.; Gentz K.; Becker M.; Keller H.; Janetzko F.; Bredow T.; Wandelt K.; Dosch H. *Phys. Rev. B* **2009**, *79*, 115448.
- (36) Sánchez C.; Leiva E. P. M. *Electrochim. Acta* **1999**, *45*, 691-697.
- (37) Magnussen O. M. *Chem. Rev.* **2002**, *102*, 679-726.
- (38) Robert S.; Gauthier S.; Bocquet F.; Rousset S.; Duvault J. L.; Klein J. *Surf. Sci.* **1996**, *350*, 136-144.

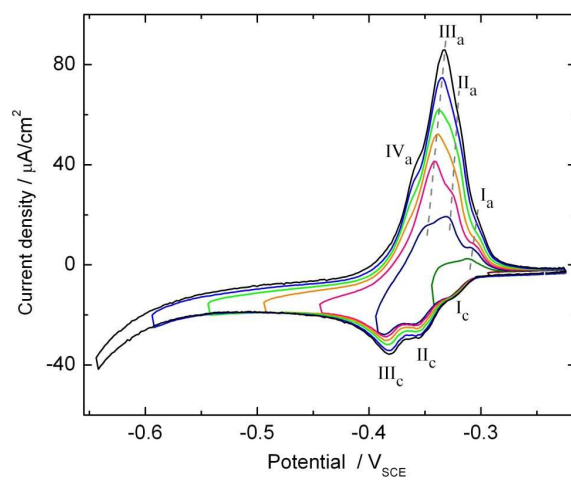


Fig. 1: Cyclic voltammograms of Cu(100) in 0.1 M HClO_4 containing $30 \mu\text{M Pb}^{2+}$ and 2mM NaCl (potential sweep rate 10 mV/s), obtained by decreasing the negative potential limit by 50 mV steps.

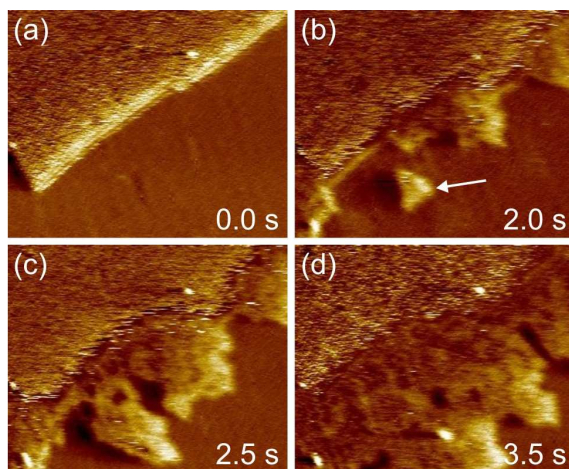


Fig. 2: Selected images ($22 \times 18 \text{ nm}^2$) from a video-STM sequence, recorded during a potential decrease from -0.31 to $-0.38 \text{ V}_{\text{SCE}}$. The series shows the formation of the Pb/Cu surface alloy during Pb underpotential deposition on a Cu(100) electrode surface, covered with a $c(2 \times 2)\text{-Cl}$ adlayer.

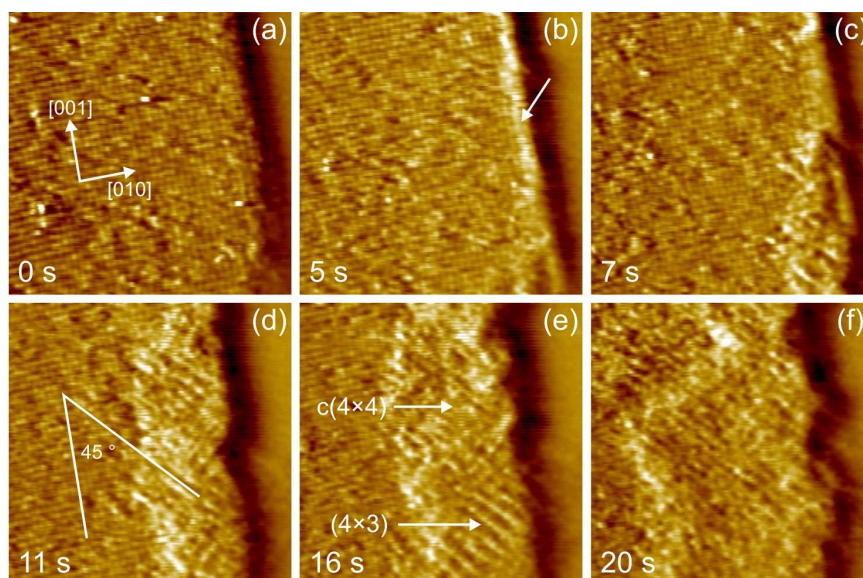


Fig. 3: Selected STM images ($15 \times 15 \text{ nm}^2$) from a video showing the Pb surface alloying process on Cu(100) during a continuous change in the electrode potential from (a) -0.24 to (f) $-0.47 \text{ V}_{\text{SCE}}$. Starting from (a) a surface covered by the square lattice of the $c(2 \times 2)$ -Cl adlayer, (b) Cu step decoration by deposited Pb (indicated by arrow), (c) Pb alloy nucleation, and (d) – (f) growth of the Pb alloy phase is observed. Examples of domains of the $c(4 \times 4)$ and the metastable (4×3) phase areas, showing the characteristic row-like patterns, are marked in (e).

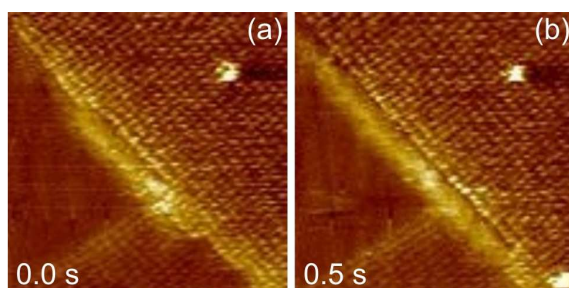


Fig. 4: Selected high-resolution video-STM images ($12 \times 12 \text{ nm}^2$) at -0.34 V , illustrating the decoration of the step to the upper terrace.

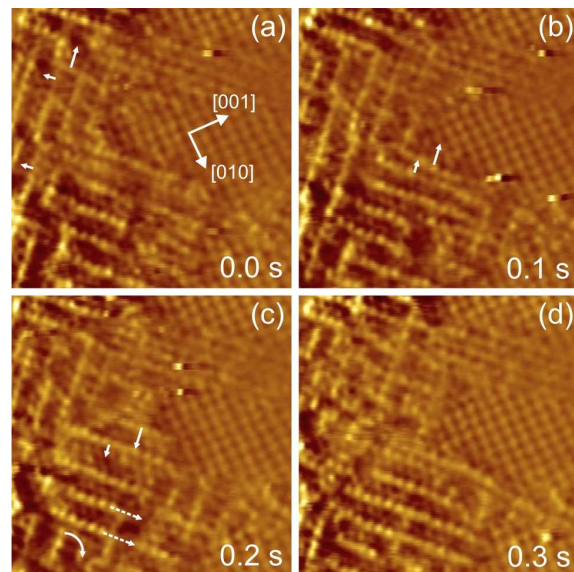


Fig. 5: Series of 4 subsequently recorded images ($8.5 \times 8.5 \text{ nm}^2$) from a video-STM sequence, showing the structure and dynamics of the (4×3) phase in the initial stages of alloy formation. In the right part of the images the square lattice of the $c(2 \times 2)$ -Cl adlayer is visible. Solid, dashed, and arched arrows indicate different types of dynamic fluctuations in the arrangement of the Pb rows (see text).

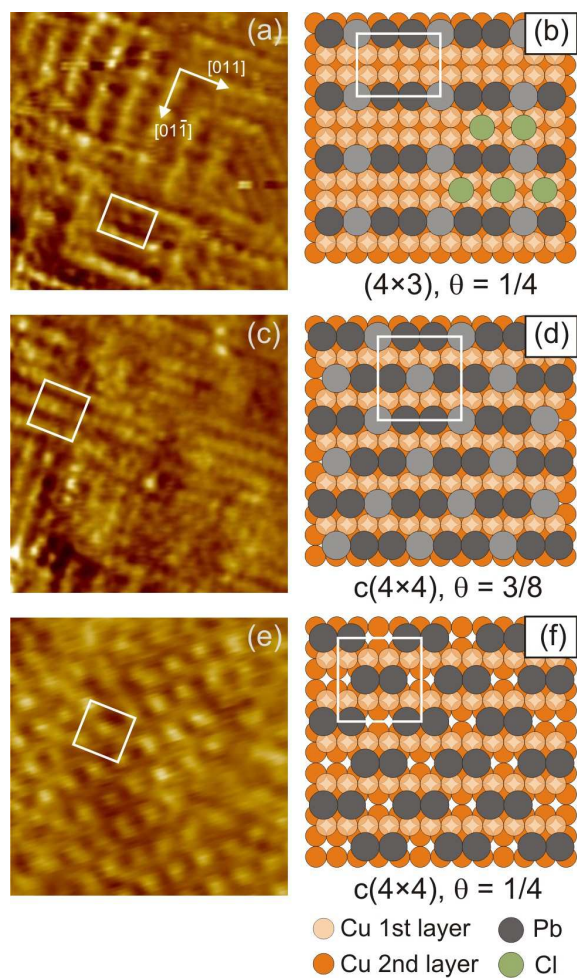


Fig. 6: Characteristic STM images ($6.5 \times 6.5 \text{ nm}^2$) and schematic structural models of (a,b) the (4×3) , (c,d) the $c(4 \times 4)$ surface alloy phase, and (e,f) the diluted $c(4 \times 4)$ surface alloy observed during dealloying. White rectangles indicate the unit cell of these superstructures.

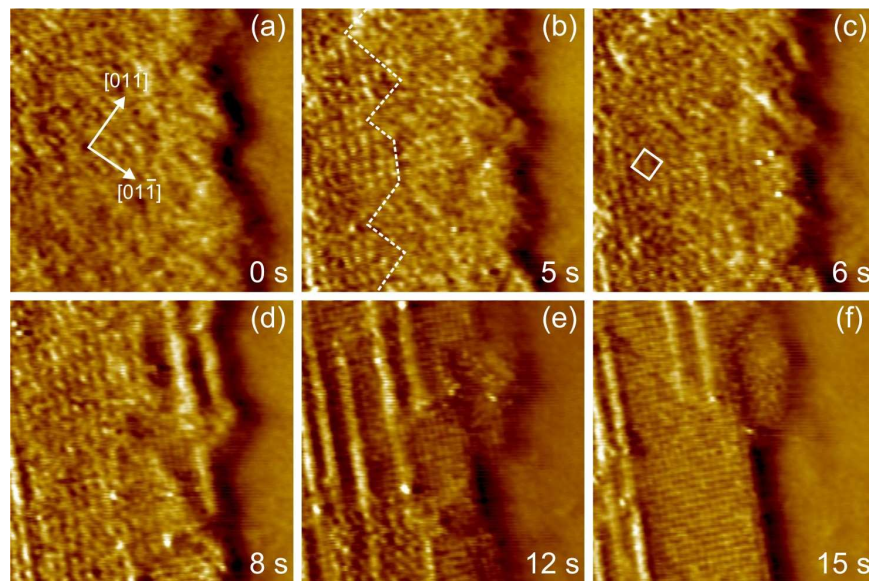


Fig. 7: Selected images from a video sequence ($15 \times 15 \text{ nm}^2$) showing the Pb dealloying process during a potential increases from -0.47 to -0.24 V . (a) Initial $c(4 \times 4)$ alloy phase, covering the observed terrace, (b) appearance of the diluted $c(4 \times 4)$ alloy phase, (c) surface covered completely by the diluted $c(4 \times 4)$ alloy phase, (d-f) slow replacement of the dilute $c(4 \times 4)$ alloy phase by the $c(2 \times 2)$ -Cl adlayer and appearance of the stripe network.

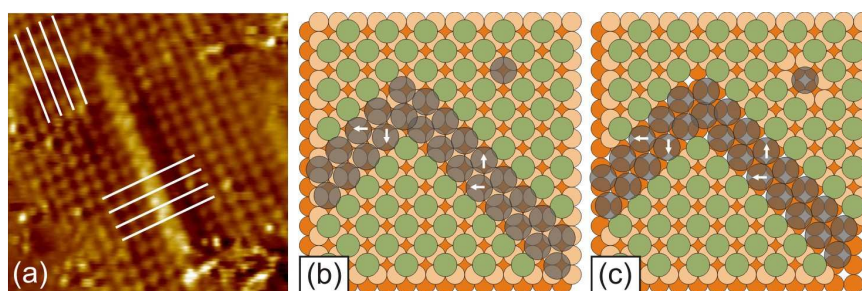


Fig. 8: (a) Atomic-resolution video-STM image ($8.5 \times 8.5 \text{ nm}^2$) of a ribbon, formed by surface dealloying during an increase of the potential from -0.52 to -0.32 V . As visible by extrapolating the Cl adlattice across the ribbon (white lines) the ribbon corresponds to a decorated domain boundary in the $c(2 \times 2)$ -Cl adlayer. (b,c) Two schematic models of the atomic arrangement of Cl (green) and Pb (gray) in the ribbon.

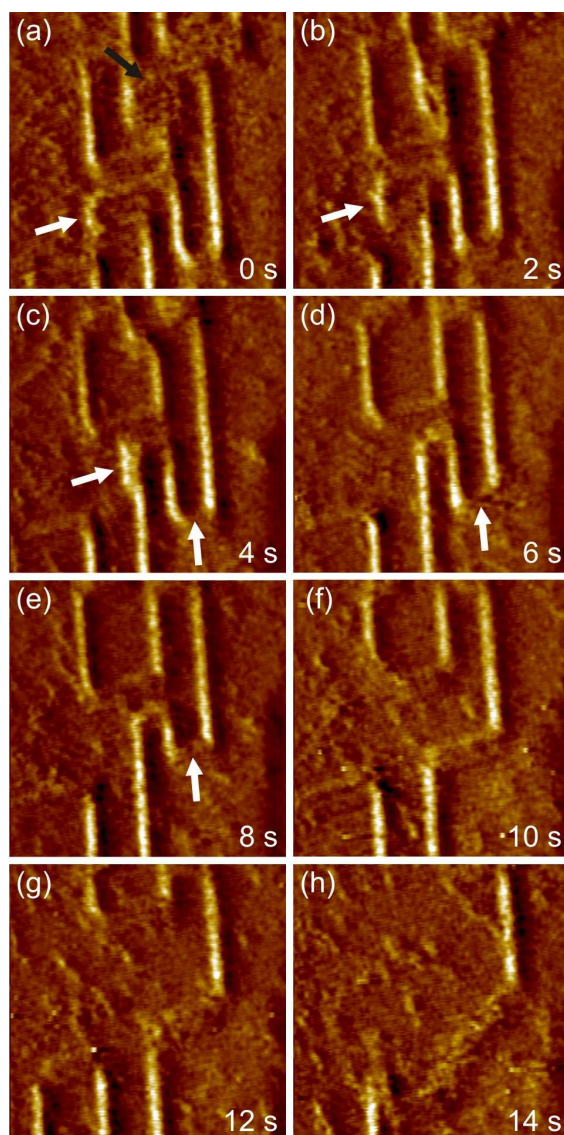


Fig. 9: Series of video-STM images ($13 \times 13 \text{ nm}^2$) illustrating the Pb ribbon dynamics at -0.26 V during the final stage of lead dissolution and ripening of the $c(2 \times 2)$ -Cl domains.

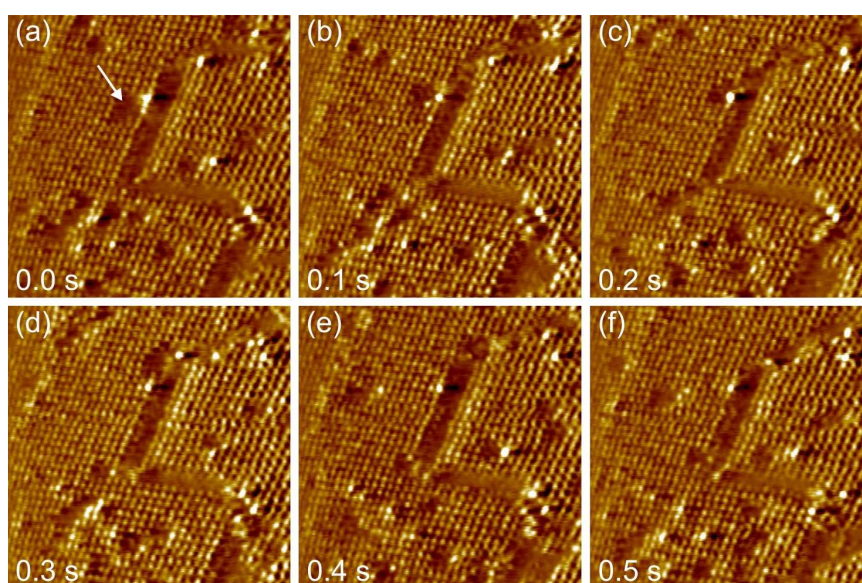


Fig. 10: Series of subsequently recorded images from a video-STM sequence at -0.33 V (12×12 nm²), showing attachment of a Pb adsorbate (white arrow) to a Pb ribbon.

6. Summary

In the present work, surface dynamic processes such as adsorbate tracer diffusion, adsorbate-adsorbate interactions, and surface phase transitions were investigated at the solid-liquid interface by *in situ* high speed STM and further quantitative analysis in the selected system consisting of Cu(100) single crystal electrode immersed in the aqueous solution of 0.01 M HCl. As studied adsorbates, in various experiments two species with different chemical nature, namely S_{ad} and Pb_{ad}, were chosen. The obtained results showed a similar potential dependency of the diffusion barriers for both species, indicating on the decisive influence of Cl c(2 × 2) adlayer on adsorbate surface diffusion.

The previous STM studies of step and island dynamics on Cu single crystals showed that the presence of the Cl adlayer has a substantial influence also on the diffusion of copper substrate adatoms which manifests in the enhancement of their mobilities [120–123]. For industrial purposes, the chloride species in combination with other additives are widely used in the damascene copper plating due to their properties to accelerate the deposition rate (accelerator agent) and to lead to the formation of uniformly thick copper deposits with a low surface roughness (leveling agent) [124–127], however the underlying mechanism of this process is not entirely understood yet. The impact of Cl adlayer on the surface diffusion of copper adatoms plays apparently the significant role during the crystal growth. In our experiments we could observe such influence for the example of sulphur and lead adsorbates. The direct study of copper surface diffusion is rather complicated due to the considerably higher mobilities of Cu_{ad} [128, 129]. Nevertheless, our recent study of dynamic trapping of copper adatoms by complexes of organosulfur additives gave first insights into the dynamics of those species too [130].

From a fundamental point of view, it is an intriguing scientific problem to reveal the effect of adlayers on atomic processes at electrochemical interfaces. Further experimental studies of surface tracer diffusion and adsorbate-adsorbate interactions within different halide adlayer (for ex., bromide, iodide) and comparison with identical studies on a bare metal substrate would shed additional light on the role of coadsorbed species and their structures in the dynamic processes at electrochemical interfaces.

A. List of the developed software

The performance of the quantitative measurements for adsorbate tracer diffusion and adsorbate-adsorbate interactions from sequences of raw STM images was divided into separate subtasks, for which the dedicated computer programs were developed and implemented on CodeGear™ Delphi® 2007 environment. The complete list of software used in the analysis together with their short descriptions is presented here.

1. **Image_Recognition_Software.exe.** Performs the recognition of sequences of raw STM images and produces in the output the corresponding sequences of digital occupation maps, which include the information about the occupation of the surface lattice sites by adsorbates. Detailed description is given in Chapter 2.
2. **Adsorbate_Distributions.exe.** Uses the sequences of digital occupation maps to generate three types of adsorbate distribution functions:
 - jump distribution function of isolated adsorbates;
 - two-dimensional jump distribution functions of isolated dimers;
 - spatial pair correlation function of adsorbates.

These distributions were used as input data in the following programs.

3. **Tracer_Diffusion.exe.** Calculates the hopping rates of the free adsorbates from their jump distribution functions.
4. **Dynamic_Method.exe.** Calculates the pairwise interatomic potential from the two-dimensional jump distribution functions of isolated dimers. Detailed description of the method is given in Chapter 3.1.
5. **Equilibrium_Method.exe.** Calculates the effective interatomic potential from the spatial pair correlation function of adsorbates. Detailed description of the method is given in Chapter 3.2.

B. List of original data used in the quantitative analysis

Filename	E , V _{SCE}	U_t , V	I_t , nA	Frames/s	N° Frames
031103z0.004	-0.320	0.01	9	10	119
031103z0.005	-0.320	0.01	7	10	336
191104z0.000	-0.380	0.11	15	10	1569
191104z0.001	-0.400	0.11	15	10	2045
191104z0.002	-0.420	0.11	15	10	1496
110604z0.004	-0.470	0.01	9	10	733
110604z0.005	-0.470	0.01	9	10	1135
110604z0.006	-0.470	0.01	9	10	814
110604z0.007	-0.490	0.01	9	10	954
110604z0.008	-0.490	0.01	9	10	1251
061104z0.004	-0.520	0.01	20	10	299
060105z0.030	-0.520	0.25	25	20	510
070105z0.014	-0.520	0.35	5	20	493

Table B.1.: Data files used for the quantitative analysis of S_{ad} - S_{ad} interactions.

Filename	E , V _{SCE}	U_t , V	I_t , nA	Frames/s	N° Frames
100219z0.001	-0.220	0.14	30	10	337
100219z0.004	-0.175	0.26	25	10	136
100304z0.002	-0.265	0.16	12	10	56
100316z0.007	-0.285	0.25	6	10	288
100316z0.009	-0.245	0.24	23	10	60
100316z0.010 ¹	-0.200	0.22	23	10	1400

Table B.2.: Data files used for the quantitative analysis of Pb_{ad} tracer diffusion and interactions¹.

¹The statistical analysis of Pb_{ad} - Pb_{ad} interactions was performed exclusively for the data set recorded at -0.20 V_{SCE}.

C. Bibliography

- [1] T. Tansel and O. M. Magnussen, Video STM studies of adsorbate diffusion at electrochemical interfaces, *Phys. Rev. Lett.* **96**, 026101 (2006).
- [2] C. H. Hamann, A. Hamnett, W. Viestich, Electrochemistry, *WILEY-VCH Verlag GmbH, Weinheim*, (1998).
- [3] W. Schmickler, Fundamentals of Electrochemistry, *Friedr. Vieweg & Sohn Verlagsgesellschaft GmbH, Braunschweig/Wiesbaden*, (1996).
- [4] M. Giesen, G. Beltramo, S. Dieluweit, J. Müller, H. Ibach, W. Schmickler, The thermodynamics of electrochemical annealing, *Surf. Sci.* **595**, 127 (2005).
- [5] J. Müller and H. Ibach, Migration of point defects at charged Cu, Ag, and Au (100) surfaces, *Phys. Rev. B* **74**, 085408 (2006).
- [6] H. Margenau, Van der Waal Forces, *Rev. Mod. Phys.* **11**, 1 (1939).
- [7] T. T. Tsong and G. Kellogg, Direct observation of the directional walk of single adatoms and the adatom polarizability, *Phys. Rev. B* **12**, 1343 (1975).
- [8] T. T. Tsong, Experimental studies of the behavior of single adsorbed atoms on solid surfaces, *Rep. Prog. Phys.* **51**, 759 (1988).
- [9] L. I. Schiff, Quantum Mechanics, 3rd edition, *McGraw-Hill Inc., New York*, (1968).
- [10] J. E. Jones, On the determination of molecular fields. II. From the equation of state of a gas, *Proc. R. Soc. Lond. A* **106**, 463 (1924).
- [11] M. W. Cole and D. R. Frankl, Probing the helium-graphite interaction, *Rev. Mod. Phys.* **53**, 199 (1981).
- [12] W. Kohn and K.-H. Lau, Adatom dipole moments on metals and their interactions, *Solid State Commun.* **18**, 553 (1976).

-
- [13] T. B. Grimley, The indirect interaction between atoms or molecules adsorbed on metals, *Proc. Phys. Soc.* **90**, 751 (1967).
- [14] T. L. Einstein and J. R. Schrieffer, Indirect interaction between adatoms on a tight-binding solid. *Phys. Rev. B* **7**, 3629 (1973).
- [15] K.-H. Lau and W. Kohn, Indirect long-range oscillatory interaction between adsorbed atoms, *Surf. Sci.* **75**, 69 (1978).
- [16] J. Repp, F. Moresco, G. Meyer, K.-H. Rieder, P. Hyldgaard and M. Persson, Substrate mediated long-range oscillatory interaction between adatoms: Cu/Cu(111), *Phys. Rev. Lett.* **85**, 2981 (2000).
- [17] P. Hyldgaard and M. Persson, Long-range adsorbate-adsorbate interactions mediated by a surface-state band, *J. Phys.: Condens. Matter* **12**, L13 (2000).
- [18] N. Knorr, H. Brune, M. Epple, A. Hirstein, M. A. Schneider and K. Kern, Long-range adsorbate interactions mediated by a two-dimensional electron gas, *Phys. Rev. B* **65**, 115420 (2002).
- [19] K.-H. Lau and W. Kohn, Elastic interaction of two atoms adsorbed on a solid surface, *Surf. Sci.* **65**, 607 (1977).
- [20] M. Ø. Pedersen, L. Österlund, J. J. Mortensen, M. Mavrikakis, L. B. Hansen, I. Stensgaard, E. Lægsgaard, J. K. Nørskov, and F. Besenbacher, Diffusion of N Adatoms on the Fe(100) Surface, *Phys. Rev. Lett.* **84**, 4898 (2000).
- [21] T.-M. Lu, G.-C. Wang and M. G. Lagally, Island-dissolution phase transition in a chemisorbed layer, *Phys. Rev. Lett* **39**, 411 (1977).
- [22] M. G. Lagally, G.-C. Wang and T.-M. Lu, Chemisorption: island formation and adatom interactions, *CRC Crit. Rev. Solid State Mater. Sci.* **7**, 233 (1978).
- [23] W. Y. Ching, D. L. Huber, M. G. Lagally and G.-C. Wang, Order-disorder transformations in chemisorped layers: oxygen on W(110), *Surf. Sci.* **77**, 550 (1978).
- [24] E. D. Williams, S. L. Cunningham and W. H. Weinberg, A determination of adatom-adatom interaction energies: application to oxygen chemisorbed on the tungsten (110) surface, *J. Chem. Phys.* **68**, 4688 (1978).

-
- [25] G. Doyen, G. Ertl and M. Plancher, Order-disorder phenomena in adsorbed layers described by a lattice gas model, *J. Chem. Phys.* **62**, 2957 (1975).
- [26] L. D. Roelofs, R. L. Park and T. L. Einstein, Adlayer-induced LEED beams near order-disorder transitions, *J. Vac. Sci. Technol.* **16**, 478 (1979).
- [27] L. D. Roelofs, A. R. Kortan, T. L. Einstein and R. L. Park, Two-dimensional chemisorbed phases, *J. Vac. Sci. Technol.* **18**, 492 (1981).
- [28] D. A. King, Kinetics of adsorption, desorption, and migration at single-crystal metal surfaces, *CRC Crit. Rev. Solid State Mater. Sci.* **7**, 167 (1978).
- [29] D. A. King and M. G. Wells, Reaction mechanism in chemisorption kinetics: nitrogen on the (100) plane of tungsten, *Proc. R. Soc. Lond. A* **339**, 245 (1978).
- [30] S. P. Singh-Borapai, M. Bowker and D. A. King, Crystallographic anisotropy in chemisorption: nitrogen on tungsten single crystal planes, *Surf. Sci.* **53**, 55 (1975).
- [31] T. T. Tsong, Field-ion microscope observations of indirect interaction between adatoms on metal surfaces, *Phys. Rev. Lett.* **31**, 1207 (1973).
- [32] T. T. Tsong and R. Casanova, Direct measurement of pair energies in adatom-adatom interactions on a metal surface, *Phys. Rev. B* **24**, 3063 (1981).
- [33] W. R. Graham and G. Ehrlich, Direct measurement of the pair distribution function for adatoms on a surface, *Phys. Rev. Lett.* **32**, 1309 (1974).
- [34] H.-W. Fink, K. Faulian, and E. Bauer, Evidence of nonmonotonic long-range interactions between adsorbed atoms, *Phys. Rev. Lett.* **44**, 1008 (1980).
- [35] H.-W. Fink and G. Ehrlich, Pair and trio interactions between adatoms: Re on W(110), *J. Chem. Phys.* **81**, 4657 (1984).
- [36] F. Watanabe and G. Ehrlich, Direct mapping of adatom-adatom interactions *Phys. Rev. Lett.* **62**, 1146 (1989).
- [37] F. Watanabe and G. Ehrlich, Direct observations of pair interactions on a metal: Heteropairs on W(110), *J. Phys. Chem.* **95**, 6075 (1991).
- [38] G. Ehrlich and F. Watanabe, Atomic interactions on crystals: a review of quantitative experiments, *Langmuir* **7**, 2555 (1991).

- [39] F. Watanabe and G. Ehrlich, Direct observations of interactions between identical adatoms: Ir–Ir and Re–Re on W(110), *J. Phys. Chem.* **95**, 6075 (1991).
- [40] S. J. Koh and G. Ehrlich, Pair- and many-atom interactions in the cohesion of surface clusters: Pd_x and Ir_x on W(110), *Phys. Rev. B* **60**, 5981 (1999).
- [41] J. Trost, T. Zambelli, J. Wintterlin, and G. Ertl, Adsorbate-adsorbate interactions from statistical analysis of STM images: N/Ru(0001), *Phys. Rev. B* **54**, 17850 (1996).
- [42] S. Renisch, R. Schuster, J. Wintterlin, and G. Ertl, Dynamics of adatom motion under the influence of mutual interactions: O/Ru(0001), *Phys. Rev. Lett.* **82**, 3839 (1999).
- [43] S. Renisch, Zur Diffusion adsorbierter Teilchen auf Einkristalloberflächen: Dynamische Untersuchungen mit dem Rastertunnelmikroskop, *PhD Thesis, Freie Universität Berlin* (1999).
- [44] Ph. Ebert, X. Chen, M. Heinrich, M. Simon, K. Urban, and M. G. Lagally, Direct determination of the interaction between vacancies on InP(110) surfaces, *Phys. Rev. Lett.* **76**, 2089 (1996).
- [45] L. Österlund, M.Ø. Pedersen, J. Stensgaard, E. Lægsgaard, and F. Besenbacher, Quantitative determination of adsorbate-adsorbate interactions, *Phys. Rev. Lett.* **83**, 4812 (1999).
- [46] H. E. Hoster, E. Filonenko, B. Richter, and R. J. Behm, Formation and short-range order of two-dimensional Cu_xPd_{1-x}/Ru(0001) monolayer surface alloys on Ru(0001), *Phys. Rev. B* **73**, 165413 (2006).
- [47] A. Bergbeiter, H. E. Hoster, S. Sakong, A. Groß, and R. J. Behm, Energetics driving the short-range order in Cu_xPd_{1-x}/Ru(0001) monolayer surface alloys *Phys. Chem. Chem. Phys.* **9**, 5127 (2007).
- [48] G. Binnig, H. Rohrer, Scanning tunneling microscopy, *Helv. Phys. Acta* **55**, 726 (1982).
- [49] G. Binnig, H. Rohrer, C. Gerber, E. Weibel, Surface studies by scanning tunneling microscopy, *Phys. Rev. Lett.* **49**, 57 (1982).
- [50] R. Wiesendanger, Scanning probe microscopy and spectroscopy: methods and applications, *Cambridge University Press*, (1994).

-
- [51] G. Antczak, G. Ehrlich, Surface diffusion: metals, metal atoms, and clusters, *Cambridge University Press*, (2010).
- [52] P. Samori, Scanning probe microscopies beyond imaging: manipulation of molecules and nanostructures, *WILEY-VCH Verlag GmbH & Co. KGaA, Weinheim*, (2006).
- [53] J. Frenkel, On the electrical resistance of contacts between solid conductors, *Phys. Rev.* **36**, 1604 (1930).
- [54] J. C. Fisher, I. Giaever, Tunneling through thin insulating layers, *J. Appl. Phys.* **32**, 172 (1961).
- [55] J. G. Simmons, Generalized formula for the electric tunnel effect between similar electrodes separated by a thin insulating film, *J. Appl. Phys.* **34**, 1793 (1963).
- [56] L. Zitzler, B. Gleich, O. M. Magnussen, R. J. Behm, Electrochemical Video-STM, *Proc. Electrochem. Soc.* **99-28**, 29 (2000).
- [57] O. M. Magnussen, L. Zitzler, B. Gleich, M. R. Vogt, R. J. Behm, In-situ atomic-scale studies of the mechanisms and dynamics of metal dissolution by high-speed STM, *Electrochim. Acta.* **46**, 3725 (2001).
- [58] L. Zitzler, Video-STM-Untersuchungen von Reaktionen an der Metall-Flüssigkeits-Grenzfläche, *Diplomarbeit, Universität Ulm*, (2000).
- [59] B. Gleich, Entwicklung eines schnellen Rastertunnelmikroskops zur Untersuchung von Diffusionsprozessen auf Platin Ruthenium Legierungen, *Dissertation, Universität Ulm*, (2000).
- [60] M. R. Vogt, F. Möller, C. M. Schilz, O. M. Magnussen, R. J. Behm, Adsorbate-induced step faceting of Cu(100) electrodes in HCl, *Surf. Sci.*, **367**, L33 (1996).
- [61] T. Tansel, Video-STM-Untersuchungen der Diffusion von Adsorbaten in elektrochemischer Umgebung, *PhD Thesis, CAU Kiel* (2006).
- [62] M. J. Heben, M. M. Dovek, N. S. Lewis, R. M. Penner, C. F. Quate, Preparation of STM tips for *in situ* characterization of electrode surfaces, *J. Microsc.*, **152**, 651 (1988).

-
- [63] M. J. Heben, R. M. Penner, N. S. Lewis, M. M. Dovek, C. F. Quate, Atomic resolution imaging of electrode surfaces in solutions containing reversible redox species, *Appl. Phys. Lett.*, **54**, 1421 (1989).
- [64] L. A. Nagahara, T. Thundat, S. M. Lindsay, Preparation and characterization of STM tips for electrochemical studies, *Rev. Sci. Instrum.*, **60**, 3128 (1989).
- [65] M. J. J. Jak, C. Konstapel, A. van Kreuningen, J. Verhoeven, R. van Gastel, and J. W. M. Frenken, Automated detection of particles, clusters and islands in scanning probe microscopy images, *Surf. Sci.* **494**, 43 (2001).
- [66] R. N. Bracewell, The Fourier Transform and its Applications, Second edition, *Mc-Graw Hill, Inc., New York*, (1965).
- [67] S. Glasstone, K. J. Laidler, H. Eyring, The Theory of Rate Processes: the kinetics of chemical reactions, viscosity, diffusion and electrochemical phenomena, *Mc-Graw Hill, Inc., New York*, (1941).
- [68] K. D. Dobbs and D. J. Doren, Dynamics of molecular surface diffusion: Origins and consequences of long jumps, *J. Chem. Phys.* **97**, 3722 (1992).
- [69] A. Iserles, A first course in the numerical analysis of differential equations, *Cambridge University Press*, (2004).
- [70] T. Tansel, A. Taranovsky and O. M. Magnussen, *In situ* Video-STM studies of adsorbate dynamics at electrochemical interfaces, *Chem. Phys. Chem.* **11**, 1438 (2010).
- [71] P. R. Bevington, *Data Reduction and Error Analysis for the Physical Sciences*, *New York: McGraw-Hill* (1969).
- [72] T. T. Tsong, Quantitative investigations of atomic processes on metal surfaces at atomic resolution, *Prog. Surf. Sci.* **10**, 165 (1980).
- [73] N. Metropolis and S. Ulam, The Monte Carlo Method, *JASA* **44**, 335 (1949).
- [74] N. Metropolis, A. W. Rosenbluth, M. N. Rosenbluth and A. H. Teller, Equation of state calculations by fast computing machines, *J. Chem. Phys.* **21**, 1087 (1953).
- [75] J. A. Nedler and R. Mead, A simplex method for function minimization, *Computer Journal (UK)* **7**, 308 (1965).

-
- [76] W. H. Press, *Numerical recipes in FORTRAN: the art of scientific computing*, Cambridge University Press (1992).
- [77] D. P. Woodruff, Adsorbate-induced reconstruction of surfaces: An atomistic alternative to microscopic faceting?, *J. Phys.: Condens. Matter* **6**, 6067 (1994).
- [78] A. Spaenig, P. Broekmann, and K. Wandelt, Structure of electrochemically deposited sulfide layers on Cu(100), *Z. Phys. Chem.* **217**, 459 (2003).
- [79] C. Schlaup, A. Spaenig, P. Broekmann, and K. Wandelt, Sulfide anion interaction with Cu(100) and Cu modified Au(100): An electrochemical STM study, *Phys. Status Solidi A* **207**, 254 (2010).
- [80] A. Taranovskyy, T. Tansel and O. M. Magnussen, Quantitative Measurements of Adsorbate-Adsorbate Interactions at Solid-Liquid Interfaces, *Phys. Rev. Lett.* **104**, 106101 (2010).
- [81] T. Tansel, A. Taranovskyy, and O. M. Magnussen, *In situ* Video-STM studies of adsorbate dynamics at electrochemical interfaces, *ChemPhysChem* **11**, 1438 (2010).
- [82] G. A. Somorjai and F. Szalkowski, Simple rules to predict the structure of adsorbed gases on crystal surfaces, *J. Chem. Phys.* **54**, 389 (1971).
- [83] T. L. Einstein and J. R. Schrieffer, Indirect interaction between adatoms on a tight-binding solid, *Phys. Rev. B* **7**, 3629 (1973).
- [84] T. T. Tsong and R. Casanova, Correlation between adatom-adatom pair interaction and adlayer superstructure formation: Si on W(110), *Phys. Rev. Lett.* **47**, 113 (1981).
- [85] H. W. Fink and G. Ehrlich, Direct observation of overlayer structures on W(110), *Surf. Sci.* **110**, L611 (1981).
- [86] C. Uebing and R. Gomer, A Monte Carlo study of surface diffusion coefficients in the presence of adsorbate-adsorbate interactions. III. Repulsive nearest-neighbor and attractive next-nearest-neighbor interactions, *J. Chem. Phys.* **95**, 7641 (1991).
- [87] E. G. Seebauer and C. E. Allen, Estimating surface diffusion coefficients, *Prog. Surf. Sci* **49**, 265 (1995).
- [88] C. Nagl, E. Platzgummer, O. Haller, M. Schmid and P. Varga, Surface alloying and superstructures of Pb on Cu(100), *Surf. Sci* **331**, 831 (1995).

- [89] C. Nagl, O. Haller, E. Platzgummer, M. Schmid and P. Varga, Submonolayer growth of Pb on Cu(111): surface alloying and de-alloying, *Surf. Sci* **321**, 237 (1994).
- [90] S. Robert, S. Gauthier, F. Bocquet, S. Rousset, J. L. Duvault, J. Klein, An STM study of the adsorption of Pb on Cu(100): formation of an ordered surface alloy, *Surf. Sci* **350**, 136 (1996).
- [91] M. L. Anderson, N. C. Bartelt, B. S. Swartzentruber, The importance of Pb-vacancy attractions on diffusion in the Pb/Cu(001) surface alloy, *Surf. Sci* **538**, 53 (2003).
- [92] C. Cohen, Y. Girard, P. Leroux-Hugon, A. L'Hoir, J. Moulin, D. Schmaus, Surface diffusion of Pb on (100) Cu: coverage dependence and influence of ordered-phase formation, *Eur. Phys. Lett.* **24**, 767 (1993).
- [93] G. Ehrlich, Atomic displacements in one and two dimensional diffusion, *J. Chem. Phys.* **44**, 1050 (1966).
- [94] S. Guézo, A. Taranovskyy, H. Matsushima, and O. M. Magnussen, Surface dynamics of lead adsorbates at the Cu(100)-electrolyte interface, *J. Phys. Chem. C* **115**, 19336 (2011).
- [95] W. J. Lorenz, E. B. Budevski, G. T. Staikov, Electrochemical phase formation and growth, *Wiley-VCH: Weinheim, Germany*, 1996.
- [96] W. J. Lorenz, H. D. Hermann, N. Wüthrich, and F. Hilbert, The formation of monolayer metal films on electrodes, *J. Electrochem. Soc.* **121**, 1167 (1974).
- [97] J. W. Schultze, D. Dickertmann, Potentiodynamic desorption spectra of metallic monolayers of Cu, Bi, Pb, Tl, and Sb adsorbed at (111), (100), and (110) planes of gold electrodes, *Surf. Sci.* **54**, 489 (1976).
- [98] E. Herrero, L. J. Buller, and H. D. Abruna, Underpotential deposition at single crystal surfaces of Au, Pt, Ag and other materials, *Chem. Rev.* **101**, 1897 (2001).
- [99] D. M. Kolb, In *Advances in Electrochemistry and Electrochemical Engineering*, H. Gerisher, C. W. Tobias, Eds., *Wiley-Interscience: New York*, 1978, Vol. **11**, p. 125.
- [100] E. Schmidt, N. Wüthrich, Untersuchung der adsorption von Pb an silberelektroden in chloridlösung mit einem zweielektroden-dünnschichtverfahren, *J. Electroanal. Chem.* **28**, 349 (1970).

- [101] E. Schmidt, N. Wüthrich, Elektroanalytische Untersuchung der Pb-Adsorption an Goldelektroden nach dem Zweielektroden-Dünnschichtverfahren, *J. Electroanal. Chem.* **34**, 377 (1972).
- [102] E. Schmidt, N. Wüthrich, Zweielektroden-dünnschichtversuche zur Pb-adsorption an platin, *J. Electroanal. Chem.* **40**, 399 (1972).
- [103] A. Bewick, B. Thomas, Effects of substrate orientation on underpotential monolayers of Pb and Tl deposited on single crystals, *J. Electroanal. Chem.* **70**, 239, (1976).
- [104] A. Bewick, J. Jovicevic and B. Thomas, Phase formation in the underpotential deposition of metals, *Faraday Symp. Chem. Soc.* **12**, 24, (1977).
- [105] H. Bort, K. Jüttner, W. J. Lorenz, E. Schmidt, Lead adsorption on silver single crystal surfaces, *J. Electroanal. Chem.* **90**, 413, (1978).
- [106] D. Dickertmann, F. D. Koppitz, J. W. Schultze, Eine methode zum ausschluss von randeffekten bei elektrochemischen messungen an einkristallen: Test anhand der adsorptionssysteme Ag/Pb²⁺ und Au/Cu²⁺, *Electrochim. Acta* **21**, 967, (1976).
- [107] K. Jüttner and W. J. Lorenz, Underpotential metal deposition on single crystal surfaces, *Z. Phys. Chem.* **122**, 163, (1980).
- [108] S. Gauthier, W. Moritz, W. Höslér, Surface alloy in the $c(4 \times 4)$ phase of Pb on Cu(100), *Surf. Sci* **345**, 53 (1996).
- [109] W. Li, G. Vidali, O. Biham, Scaling of island growth in Pb overlayers on Cu(001), *Phys. Rev. B* **48**, 8336 (1993).
- [110] S. Robert, C. Cohen, A. L'Hoir, J. Moulin, D. Schmaus, M. G. Barthes-Labrousse, A channeling study of lead submonolayers deposited onto Cu(100), *Surf. Sci* **365**, 285 (1996).
- [111] A. Sánchez, S. Ferrer, Structure and melting of lead overlayers on Cu(100) studied with thermal-energy atom scattering, *Phys. Rev. B* **39**, 5778 (1989).
- [112] T. P. Moffat, Oxidative chloride adsorption and lead upd on Cu(100): investigations into surfactant-assisted epitaxial growth, *J. Phys. Chem. B* **102**, 10200 (1998).
- [113] N. Vasiljevic, Surface ordering during underpotential deposition of lead on copper, *Ph.D. Thesis, Arizona State University*, (2004).

- [114] J. Henrion, G. E. Rhead, Leed studies of the first stages of deposition and melting of lead on low index faces of copper, *Surf. Sci* **29**, 20 (1972).
- [115] W. Höslér, W. Moritz, LEED studies of lead on copper (100), *Surf. Sci* **117**, 196 (1982).
- [116] W. Höslér, W. Moritz, LEED analysis of a dense lead monolayer on copper (100), *Surf. Sci* **175**, 63 (1986).
- [117] H.-C. Wu, S.-L. Yau, In situ Scanning Tunneling Microscopy of underpotential deposition of lead on Cu(100) in sulfuric acid solutions, *J. Phys. Chem. B* **105**, 6965 (2001).
- [118] G. L. Kellogg, R. Plass, The relationship between the growth shape of three-dimensional Pb islands on Cu(100) and the domain orientation of the underlying $c(5\sqrt{2} \times \sqrt{2})R45^\circ$ structure, *Surf. Sci.* **465**, L777 (2000).
- [119] R. V. Kukta, N. Vasiljevic, N. Dimitrov, K. Sieradzki, Self-assembly of paired nanoribbons, *Phys. Rev. Lett.* **95**, 186103 (2005).
- [120] D. W. Suggs, A. J. Bard, Scanning Tunneling Microscopic study with atomic resolution of the dissolution of Cu(111) in aqueous chloride solutions, *J. Am. Chem. Soc.* **116**, 10725 (1994).
- [121] M. Wilms, P. Broekmann, M. Krufft, C. Stuhlmann, K. Wandelt, STM investigation of step orientation and surface dynamics of Cu(111) in hydrochloric acid electrolyte, *Appl. Phys. A* **66**, S473 (1998).
- [122] M. Giesen, S. Baier, Atomic transport processes on electrodes in liquid environment, *J. Phys.: Condens. Matter* **13**, 5009 (2001).
- [123] M. Giesen, Step and island dynamics at solid/vacuum and solid/liquid interfaces, *Prog. Surf. Sci.* **68**, 1 (2001).
- [124] C. Andricacos, C. Uzoh, J. O. Dukovic, J. Horkans, H. Deligianni, Damascene copper electroplating for chip interconnections, *IBM J. RES. DEV.* **42**, 567 (1998).
- [125] T. P. Moffat, D. Wheeler, M. D. Edelstein, D. Josell, Superconformal film growth: mechanism and quantification, *IBM J. RES. DEV.* **49**, 19 (2005).

-
- [126] T. P. Moffat, J. E. Bonevich, W. H. Huber, A. Stanishevsky, D. R. Kelly, G. R. Stafford, D. Josell, Superconformal electrodeposition of copper in 500-90 nm features, *J. Electrochem. Soc.* **147**, 4524 (2000).
- [127] P. M. Vereecken, R. A. Binstead, H. Deligianni, P. C. Andricacos, The chemistry of additives in damascene copper plating, *IBM J. RES. DEV.* **49**, 3 (2005).
- [128] H. J. Ernst, F. Fabre, J. Lapujoulade, Nucleation and diffusion of Cu adatoms on Cu(100): A helium-atom-beam scattering study, *Phys. Rev. B* **46**, 1929 (1992).
- [129] J. J. de Miguel, A. Sánchez, A. Cebollada, J. M. Gallego, J. Ferrón, S. Ferrer, The surface morphology of a growing crystal studied by thermal energy atom scattering (TEAS), *Surf. Sci.* **189-190**, 1062 (1987)
- [130] Y.-C. Yang, A. Taranovskyy, O. M. Magnussen, Thiolate-induced metal adatom trapping at solid-liquid interfaces, *Angew. Chem. Int. Ed.* **51**, 1966 (2012).

Publication list

- **Studies of Lead Surface Alloying and Dealloying on Cu(100) in Cl-Containing Solutions by *In Situ* High-Speed STM**
A. Taranovskyy, S. Guézo, H. Matsushima, Y. Gründer, O. M. Magnussen
submitted to Phys. Chem. Chem. Phys.
- **Thiolate-Induced Metal Adatom Trapping at Solid-Liquid Interfaces**
Y.-C. Yang, A. Taranovskyy, O. M. Magnussen
Angew. Chem. Int. Ed. 51, 1966-1969 (2012)
- **Surface Dynamics of Lead Adsorbates at the Cu(100)-Electrolyte Interface**
S. Guézo, A. Taranovskyy, H. Matsushima, O. M. Magnussen
J. Phys. Chem. C 115, 19336-19342 (2011)
- ***In situ* video STM studies of the hydrogen-induced reconstruction of Cu(100): potential and pH dependence**
H. Matsushima, C. Haak, A. Taranovskyy, Y. Gründer, O. M. Magnussen
Phys. Chem. Chem. Phys. 12, 13992-13998 (2010)
- **Quantitative Measurements of Adsorbate-Adsorbate Interactions at Solid-Liquid Interfaces**
A. Taranovskyy, T. Tansel, O. M. Magnussen
Phys. Rev. Lett. 104, 106101 (2010)
- ***In Situ* Video-STM Studies of Adsorbate Dynamics at Electrochemical Interfaces**
T. Tansel, A. Taranovskyy, O. M. Magnussen
ChemPhysChem 11, 1438 - 1445 (2010)
- **Reconstruction of Cu(100) Electrode Surfaces during Hydrogen Evolution**
H. Matsushima, A. Taranovskyy, C. Haak, Y. Gründer, O. M. Magnussen
J. Am. Chem. Soc. 131, 10362-10363 (2009)

-
- **On the Determination of the Equilibrium Surface Segregation Isotherms from Kinetic Measurements**
Z. Erdelyi, A. Taranovskyy, D.L. Beke
Rev. Adv. Mater. Sci. 21, 6-17 (2009)
 - **Dissolution and Off-Stoichiometric Formation of Compound Layers in Solid State Reactions**
Z. Erdélyi, D. L. Beke, A. Taranovskyy
Appl. Phys. Lett. 92, 133110 (2008)
 - **On the Determination of the Equilibrium Surface Segregation Isotherms from Kinetic Measurements**
Z. Erdelyi, A. Taranovskyy, D. L. Beke
Surf. Sci. 602, 805-810 (2008)
 - **On the Local Equilibrium during Dissolution of a Thin Film**
Z. Erdélyi, A. Taranovskyy, D. L. Beke
Diffusion and Defect Data 264, 171-175 (2007)

Curriculum Vitae

Andriy Taranovskyy

Address Steenbker Weg 6, 6101
 D-24106 Kiel

Date of Birth July 31st 1982
 in Antypiwka,
 son of Oleksiy Taranovskyy
 and Lidiya Taranovska

Nationality Ukraine



Education and Research Experience

- Jan. 2007 - Mar. 2012 PhD project in the group of Prof. Dr. O. M. Magnussen, Institute of Experimental and Applied Physics, University Kiel: 'Adsorbate-adsorbate interactions at electro-chemical interfaces'.
- Sep. 2005 - Sep. 2006 Research project 'Interface atomic motions' under the supervision of Prof. Dr. D. L. Beke, Debrecen University, Department of Solid State Physics, Debrecen, Hungary.
- Oct. 2004 - Aug. 2005 Research project 'Computer modeling of the diffusional welding' under the supervision of Prof. Dr. A. M. Gusak, B. Khmelnytsky State University at Cherkasy, Cherkasy, Ukraine.
- Sep. 1999 - Jun. 2004 Undergraduate Course in physics at B. Khmelnytsky State University at Cherkasy, Cherkasy, Ukraine:
09/2003 - 06/2004: Master thesis in the group of Prof. Dr. A. M. Gusak, 'Modeling of Diffusional Processes at Interface' (The Sintering of Nanoparticles)
09/1999 - 07/2003: Bachelor thesis in the group of Prof. Dr. A. M. Gusak, 'Modeling of Diffusional Processes at Interface' (The Molecular Dynamic approach)

Sep. 1988 - Jun. 1999 Comprehensive school in Antypiwka, Ukraine

Tutoring Experience

Sep. 2004 - Jul. 2005 State Business-College at Cherkasy, Cherkasy, Ukraine
Courses: Numerical analysis, Computer graphics.

Kiel, den 25. Mai 2012

Acknowledgements

At this point I would like to express my gratitude to all those people who made their contribution for this work. I am very grateful to . . .

. . . my thesis adviser Prof. Dr. Olaf Magnussen who gave me the possibility to work on a very interesting and inspiring scientific project. I appreciate his professional guidance, helpful advices and well-established feedback.

. . . Dr. Tunay Tansel, Dr. Hisayoshi Matsushima, Dr. Sophie Guezo, Dr. Yvonne Gründer for their considerable contributions in the common cause.

. . . Dr. Yaw-Chia Yang for the fruitful cooperation in the adjoining research project on methyl thiolate dynamics.

. . . Christian Haak for his masterly introduction into the operation of high-speed STM technique.

. . . Arnd Seeger for the prompt and efficient support in computing tools.

. . . Monica Seeger, Rosemarie Müller-Puffe and Linda Sommer for their administrative and social care.

. . . my office mates, current and former group colleagues and friends in Kiel for a nice atmosphere during working and leisure hours spend together. Special thanks to Dr. Klaus Krug, Dr. Frederik Golks, Dr. Bridget Murphy, Dr. Jochim Stettner, Belinda Baisch, Dr. Ulrich Jung, Anika Elsen, Stjepan Hrkac, Sven Festersen, Laura Lazzari and Lu Zhang.

. . . my family, especially my parents and my grandma, for their support and patience.

. . . Deutscher Akademischer Austauschdienst and Deutsche Forschungsgemeinschaft for the vital financial support.

My special thanks goes to the city of Kiel with its unique environment, where I had a chance to spend a considerable part of my life.

Eidesstattliche Erklärung

Hiermit versichere ich, dass ich die vorgelegte Dissertation, abgesehen von der Beratung durch mein Betreuer Prof. Dr. O. Magnussen, selbständig verfasst und keine anderen als die angegebenen Quellen und Hilfsmittel verwendet habe. Die Arbeit ist unter Einhaltung der Regeln guter wissenschaftlicher Praxis entstanden. Teile der Arbeit sind bereits veröffentlicht oder als Manuskript zur Veröffentlichung eingereicht worden. Meine den Veröffentlichungen und Manuskripten zugrunde liegenden Beiträge sind im Folgenden genauer aufgeschlüsselt:

Phys. Rev. Lett. 104, 106101 (2010), Kapitel 4.2: Implementierung der Software zur Bilderkennung Analyse sowie für die quantitative Analyse von Tracerdiffusion und Adsorbat-Adsorbat-Wechselwirkungen. Die Umsetzung der Änderungen an dem bestehenden Modell für das Extrahieren von Adsorbat-Adsorbat Wechselwirkungen aus den experimentellen Daten. Video-Rastertunnelmikroskopie Daten wurden von Dr. T. Tansel früher aufgezeichnet. Durchführung der Auswertung mit das geschriebene Software. Verfassung des Manuskriptes. Maßgebliche Beteiligung an Interpretation der Auswertungen und Diskussion der Publikation.

ChemPhysChem. 11, 1438 (2010), Kapitel 4.3: Die quantitativen Verifikation des Einflusses der RTM Spitze auf die Diffusion der isolierten Adsorbate. Durchführung der quantitative Analyse von Adsorbat-Adsorbat-Wechselwirkungen. Video-Rastertunnelmikroskopie Daten wurden von Dr. T. Tansel aufgezeichnet. Verfassung des Manuskriptes durch Prof. Dr. O. M. Magnussen. Maßgebliche Beteiligung an Interpretation der Auswertungen und Diskussion der Publikation.

J. Phys. Chem. C 115, 19336 (2011), Kapitel 5.2: Beteiligung an Vorbereitung und Durchführung der in situ Rastertunnelmikroskopie Experimente zusammen mit Dr. H. Matsushima und Dr. S. Guezo. Durchführung der Auswertung zusammen mit Dr. S. Guezo. Verfassung des Manuskriptes durch mich und Dr. S. Guezo. Maßgebliche Beteiligung an Interpretation der Auswertungen und Diskussion der Publikation.

Manuskript eingereicht für Phys. Chem. Chem. Phys., Kapitel 5.4: Beteiligung an Vorbereitung und Durchführung der in situ Rastertunnelmikroskopie Experimente zusammen mit Dr. H. Matsushima und Dr. S. Guezo. Die Hauptteile der ex situ elektrochemischen Charakterisierung wurden von Dr. Y. Gründer und Dr. S. Guezo durchgeführt. Durchführung der Auswertung. Verfassung des Manuskriptes. Maßgebliche Beteiligung an

Interpretation der Auswertungen und Diskussion der Publikation.

Ich versichere, dass die vorliegende Dissertation weder ganz noch in Teilen Bestandteil einer anderen Studien- oder Prüfungsleistung war. Des Weiteren bestätige ich, keine früheren Promotionsversuche unternommen zu haben. Mir ist bewusst, dass Zuwiderhandlungen gegen diese Erklärung den Ausschluss von der Prüfung zur Folge haben können.

Kiel, den 25. Mai 2012